Studies on a discrete symmetry violation in epithermal region using neutron-induced compound states

高田, 秀佐

https://hdl.handle.net/2324/4784399

出版情報：九州大学, 2021, 博士（理学）, 課程博士
バージョン：
権利関係：

KYUSHU UNIVERSITY

DOCTORAL THESIS

Studies on a discrete symmetry violation in the epithermal region using neutron-induced compound states

---

Author:	*Supervisor:*
Shusuke TAKADA	Tamaki YOSHIOKA

A thesis submitted in fulfillment of the requirements
for the degree of Doctor of Science

in the

Department of Physics

March 3, 2022

Abstract

Charged conjugate and parity (CP) violation, which refers to the asymmetry between particles and antiparticles, is essential to explain the matter–antimatter imbalance in the present universe. Based on the CPT theorem, the search for time-reversal (T) violation is synonymous with the search for CP violation. T violation is an unsolved problem in physics, and search experiments are being conducted worldwide. Neutron-induced compound nuclei can potentially search for T violation with high sensitivity.

Scholars have theoretically proposed that a large T violation in compound nuclei appears in p-wave resonance, which is a resonance with an orbital angular momentum of 1 for the incident neutron. Its amplification factor is described by the unknown parameters ϕ and $\kappa(J)$. Although previous studies have reported only ϕ and $\kappa(J)$ for the energy region around 1 eV, several p-wave resonances of compound nuclei exist in the epithermal neutron region from 1 eV to 1 keV, and they are still unexplored in the high-energy region. This thesis reports two research results, aimed at extending the study of compound nuclei to the epithermal neutron region.

The first is the study of ϕ and $\kappa(J)$ for indium-115 (^{115}In). In general, the peak distance between resonances becomes denser at higher incident neutron energies. Therefore, studies using ^{115}In can properly demonstrate nuclear research on the epithermal neutron region, where multiple resonances are observed below 10 eV. In this study, the values of ϕ and $\kappa(J)$ for ^{115}In were determined for the first time, and ^{115}In was observed to be a strong candidate for a T violation search. Two sets of values obtained through an analysis based on the theoretical formalism are

$$\phi = 23.0^{+17.8+4.7\circ}_{-21.0-6.9} \text{ and } |\kappa(J)| = 1.10^{+0.29+0.07}_{-0.26-0.09}, \text{ or}$$
$$\phi = 252.0^{+21.0+6.9\circ}_{-17.8-4.5} \text{ and } \kappa(J) > 1.66.$$

The second is a development of spin polarization devices for epithermal neutrons. The polarization of neutron spins is essential in the search for T violation, and proton spin filters are particularly suitable for the neutron polarization of higher energies. In this study, a neutron spin-polarization device based on proton polarization using the spin of photo-excited triplet electrons was developed, and the polarization of epithermal neutrons was experimentally successful for the first time. The average values of the proton and neutron polarizations were 0.250 ± 0.050 and 0.076 ± 0.015, respectively.

Acknowledgements

First, I would like to express my gratitude to my supervisor, Professor Tamaki Yoshioka. I cannot count the number of things he taught me, including how to conduct research, conduct experiments and analysis, and write papers. Although I often felt my heart break under his severe comments, this doctoral thesis would never have been completed without his help. His way of thinking and living has been passed on to me and has definitely had a great impact on my life. My employment was introduced by him and is in a field close to my current research, so I look forward to working with him again.

I have lived for nine years in the Experimental Particle Physics laboratory of Kyushu University, and there are too many people to thank. Among them, I would like to make special mention and thank Professor Kiyotomo Kawagoe. Thanks to him, I learned the basics of particle physics and experiments. I am equally grateful to Professor Satoshi Sakaguchi of the Experimental Nuclear Physics Laboratory. He gave me much advice on polarization experiments. Additionally, Professor Yoshioka, Professor Kawagoe and Professor Sakaguchi reviewed my doctoral thesis.

I would like to thank all the collaborators in the NOPTREX experiment, where I have worked for many years. In particular, Professor Hirohiko Shimizu taught me basic knowledge about neutrons and my attitude toward physics research. I also spent much time with my colleagues, Dr. Takuya Okudaira, Dr. Jun Koga, and Dr. Tomoki Yamamoto, with whom I had many discussions about physics analysis and experiments at J-PARC. In particular, Dr. Okudaira and I participated in the NOPTREX experiment at the same time, and he spent the most time with me, not only in our research life. When I was depressed, he often comforted me and stabilized my mind. Dr. Koga joined the same laboratory when I was in my second year of the master's program, and we have worked together at the NOPTREX experiment since a year later. Until he joined the NOPTREX experiment, I was the only student in the Kyushu group, which was very discouraging. I am very grateful that he has joined the group. Apart from Dr. Okudaira, I have had the most discussions with him.

I am grateful to the staff of the MLF at J-PARC for providing the neutron beam and instruments for my experiments. In particular, I would like to thank Dr. Atsushi Kimura for his technical support with beamline 04 and technical advice for the analysis of the measurement data, which was very important for my research.

I have been working at RIKEN for three years in the JRA program. In particular, I would like to thank Dr. Tomohiro Uesaka, Dr. Kenichiro Tateishi, Dr. Yoshie Otake, Dr. Yasuo Wakabayashi, and Dr. Yoshimasa Ikeda for giving me much advice during my research at RIKEN. The development of polarization devices and polarization experiments using a compact neutron source would not have been possible without their support.

Finally, I would like to express my deepest gratitude to my parents, siblings, and friends who have supported me. In particular, I would like to repay my father Akinori and my mother Nobuko, who have warmly watched over me in every aspect of my life, little by little over time.

Contents

List of Figures

List of Tables

Chapter 1

Introduction

In this chapter, the historical background of previous studies on discrete symmetry violations and the purpose of this study are explained. The structure of this thesis is presented at the end of the chapter.

1.1 Discrete symmetry violation

In particle physics, three discrete symmetries are defined for charge conjugation (C), parity (P), and time reversal (T). A transformation for C means the exchange of a particle and an antiparticle. A transformation for P means the inversion of a spatial coordinate. A transformation for T means the inversion of a time coordinate. Until the 1950s, the physical phenomena in these three transformations were considered to be symmetrical.

1.1.1 P violation

In the mid-1950s, P violation was proven. In 1949, the following two different decays were observed in charged strange particles:

$$\begin{aligned} \theta &\rightarrow \pi + \pi, \\ \tau &\rightarrow \pi + \pi + \pi. \end{aligned}$$

The parent particles, θ and τ, have different parities because the intrinsic parity of the π meson is $P = -1$; therefore, they were considered to be different particles [1]. However, no differences were observed in the mass and lifetime of these particles, implying that they were the same particle. This problem is known as the $\theta - \tau$ puzzle. Today, θ and τ are known as K^+ mesons. In 1956, the problem of the $\theta - \tau$ puzzle was theoretically explained by C. N. Yang and T. D. Lee in that P symmetry can be violated in physical phenomena involving weak interactions [2]. This prediction was confirmed in 1957 by C. S. Wu *et al.* in an experiment on the β-decay events of ^{60}Co, which involve weak interactions [3]. In this experiment, an asymmetric angular distribution in the spin direction of ^{60}Co was observed, providing direct evidence for P violation.

1.1.2 CP violation

Following the evidence of P violation, the conservation of CP symmetry, which is the product of P and C transformations, was predicted by L. Landau [4]. However, CP violation in weak interactions was observed in neutral K meson decays by J. H. Christenson *et al.* in 1964 [5]. At that time, two types of K_1 and K_2 decays with different decay channels were known: K_1 decays to two pions, and K_2 decays to three pions, which means that these two K mesons have different CP eigenstates. Moreover, two different K mesons, K_{S} and K_{L}, with lifetimes $\tau_{\mathrm{S}} = 8.9\times10^{-11}$ s and $\tau_{\mathrm{L}} = 5.2\times10^{-8}$ s, respectively, were also observed. The subscripts, S and L represent the initial letters of "short" and "long," respectively. Before the experiment by J. H. Christenson *et al.*, K_{S} and K_{L} were believed to be K_1 and K_2, respectively. However, K_{L} was discovered to decay into two pions with a branching ratio of 2×10^{-3}. This implies that K_{S} and K_{L} are not K_1 and K_2 but a mixture of two CP eigenstates, providing evidence for CP violation.

The CP violation observed in the K_{L} meson experiment was theoretically explained by the Cabibbo–Kobayashi–Maskawa (CKM) matrix proposed by M. Kobayashi and T. Maskawa in 1973 [6]. The CKM matrix is a matrix for the coupling constants of interactions owing to weak interactions with changing flavors, and it represents the mixing of quarks of different generations. The CKM matrix, V_{CKM}, is given by

$$\begin{aligned}
V_{\mathrm{CKM}} &= \begin{pmatrix} V_{ud} & V_{us} & V_{ub} \\ V_{cd} & V_{cs} & V_{cb} \\ V_{td} & V_{ts} & V_{tb} \end{pmatrix} \\
&= \begin{pmatrix} 1 & 0 & 0 \\ 0 & c_{23} & s_{23} \\ 0 & -s_{23} & c_{23} \end{pmatrix} \begin{pmatrix} c_{13} & 0 & s_{13}e^{-i\delta} \\ 0 & 1 & 0 \\ s_{13}e^{i\delta} & 0 & c_{13} \end{pmatrix} \begin{pmatrix} c_{12} & s_{12} & 0 \\ -s_{12} & c_{12} & 0 \\ 0 & 0 & 1 \end{pmatrix} \\
&= \begin{pmatrix} c_{12}c_{13} & s_{12}c_{13} & s_{13}e^{-i\delta} \\ -s_{12}c_{23} - c_{12}c_{23}e^{i\delta} & -c_{12}c_{23} - s_{12}s_{23}s_{13}e^{i\delta} & s_{23}c_{13} \\ s_{12}c_{23} - c_{12}c_{23}s_{13}e^{i\delta} & -c_{12}c_{23} - s_{12}c_{23}s_{13}e^{i\delta} & c_{23}c_{13} \end{pmatrix} \\
&= \begin{pmatrix} 0.97401 \pm 0.00011 & 0.22650 \pm 0.00048 & 0.00361^{+0.00011}_{-0.00009} \\ 0.22636 \pm 0.00048 & 0.97320 \pm 0.00011 & 0.04053^{+0.00083}_{-0.00061} \\ 0.00854^{+0.00023}_{-0.00016} & 0.03978^{+0.00082}_{-0.00060} & 0.999172^{+0.000000}_{-0.000035} \end{pmatrix}
\end{aligned}$$

where $s_{ij} = \sin\theta_{ij}$, $c_{ij} = \cos\theta_{ij}$, and δ are the CP-violating phases in the flavor-changing process in the Standard Model of particle physics. The three angles θ_{12}, θ_{13}, and θ_{23} are mixing angles called Euler angles, and θ_{12}, in particular, is called the Cabibbo angle. The values of these parameters were measured to be $s_{12} = 0.22650 \pm 0.00048$, $s_{13} = 0.00361^{+0.00011}_{-0.00009}$, $s_{23} = 0.04053^{+0.00083}_{-0.00061}$, and $\delta = 1.196^{+0.045}_{-0.043}$, respectively [7]. The Kobayashi–Maskawa model also predicted an even larger CP violation in the neutral B meson, which was later discovered in the Belle [8] and BaBar [9] experiments.

1.1.3 Matter—antimatter imbalance

In the early universe, which was in a high-density and high-energy state, particles and antiparticles were in equilibrium through repeated processes of pair production and pair annihilation, and it is expected that the amount of particles and antiparticles were the same. However, the amount of matter and antimatter in the present universe is unbalanced. Therefore, CP violation, described in the previous section, is the key to explaining the current matter-dominant universe [10].

The asymmetry in the amount of matter and antimatter particles predicted based on the Standard Model is given by

$$\frac{n_B - n_{\bar{B}}}{n_\gamma} \sim 10^{-18},$$

where n_B and $n_{\bar{B}}$ are the number densities of the baryons and antibaryons in the universe, respectively [11]. Here, $n_B - n_{\bar{B}}$ is the number of baryons remaining in the current universe, and n_γ is the number of photons produced from the annihilation of baryons and antibaryons. The ratio of baryon density to photon density, obtained by the Planck space observatory, is given by $\sim 10^{-9}$ [7]. This large discrepancy between the theoretical calculation and observation suggests the existence of physical phenomena beyond the Standard Model.

1.1.4 T violation and the search for electric dipole moments

One of the experiments to search for CP violation for physics beyond the Standard Model is the search for the electric dipole moments (EDMs) of elementary particles. The existence of EDMs implies T violation, and based on the CPT theorem, this is synonymous with CP violation. The reason for the presence of the EDMs indicating the existence of T violation is explained as follows. The Hamiltonian of the interaction between a particle and an electromagnetic field is expressed in terms of a magnetic moment $\boldsymbol{\mu}$ and an EDM $\boldsymbol{d}$ as

$$H = -\boldsymbol{\mu} \cdot \boldsymbol{B} - \boldsymbol{d} \cdot \boldsymbol{E},$$

where $\boldsymbol{B}$ and $\boldsymbol{E}$ are the magnetic and electric fields, respectively. Under T transformation, $\boldsymbol{\mu}$, $\boldsymbol{B}$, $\boldsymbol{d}$, and $\boldsymbol{E}$ are transformed as $\boldsymbol{\mu} \to \boldsymbol{\mu}$, $\boldsymbol{B} \to -\boldsymbol{B}$, $\boldsymbol{d} \to -\boldsymbol{d}$, and $\boldsymbol{E} \to \boldsymbol{E}$, respectively, and the Hamiltonian H with the T transformation is

$$H = -\boldsymbol{\mu} \cdot \boldsymbol{B} + \boldsymbol{d} \cdot \boldsymbol{E},$$

If the value of $d = |\boldsymbol{d}|$ is nonzero, then the Hamiltonian H is changed by the T transformation. This indicates that a nonzero value of the EDM of the particles implies the existence of T violation.

Figure 1.1 shows the hierarchy of scales between the CP-odd sources and observable EDMs. The fundamental CP-odd phase results in the emergence of multiple EDMs via different paths at low-energy scales based on the effective field theory (EFT). EDMs may be observed in particles of various scales, such as electrons, muons, neutrons, nuclei, ions, atoms, and molecules, but thus far, they have not been discovered. Figure 1.2 shows the upper limits that have been obtained to date in the search for the neutron EDM, with the horizontal axis representing the year of publication [12–26]. The current upper limit of the neutron EDM d_n was obtained as

$$|d_\mathrm{n}| < 1.8 \times 10^{-26}\ \mathrm{e} \cdot \mathrm{cm}\ (90\%\ \mathrm{C.L.}),$$

through an experiment conducted at the Paul Scherrer Institute (PSI) [26]. During the past 60 years of experiments, six orders of magnitude have been covered, thereby imposing severe constraints on the theoretical model. The Standard Model prediction is less than 10^{-30}, but assuming theories such as the left–right symmetric and supersymmetric models, the discovery may be in the order of 10^{-27} or less [27].

1.2 Discrete symmetry violation in compound nucleus

A promising method to search for T violation is the use of neutron-induced compound nuclei. When a neutron is incident on a nucleus, the energy of the incident neutron is distributed to each nucleon in the nucleus and the nucleons repeatedly collide with each other. The energy exchanged between the nucleons is small such that approximately 10^{-16} s is required to release the excitation energy, which is much longer than the time required for a neutron to pass through the nucleus (10^{-22} s). Such a long excited state

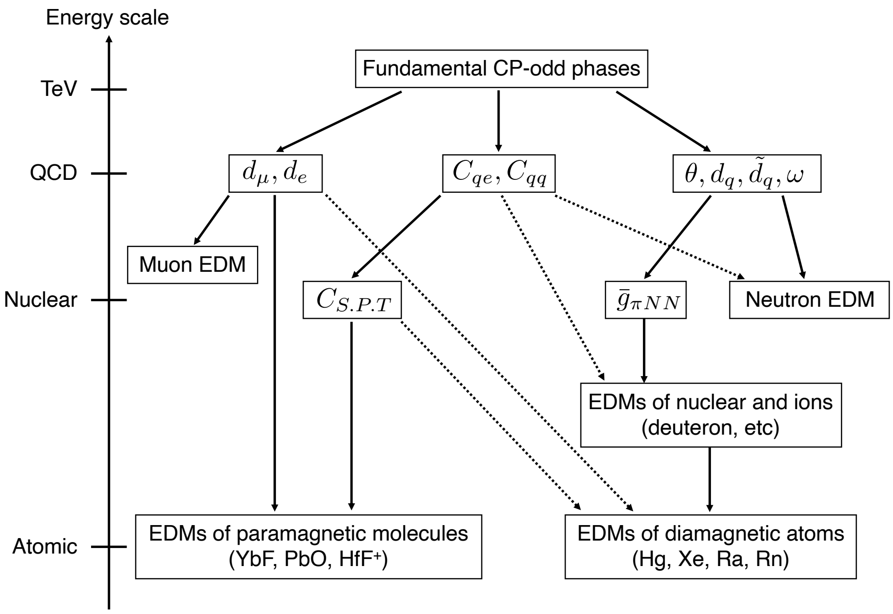

FIGURE 1.1: Schematic plot of the hierarchy of scales between the CP-odd sources and three generic classes of observable EDMs. The dashed lines indicate generically weaker dependencies [28].

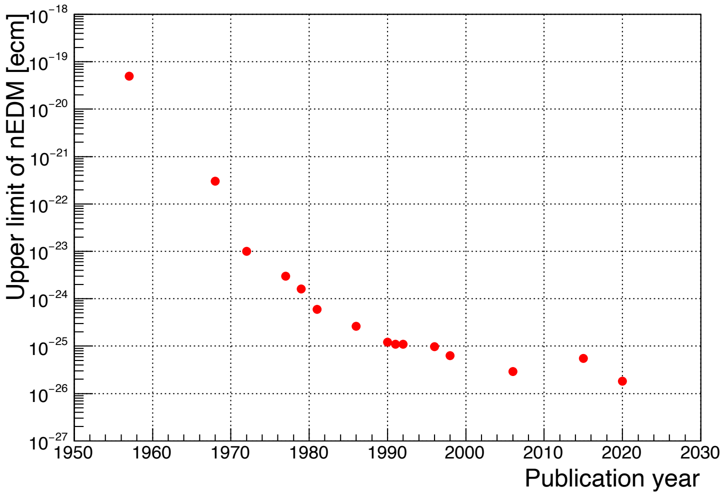

FIGURE 1.2: History of the upper limit of the neutron EDM [12–26].

can be considered a type of nucleus with a lifetime and can define internal degrees of freedom such as spin. The total angular momentum of the compound state, denoted by $\boldsymbol{J}$, is given by

$$\boldsymbol{J} = \boldsymbol{l} + \boldsymbol{s} + \boldsymbol{I},$$

where $\boldsymbol{l}$, $\boldsymbol{s}$, and $\boldsymbol{I}$ are the orbital angular momentums of the incident neutrons, spin of the incident neutrons, and target nuclear spin, respectively. Compound nuclear reactions are sensitive to the coupling constant of the pion exchange interactions between nucleons. Therefore, experimental searches using compound nuclear reactions are sensitive to the T-violating coupling constant, $\bar{g}_{\pi}NN$ (Fig. 1.1).

1.2.1 Enhancement of parity violation

In nucleon–nucleon interactions, where strong interactions dominate, the parity nonconserving (PNC) effect due to weak interactions is very small. The PNC effect in proton–proton scattering has been studied experimentally by several groups, where the longitudinal asymmetry of the scattering cross-section has been measured using a polarized proton beam and an unpolarized proton target. The longitudinal asymmetry $A_{\mathrm{L,pp}}$ is given by

$$A_{\mathrm{L,pp}} = \frac{\sigma_{\mathrm{pp}}^{+} - \sigma_{\mathrm{pp}}^{-}}{\sigma_{\mathrm{pp}}^{+} + \sigma_{\mathrm{pp}}^{-}},$$

where σ_{pp}^{+} and σ_{pp}^{-} are the total cross-sections for positive and negative helicity protons, respectively, on the target. The value of $A_{\mathrm{L,pp}}$ has been measured at several incident proton energies, and the values are approximately 10^{-7} [29–34].

Through measuring the helicity dependence of the neutron capture cross-section using a polarized neutron beam and an unpolarized target, a 10^{6} times larger P violation than that of proton–proton scattering was observed for a significant number of compound nuclei. A large P violation has been observed only in p-wave resonances ($l = 1$) located at the tail of s-wave resonances ($l = 0$) (Fig. 1.3). The P violation of compound nuclei is given by the following equation, as for proton–proton scattering:

$$A_{\mathrm{L}} = \frac{\sigma_{\mathrm{cap}}^{+} - \sigma_{\mathrm{cap}}^{-}}{\sigma_{\mathrm{cap}}^{+} + \sigma_{\mathrm{cap}}^{-}},$$

where $\sigma_{\mathrm{cap}}^{+}$ and $\sigma_{\mathrm{cap}}^{-}$ are the neutron-capture cross-sections of the target nucleus for positive- and negative-helicity neutrons, respectively. Figure 1.4 shows the experimental results of measuring the longitudinal asymmetry A_{L} of various nuclei summarized in Ref. [35].

Theoretically, the large P violation is explained as a result of interference between the s-wave and p-wave resonance amplitudes (s–p mixing), which enhances the P violation in nucleon–nucleon interactions. The angular momentum of the incident neutron $\boldsymbol{j}$ can be expressed as $\boldsymbol{j} = \boldsymbol{l} + \boldsymbol{s}$. The probability amplitude of the p-wave is one of the two states, $j = 1/2$ or $j = 3/2$, and the probability amplitude of the s-wave is the $j = 1/2$ state. Because nucleons can interact for a much longer time in the compound state than in the direct process, parity mixing between the s-wave and p-wave amplitudes can be much larger in the compound state than in the direct

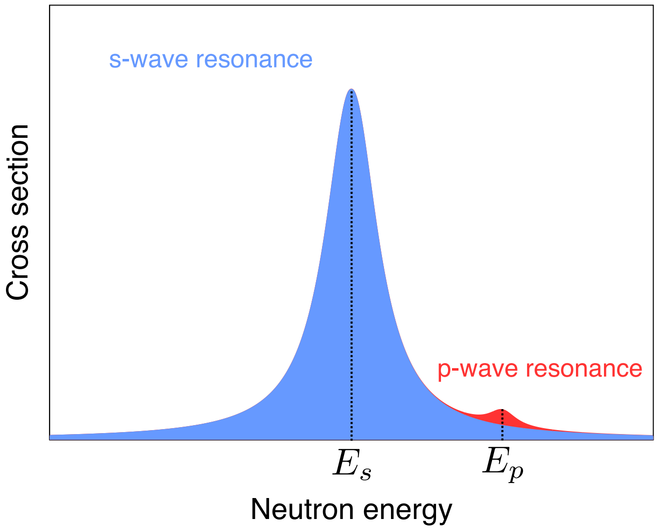

FIGURE 1.3: Schematic of a p-wave resonance located at the tail of a large s-wave resonance. A large P violation has been observed at such a p-wave resonance.

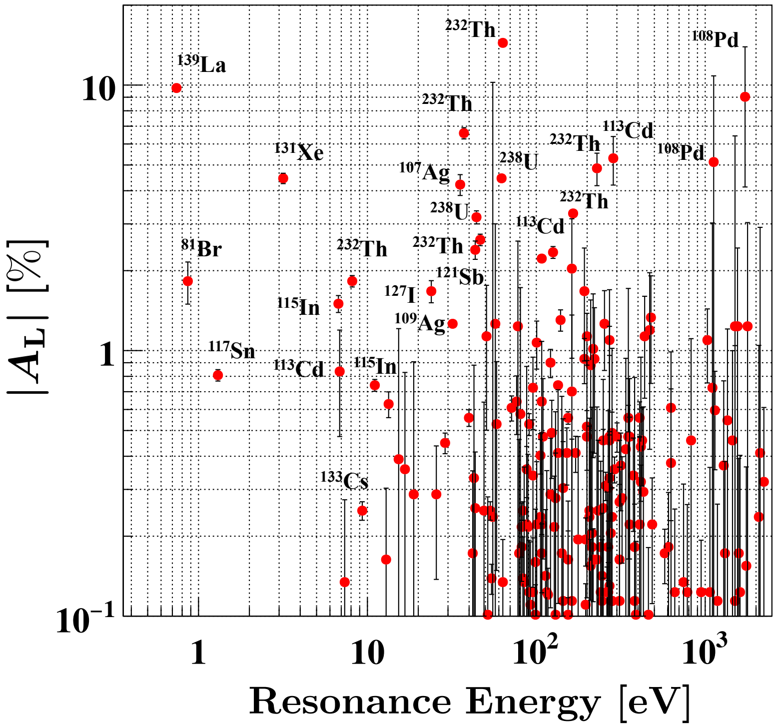

FIGURE 1.4: Longitudinal asymmetry $|A_\mathrm{L}|$ in various nuclei [35].

process. The longitudinal asymmetry A_{L} is theoretically expressed as

$$A_{\mathrm{L}} \simeq -\sum_{\mathrm{s}} \frac{2xW}{E_{\mathrm{p}}-E_{\mathrm{s}}}\sqrt{\frac{\Gamma^{\mathrm{n}}_{\mathrm{s}}}{\Gamma^{\mathrm{n}}_{\mathrm{p}}}}, \tag{1.1}$$

where E_{s} (E_{p}) is the resonance energy of the s-wave (p-wave) resonance, W is the weak matrix element, and $\Gamma^{\mathrm{n}}_{\mathrm{s}}$ ($\Gamma^{\mathrm{n}}_{\mathrm{p}}$) is the neutron width of the s-wave (p-wave) resonance [35]. The neutron widths $\Gamma^{\mathrm{n}}_{\mathrm{s}}$ and $\Gamma^{\mathrm{n}}_{\mathrm{p}}$ are expressed as

$$\Gamma^{\mathrm{n}}_{\mathrm{s}} = \Gamma^{\mathrm{n}}_{\mathrm{s},j=\frac{1}{2}}, \quad \Gamma^{\mathrm{n}}_{\mathrm{p}} = \Gamma^{\mathrm{n}}_{\mathrm{p},j=\frac{1}{2}} + \Gamma^{\mathrm{n}}_{\mathrm{p},j=\frac{3}{2}}.$$

Here, x in Eq. 1.1 is given by $x \equiv \sqrt{\Gamma^{\mathrm{n}}_{\mathrm{p},j=1/2}/\Gamma^{\mathrm{n}}_{\mathrm{p}}}$. The summation symbol $\sum$ refers to the sum of the contributions of several s-wave resonances with the same J in the vicinity of p-wave resonance. The derivation of A_{L} is explained in Appendix A.

The enhancement mechanism of A_{L} can be divided into two components: "dynamic enhancement" and "structural enhancement." The dynamical enhancement results from the statistical properties of the composite nuclear state. The wave functions of the s-wave and p-wave can be described as an expansion of a number of single particle–hole states in a nuclear shell model, given as follows:

$$|\mathrm{s}\rangle = \sum_{i}^{N} a_i |i\rangle \text{ and } |\mathrm{p}\rangle = \sum_{j}^{N} b_j |j\rangle,$$

where $|i\rangle$ and $|j\rangle$ are the wave functions of the single particle–hole states. The magnitudes of the coefficients a_i and b_j are in the order of $\sim 1/\sqrt{N}$ because of the normalization of the wave functions $|\mathrm{s}\rangle$ and $|\mathrm{p}\rangle$. The number of states N is estimated as

$$N \sim \frac{\Delta E}{D},$$

where ΔE is the energy required to excite one nucleus from the ground state, and D is the energy difference between the states. Typical values of ΔE and D are $\Delta E \sim 10^6$ eV and $D \sim 10$ eV, respectively, and the value of N is estimated to be $\sim 10^5$. Subsequently, the weak matrix element W is described as

$$\begin{aligned}
|W| &= |\langle \mathrm{s}\,|H_{\mathrm{PNC}}|\,\mathrm{p}\rangle| \\
&= \left|\sum_{ij}^{N} a_i^* b_j \langle i\,|H_{\mathrm{PNC}}|\,j\rangle\right| \\
&\sim \frac{\langle i\,|H_{\mathrm{PNC}}|\,j\rangle}{N} \times \sqrt{N},
\end{aligned}$$

where H_{PNC} is the Hamiltonian of PNC interactions. Therefore, $2W/(E_{\mathrm{p}}-E_{\mathrm{s}})$ in Eq. 1.1 is expressed as

$$\frac{2W}{E_{\mathrm{p}}-E_{\mathrm{s}}} \sim \frac{|W|}{D} \sim \frac{\overline{\langle i\,|H_{\mathrm{PNC}}|\,j\rangle}}{\Delta E}\sqrt{N} \tag{1.2}$$

The magnitude of the structural enhancement, which is $\sqrt{\Gamma^{\mathrm{n}}_{\mathrm{s}}/\Gamma^{\mathrm{n}}_{\mathrm{p}}}$ in Eq. 1.1, is estimated as follows: The neutron width is proportional to a factor of the centrifugal potential, $(kR)^{2l+1}$, where k is the neutron momentum, and R is the radius of the nucleus. By substituting $k \sim 2 \times 10^{-4}$ fm^{-1} and $R \sim 10$ fm, this factor is $\sim 10^3$. If x is in the order of 1, the longitudinal asymmetry A_{L} is approximately 10^{-1}. However, the values of x for various nuclei have not yet been experimentally determined.

1.2.2 Enhancement of T violation

V. P. Gudkov predicted that T violation is also enhanced by the same mechanism as that of P violation described in the previous section [36]. This effect can be studied by measuring the T violation cross-sections of neutron captures. The wave function of the compound nucleus $|J\rangle = |lsI\rangle$ is transformed into $(-1)^l\,|lsI\rangle$ via a P transformation. However, it is transformed into $e^{i\pi S_y}\hat{K}\,|lsI\rangle$ in a T transformation [37]. Here, $\hat{K}$ is the complex conjugate matrix and S_y is the y-component of the channel spin S described as $\boldsymbol{S} = \boldsymbol{s} + \boldsymbol{I}$. This means that the T violation is caused by interference between states with different channel spins in compound nuclear states.

The wave function of the compound nucleus can be expanded using the Clebsch—Gordan coefficients, as follows:

$$\begin{aligned} |J(l,S(sI))\rangle &= \sum_j \langle\langle J(j(ls),I) \mid J(l,S(sI))\rangle \mid J(j(ls),I)\rangle \\ &= \sum_j (-1)^{l+s+I+J}\sqrt{(2j+1)(2S+1)} \left\{ \begin{array}{ccc} I & s & l \\ I & S & j \end{array} \right\} |J\left(j\left(l_s\right),I\right)\rangle . \end{aligned}$$

Now, extracting only the relevant characters, it is rewritten as follows:

$$|S\rangle = \sum_j (-1)^{l+s+I+J}\sqrt{(2j+1)(2S+1)} \left\{ \begin{array}{ccc} I & s & l \\ I & S & j \end{array} \right\} |j\rangle .$$

The relative magnitude of the T violation cross-section $\Delta\sigma_T$ to the P violation cross-section $\Delta\sigma_P$ can be described as follows:

$$\begin{aligned} \frac{\Delta\sigma_{\mathrm{T}}}{\Delta\sigma_{\mathrm{P}}} &= \frac{\langle S\,|H_{\mathrm{TRTV}}|\,S'\rangle}{\langle \mathrm{s}\,|H_{\mathrm{PNC}}|\,\mathrm{p}\rangle} \\ &= \kappa(J)\frac{\langle \mathrm{s}\,|H_{\mathrm{TRIV}}|\,\mathrm{p}\rangle}{\langle \mathrm{s}\,|H_{\mathrm{PNC}}|\,\mathrm{p}\rangle} \\ &= \kappa(J)\frac{W_{\mathrm{T}}}{W}, \\ \Delta\sigma_{\mathrm{T}} &= \kappa(J)\frac{W_{\mathrm{T}}}{W}\Delta\sigma_{\mathrm{P}}, \end{aligned} \tag{1.3}$$

where H_{TRIV} is the Hamiltonian of time-reversal invariance violating (TRIV) interactions, and W_{T} and W are the T-violating and P-violating matrix elements, respectively. $\kappa(J)$ is the spin factor, which can be expressed as [38]

$$\kappa(J) = \begin{cases} (-1)^{2I}\left(1 + \frac{1}{2}\sqrt{\frac{2I-1}{I+1}\frac{y}{x}}\right) & \left(J = I - \frac{1}{2}\right) \\ (-1)^{2I+1}\frac{I}{I+1}\left(1 - \frac{1}{2}\sqrt{\frac{2I+3}{I}\frac{y}{x}}\right) & \left(J = I + \frac{1}{2}\right) \end{cases}, \tag{1.4}$$

where x and y are defined as

$$x^2 = \frac{\Gamma^{\mathrm{n}}_{\mathrm{p},j=\frac{1}{2}}}{\Gamma^{\mathrm{n}}_{\mathrm{p}}} \text{ and } y^2 = \frac{\Gamma^{\mathrm{n}}_{\mathrm{p},j=\frac{3}{2}}}{\Gamma^{\mathrm{n}}_{\mathrm{p}}},$$

TABLE 1.1: Candidate nuclei for T violation search in the vicinity of 1 eV. The nuclei whose P violation was observed with over 2σ and whose nuclear spins I are nonzero are listed. The values of $\kappa(J)$ have statistical errors of 1σ.

	E_{p}[eV]	A_{L}[%]	I	Abundance [%]	Polarization method	$\|\kappa(J)\|$
^{139}La	0.758	9.8 ± 0.2	7/2	99.91	DNP [41]	$1.62^{+2.60}_{-0.95}$ [39, 42]
^{81}Br	0.88	0.77 ± 0.33	3/2	49.31	–	–
^{117}Sn	1.327	0.79 ± 0.04	1/2	7.68	–	$0.42^{+0.05}_{-0.06}$ or $2.6^{+6.8}_{-1.3}$ [40]

and x and y satisfy $x^2 + y^2 = 1$ because of the relationship $\Gamma^{\mathrm{n}}_{\mathrm{p}} = \Gamma^{\mathrm{n}}_{\mathrm{p},j=\frac{1}{2}} + \Gamma^{\mathrm{n}}_{\mathrm{p},j=\frac{3}{2}}$. In addition, x and y have the following relationship using the mixing angle ϕ:

$$x = \cos\phi \text{ and } y = \sin\phi.$$

If the value of $\kappa(J)$ is nonzero, Eq. 1.3 implies that the enhancement effect of the T violation may be observed in the compound nucleus where the enhancement effect of the P violation has already been observed.

1.2.3 Candidate nuclei for a target of the T violation search

The experimental sensitivity of the T violation search depends on the target nucleus. Nuclei that satisfy the following conditions are given high priority as candidates for the target of the experiment:

1. Large longitudinal asymmetry A_{L}.
2. Large value of $|\kappa(J)|$.
3. Spin polarization is possible (nuclear spin $I \neq 0$).

The value of $|\kappa(J)|$ can be determined using experiments focusing on p-wave resonance, as described in the following chapters. From the perspective of ease of conducting experiments to determine the $|\kappa(J)|$ values, the following two conditions are added to the list of candidate target nuclei.

4. Low p-wave resonance energy at which P violation occurs.
5. Large natural abundance ratio.

The value of $|\kappa(J)|$ was first determined in 2018 by T. Okudaira *et. al.* for ^{139}La [39] and then by J. Koga for ^{117}Sn in 2021 [40]. Information on the candidate nuclei with p-wave resonances in the vicinity of 1 eV is summarized in Tab. 1.1. Currently, ^{139}La is the first candidate for the T violation search.

The nucleus shown in Tab. 1.1 satisfies the fourth of the five aforementioned conditions. However, most of the p-wave resonances in which A_{L} has been observed exist in the region above 1 eV. Therefore, the establishment of research methods for the region above 1 eV will rapidly expand the field of compound nucleus research. Nuclei with p-wave resonances at energies higher than those listed in Tab. 1.1, up to 10 eV, are summarized in Tab. 1.2. Figure 1.5 shows the correlations between $|\kappa(J)|$ and ϕ for candidate nuclei listed in Tab. 1.1 and Tab. 1.2.

TABLE 1.2: Candidate nuclei for T violation search in the energy region from 1 to 10 eV. The nuclei whose P violation was observed with over 2σ and whose nuclear spins I are nonzero are listed.

	E_p[eV]	A_L[%]	I	Abundance [%]	Polarization method	$\kappa(J)$
^{131}Xe	3.2	4.3 ± 0.2	3/2	21.2	SEOP[43]	–
^{115}In	6.853	-1.45 ± 0.11	9/2	95.72	Brute force [44], DNP [45], DYNASP [46]	–
^{113}Cd	7.00	-0.80 ± 0.33	3/2	12.22	–	–
^{133}Cs	9.50	0.24 ± 0.02	7/2	100	–	–

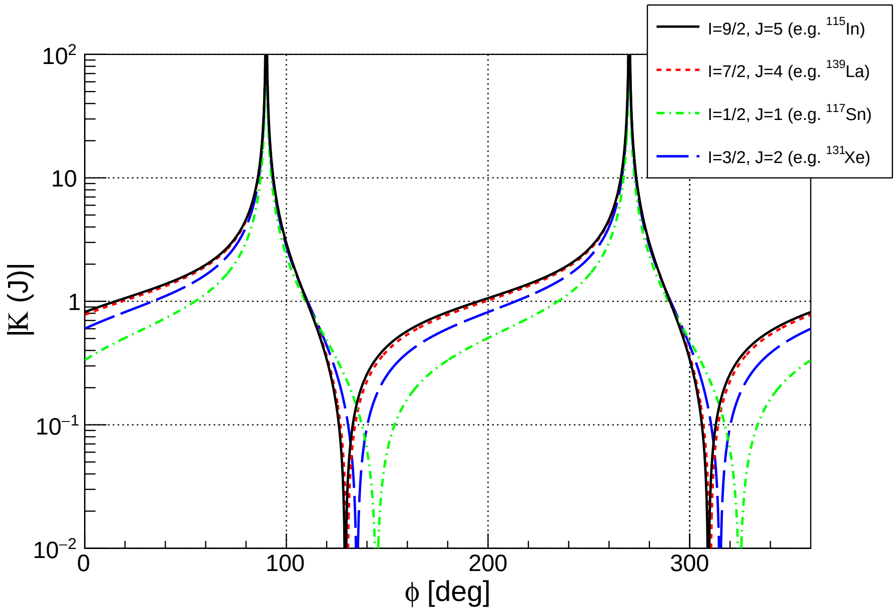

FIGURE 1.5: Correlations between $|\kappa(J)|$ and ϕ for candidate nuclei.

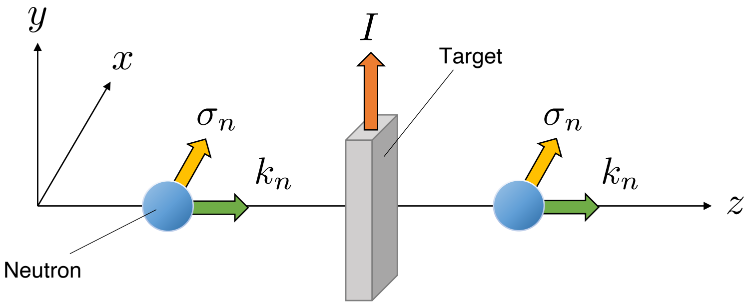

FIGURE 1.6: Measurement principle of the D term with polarized neutrons and a polarized target.

1.3 Experimental principle of the T violation search in the epithermal region

As discussed in the previous section, the T violation effect can be enhanced by the same mechanism as the P violation effect; therefore, T violation can be searched with high sensitivity using experiments using compound nuclei. The neutron forward scattering amplitude f depends on the directions of the neutron spin $\boldsymbol{\sigma}_{\mathbf{n}}$, nucleus spin $\boldsymbol{I}$, and neutron momentum $\hat{\boldsymbol{k}}_{\mathbf{n}}$, and it can be expressed as

$$f = A + B\left(\boldsymbol{\sigma}_{\mathbf{n}} \cdot \boldsymbol{I}\right) + C\left(\boldsymbol{\sigma}_{\mathbf{n}} \cdot \hat{\boldsymbol{k}}_{\mathbf{n}}\right) + D\left(\boldsymbol{\sigma}_{\mathbf{n}} \cdot \left(\boldsymbol{I} \times \hat{\boldsymbol{k}}_{\mathbf{n}}\right)\right). \tag{1.5}$$

The coefficient A is a spin-independent (P-even, T-even) term corresponding to the neutron capture cross-section. The coefficient B is a spin-dependent (P-even, T-even) term corresponding to the spin rotation of the neutron through the polarized target, called the "pseudomagnetic effect." The coefficient C is the P-violating (P-odd, T-even) term, which is enhanced in some of the nuclei mentioned earlier. The coefficient D is the T-violating (P-odd, T-odd) term, which corresponds to the T-violating cross-section in Eq. 1.3. Therefore, a nonzero value of D implies the existence of T violation. Note that Eq. 1.5 is in the form $I = 1/2$. For $I > 1/2$, a tensor term must be added to the forward-scattering amplitude. However, the contribution of the tensor term is generally smaller than that of the other terms and is ignored in this thesis to approximate the D term. Figure 1.6 schematically shows the measurement principle of the D term. The coordinate system is defined as the z-axis for the beam axis, the y-axis for the vertical direction, and the x-axis for the direction perpendicular to them. The measurement of the D term requires a polarized neutron beam and a polarized nuclear target. The specific method for measuring the D term is described in Chap. 6.

The following subsections explain the contents of this thesis. In Sec. 1.3.1, indium nuclei are proposed as the target nuclei and the reasons for this are explained. In Sec. 1.3.2, several instruments for neutron polarization are introduced, the instruments adopted in this study are briefly described, and the reason is explained.

1.3.1 Properties of ^{115}In

As explained in Sec. 1.2.3, the establishment of research methods for the region above 1 eV will rapidly expand the field of compound nucleus research. However, resonant states are generally clustered within a narrow energy interval in the region of high incident neutron energy. Among the nuclei listed in Tab. 1.2, the nucleus of

TABLE 1.3: Resonance parameters of ^{115}In summarized in [47].

r	E_0 [eV]	J	l	$2g\Gamma_\mathrm{n}$ [meV]	Γ_γ [meV]
1	1.457 ± 0.002	5	0	3.28 ± 0.06	72 ± 2
2	3.85 ± 0.01	4	0	0.339 ± 0.013	81 ± 4
3	6.853 ± 0.009	5	1	0.00046 ± 0.00004	-
4	9.07 ± 0.04	5	0	1.69 ± 0.12	80 ± 40

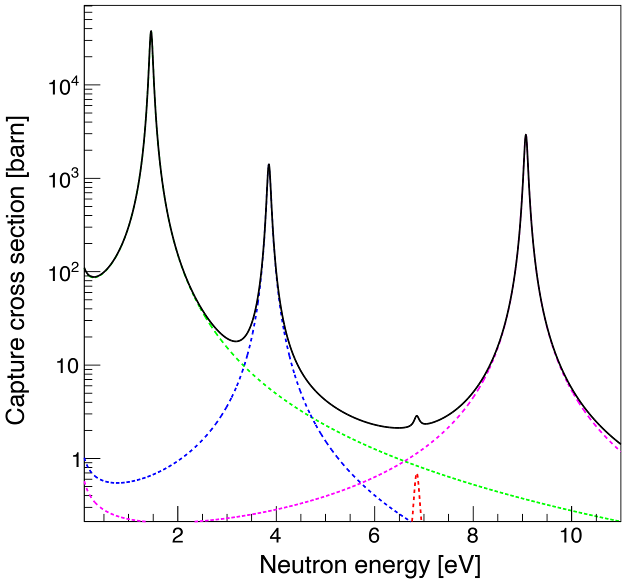

FIGURE 1.7: Capture cross-sections for each resonance of ^{115}In.

^{115}In is suitable as a first step in extending the field of compound nucleus research to the energy region above 1 eV. The respective resonance parameters for the p-wave resonance of ^{115}In and some of its immediate s-wave resonances are summarized in Tab. 1.3, and the capture cross-sections drawn by substituting these resonance parameters into the Breit–Wigner function are shown in Fig. 1.7. The dotted lines represent each resonance and the solid line represents their sum. In the energy region around 6.85 eV, where p-wave resonance exists, the respective contributions of the 1.46 eV and 9.07 eV s-wave resonances are both approximately 1 barn, which is almost the same. Measurements and data analyses that consider the contributions of multiple s-wave resonances such as ^{115}In are a basis for studying nuclei with p-wave resonances in the high-energy region.

Additional information on ^{115}In is provided: The natural abundance of ^{115}In is 95.7%, and the only other stable isotope is ^{113}In, which enables us to perform measurements with low contamination. The value of the nuclear spin is $I = 9/2$, and ^{115}In has been polarized using several techniques [44–46]. The compound nucleus state of $^{115}\mathrm{In} + \mathrm{n}$ is an excited state with a neutron separation energy of $S_n = 6784.7$ keV. Thus, the compound nucleus deexcites to the ground state by emitting one or more γ-rays. Figure 1.8 shows the level scheme of the $^{115}\mathrm{In}(\mathrm{n},\gamma)^{116}\mathrm{In}$ reaction. The energies of the γ-rays emitted from the compound nucleus are summarized in Tab. 1.4 only for the γ-rays whose final state spin F is known from previous studies [48, 49], in other words, only for high-intensity γ-rays. This thesis reports the values of ϕ and $\kappa(J)$ for ^{115}In.

TABLE 1.4: List of energy state of $^{116}\mathrm{In}^*$ until 1000 keV, final state spins of these states, and the energies of the γ-rays emitted from these states [48, 49]. S_n is the neutron separation energy of the compound nucleus. The γ-ray energies are calculated as the difference between S_n and each energy level.

$S_n = 6784.7$ [keV]

Level [keV]	Final state spin F	γ-ray energy [keV]
0.0	1	6784.7
127.3	5	6657.4
223.3	4	6561.4
273.0	2	6511.7
289.7	8	6495.0
313.5	5	6471.2
350.6	7	6434.1
373.4	6	6411.3
425.9	4	6358.8
458.9	5	6325.8
508.2	3	6276.5
555.0	4	6229.7
556.8	2	6227.9
648.9	6	6135.8
658.1	3	6126.6
790.9	3	5993.8
813.3	4	5971.4
829.1	4	5955.6
850.5	3	5934.2
875.3	3	5909.4
892.7	4	5892.0
951.5	4	5833.2

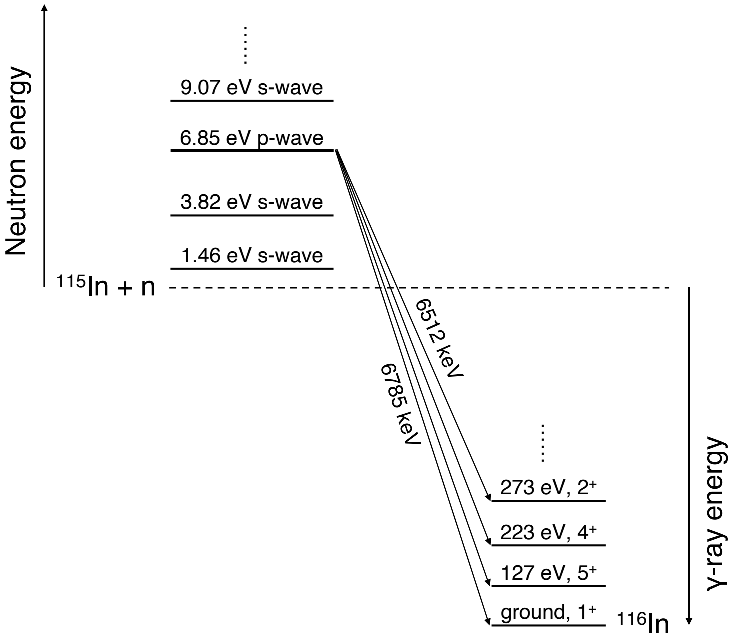

FIGURE 1.8: Transitions from ^{115}In + n to ^{116}In.

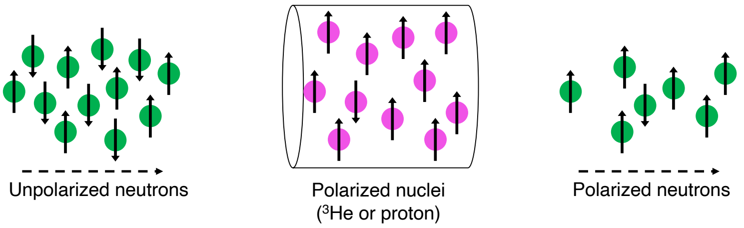

FIGURE 1.9: Polarization principle of neutrons with the neutron spin filter.

1.3.2 Polarization method of neutrons

Polarized neutrons are widely used in particle physics, nuclear physics, condensed-matter physics, and the industry. Depending on the neutron energy, polarization mirrors and neutron spin filters are used to polarize the neutrons. Polarization mirrors are used for neutrons with energies below 20 meV, whereas neutron spin filters are used for neutrons with energies above 20 meV. Neutron spin filters are suitable for the experiment shown in Fig. 1.6. Neutron spin filters rely on the spin-dependent cross-section of nuclear capture in polarized ^{3}He nuclei or scattering on polarized protons (Fig. 1.9).

A neutron spin filter using polarized ^{3}He nuclei, which is called a ^{3}He spin filter, is more suitable for use at lower energies in the epithermal region because the neutron–^{3}He capture cross-section is larger at lower energies owing to the $1/v$ law. The ^{3}He nuclei can be polarized using spin exchange optical pumping (SEOP) [50, 51], or meta-stability optical pumping (MEOP) [52], which uses a circularly polarized laser. The ^{3}He spin filter is already available at several neutron experimental facilities [53–55]. However, the energy-dependent neutron capture cross-section of ^{3}He enables the optimization of the filter size for a wide range of epithermal regions.

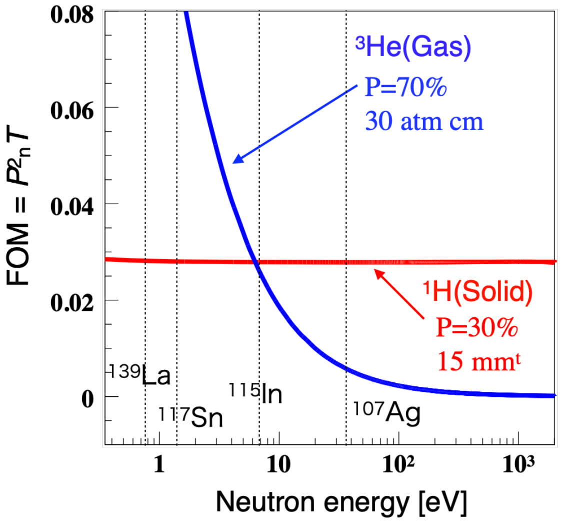

FIGURE 1.10: Comparison of the performance of the proton spin filter (red) and ^{3}He spin filter (blue).

A neutron spin filter using polarized protons, called a proton spin filter, can polarize neutrons with energies up to keV because the neutron-–proton scattering cross-section is nearly constant in the epithermal region [56]. The protons can be polarized using dynamic nuclear polarization (DNP), which is a microwave irradiation technique that can transfer the polarization of electrons to protons [57, 58]. DNP relies on the thermally equilibrated high polarization of electrons, which is added to samples as polarizing agents and is realized at cryogenic temperatures ($\sim$ 1 K) and with a strong magnetic field (2.5 T to 5 T). Historically, the proton spin filter was developed earlier than the ^{3}He spin filter. However, in addition to the aforementioned strict environment, the neutron flux in pulsed neutron sources is higher for thermal neutrons (meV to eV) than for epithermal neutrons; thus, the polarized ^{3}He spin filter was gradually preferred over the polarized proton spin filter. Today, no proton spin filters are permanently installed in pulsed neutron sources. Recently, polarized proton spin filters have been in demand owing to the advent of megawatt-class pulsed neutron sources. This thesis reports on the polarization of epithermal neutrons achieved using a proton polarization method that is different from conventional DNP.

Based on the suitability of each spin filter for the incident neutron energy, different spin filters were used in the experiment shown in Fig. 1.6 depending on the target nucleus. For reference, Fig. 1.10 shows a comparison of the figure of merit (FOM) of the two spin filters as a function of the neutron energy. The value of the FOM is a statistically relevant factor in the optimization of the spin-filter performance [59], and a specific definition is obtained in Chap. 5.

1.4 Organization of this thesis

In Chap. 1, the research motivation in this thesis is outlined. Chapter 2 explains the theory of the cross-sections of (n,γ) reactions based on the mixing of the s-wave and p-wave resonances. The method of determining the ϕ value is also described in this chapter. In Chap. 3 and 4, an experimental facility for the (n,γ) reaction and the analysis method of the ϕ and $\kappa(J)$ values are explained. Chapter 5 describes the proton polarization method and the development of a polarization device for epithermal neutrons based on this method. Chapter 6 discusses the further advancement of the results from this study. Finally, Chap. 7 summarizes this thesis.

Chapter 2

Method to determine ϕ value

In this chapter, an expression describing the cross-sections of (n,γ) reactions is explained based on a mixing theory of the amplitudes of the s- and p-wave resonances. This formalism includes the mixing angle ϕ, which is a parameter that determines $\kappa(J)$.

2.1 Formalism of cross-sections of (n,γ) reactions

Based on the observation of the strong amplification of the P-odd effect in the p-wave resonance of compound nuclei, the P-even and P-odd correlations in (n,γ) reactions were formulated by V. V. Flambaum in 1985 [60]. Figure 2.1 shows simplified Feynman diagrams of the (n,γ) reaction. In each diagram, the left side shows a nucleus with mass number A absorbing a neutron (entrance channel), and the right side shows the final state of the reaction, which is a nucleus with mass number $A+1$ and a γ-ray (exit channel). A line connecting the initial and the exit channel vertexes signifies the compound nucleus. The coupling constants are indicated beside each vertex, and the propagation function is indicated immediately below the line representing the compound nuclear state. Figures 2.1(a) and (b) show the processes for PC, and (c) and (d) show the processes for PNC. W in (c) and (d) represents the weak matrix element. In the processes of Fig. 2.1(a) and (b), the resonance states of the nuclei and neutrons are formed as an s-wave and a p-wave in the entrance channel and remain in this state until the exit channel. The compound nucleus then deexcites, emits γ-rays, and settles in the ground state. In processes of Fig. 2.1(c) and (d), the compound nuclear state formed in the entrance channel changes owing to weak interactions, and the orbital angular momentum l in the exit channel changes by 1 relative to the entrance channel. In other words, the s-wave (p-wave) state in the entrance channel changes to the p-wave (s-wave) state in the exit channel.

The amplitude of the (n,γ) reaction is considered from the diagrams based on the Feynman rules. The probability amplitudes of the interaction processes corresponding to (a) to (d) are expressed in the following equations from f_1 to f_4:

$$\begin{aligned}
f_1 &= -\frac{1}{2k}\sum_{\mathrm{s}} \frac{\langle f,\gamma\,|H_{\mathrm{EM}}|\,\mathrm{s}\rangle\,\langle \mathrm{s}\,|H_{\mathrm{s}}|\,\mathrm{n}\rangle}{E_{\mathrm{n}}-E_{\mathrm{s}}+i\Gamma_{\mathrm{s}}/2}, \\
f_2 &= -\frac{1}{2k}\sum_{\mathrm{p}} \frac{\langle f,\gamma\,|H_{\mathrm{EM}}|\,\mathrm{p}\rangle\,\langle \mathrm{p}\,|H_{\mathrm{s}}|\,\mathrm{n}\rangle}{E_{\mathrm{n}}-E_{\mathrm{p}}+i\Gamma_{\mathrm{p}}/2}, \\
f_3 &= -\frac{1}{2k}\sum_{\mathrm{s,p}} \frac{\langle f,\gamma\,|H_{\mathrm{EM}}|\,\mathrm{p}\rangle\,\langle \mathrm{p}\,|H_{\mathrm{w}}|\,\mathrm{s}\rangle\,\langle \mathrm{s}\,|H_{\mathrm{s}}|\,\mathrm{n}\rangle}{(E_{\mathrm{n}}-E_{\mathrm{p}}+i\Gamma_{\mathrm{p}}/2)\,(E_{\mathrm{n}}-E_{\mathrm{s}}+i\Gamma_{\mathrm{s}}/2)}, \\
f_4 &= -\frac{1}{2k}\sum_{\mathrm{s,p}} \frac{\langle f,\gamma\,|H_{\mathrm{EM}}|\,\mathrm{s}\rangle\,\langle \mathrm{s}\,|H_{\mathrm{w}}|\,\mathrm{p}\rangle\,\langle \mathrm{p}\,|H_{\mathrm{s}}|\,\mathrm{n}\rangle}{(E_{\mathrm{n}}-E_{\mathrm{s}}+i\Gamma_{\mathrm{s}}/2)\,(E_{\mathrm{n}}-E_{\mathrm{p}}+i\Gamma_{\mathrm{p}}/2)},
\end{aligned}$$

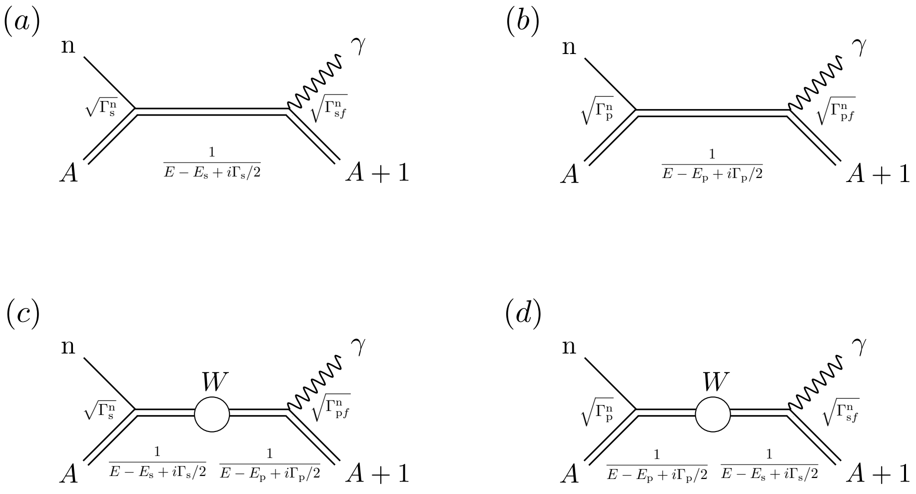

FIGURE 2.1: Diagrams for each state of the (n,γ) reaction. (a) and (b) Processes in for parity conservation, and (c) and (d) processes for of parity non-conservation.

where k is the momentum of the neutron, $E_{\rm n}$ is the kinetic energy of the neutron, and $E_{\rm r}$ and $\Gamma_{\rm r}$ are the energy and width of a neutron resonance $\mathrm{r} = \mathrm{s}$ or p, respectively. $H_{\rm s}$, $H_{\rm w}$, and $H_{\rm EM}$ are the Hamiltonians of the residual interaction, which are responsible for neutron capture, weak interaction, and electromagnetic interaction, respectively. The wave functions $|\mathrm{n}\rangle$ and $|f,\gamma\rangle$ are the initial state of the neutron and final state of the nucleus and γ-ray, respectively. The amplitude from V_1 to V_4 is newly defined using experimental parameters instead of bracket notation:

$$\begin{aligned}
V_1\left(E_{\rm n}, J_{\rm s}\right) &= -\frac{1}{2k}\sum_{\rm s}\frac{\sqrt{g_{\rm s}\Gamma^{\rm n}_{\rm s}\Gamma^{\gamma}_{{\rm s},f}}}{E_{\rm n}-E_{\rm s}+i\Gamma_{\rm s}/2},\\
V_2\left(E_{\rm n}, J_{\rm p}\right) &= -\frac{1}{2k}\sum_{\rm p}\frac{\sqrt{g_{\rm p}\Gamma^{\rm n}_{\rm p}\Gamma^{\gamma}_{{\rm p},f}}}{E_{\rm n}-E_{\rm p}+i\Gamma_{\rm p}/2},\\
V_3\left(E_{\rm n}, J_{\rm s}=J_{\rm p}\right) &= -\frac{1}{2k}\sum_{\rm s,p}\frac{\sqrt{g_{\rm s}\Gamma^{\rm n}_{\rm s}}W\sqrt{\Gamma^{\gamma}_{{\rm p},f}}}{\left(E_{\rm n}-E_{\rm p}+i\Gamma_{\rm p}/2\right)\left(E_{\rm n}-E_{\rm s}+i\Gamma_{\rm s}/2\right)},\\
V_4\left(E_{\rm n}, J_{\rm p}=J_{\rm s}\right) &= -\frac{1}{2k}\sum_{\rm s,p}\frac{\sqrt{g_{\rm p}\Gamma^{\rm n}_{\rm p}}W\sqrt{\Gamma^{\gamma}_{{\rm s},f}}}{\left(E_{\rm n}-E_{\rm s}+i\Gamma_{\rm s}/2\right)\left(E_{\rm n}-E_{\rm p}+i\Gamma_{\rm p}/2\right)}.
\end{aligned}$$

where $\Gamma^{\rm n}_{\rm r}$ is the neutron width, $\Gamma^{\gamma}_{{\rm r},f}$ is the partial γ width of the transition to the final state f, and W is the weak matrix element. They are expressed as the coupling constants in Fig. 2.1. The statistical factor $g_{\rm r}$ is described using the nuclear spin I and total spin of the compound state of the resonance r:

$$g_{\rm r} = \frac{2J_{\rm r}+1}{2(2I+1)}.$$

Here, the resonance width $\Gamma_{\rm r}$ has the following relationship

$$\Gamma_{\rm r} = \Gamma^{\rm n}_{\rm r} + \Gamma^{\gamma}_{\rm r}$$

$$\Gamma^{\gamma}_{\mathrm{r}} = \sum_{f} \Gamma^{\gamma}_{\mathrm{r},f}$$
$$\Gamma^{\gamma}_{\mathrm{r},f} = B_{\mathrm{r},f}\Gamma^{\gamma}_{\mathrm{r}},$$

where $B_{\mathrm{r},f}$ is the transition ratio to a certain final state, and $\sum_f B_{\mathrm{r},f} = 1$.

The differential cross-section of the (n,γ) reaction is expressed as

$$\begin{aligned}
\frac{d\sigma}{d\Omega} &= \frac{1}{2}\Bigg[a_0 + a_1\boldsymbol{k}_\mathbf{n}\cdot\boldsymbol{k}_\gamma + a_2\boldsymbol{\sigma}_\mathbf{n}\cdot(\boldsymbol{k}_\mathbf{n}\times\boldsymbol{k}_\gamma) + a_3\left((\boldsymbol{k}_\mathbf{n}\cdot\boldsymbol{k}_\gamma)^2 - \frac{1}{3}\right)\\
&+ a_4(\boldsymbol{k}_\mathbf{n}\cdot\boldsymbol{k}_\gamma)(\boldsymbol{\sigma}_\mathbf{n} + (\boldsymbol{k}_\mathbf{n}\times\boldsymbol{k}_\gamma)) + a_5(\boldsymbol{\sigma}_\gamma\cdot\boldsymbol{k}_\gamma)(\boldsymbol{\sigma}_\mathbf{n}\cdot\boldsymbol{k}_\gamma)\\
&+ a_6(\boldsymbol{\sigma}_\gamma\cdot\boldsymbol{k}_\gamma)(\boldsymbol{\sigma}_\mathbf{n}\cdot\boldsymbol{k}_\mathbf{n}) + a_7(\boldsymbol{\sigma}_\gamma\cdot\boldsymbol{k}_\gamma)\left((\boldsymbol{\sigma}_\mathbf{n}\cdot\boldsymbol{k}_\gamma)(\boldsymbol{k}_\gamma\cdot\boldsymbol{k}_\mathbf{n}) - \frac{1}{3}(\boldsymbol{\sigma}_\mathbf{n}\cdot\boldsymbol{k}_\mathbf{n})\right)\\
&+ a_8(\boldsymbol{\sigma}_\gamma\cdot\boldsymbol{k}_\gamma)\left((\boldsymbol{\sigma}_\mathbf{n}\cdot\boldsymbol{k}_\mathbf{n})(\boldsymbol{k}_\mathbf{n}\cdot\boldsymbol{k}_\gamma) - \frac{1}{3}(\boldsymbol{\sigma}_\mathbf{n}\cdot\boldsymbol{k}_\gamma)\right)\\
&+ a_9\boldsymbol{\sigma}_\mathbf{n}\cdot\boldsymbol{k}_\gamma + a_{10}\boldsymbol{\sigma}_\mathbf{n}\cdot\boldsymbol{k}_\mathbf{n} + a_{11}\left((\boldsymbol{\sigma}_\mathbf{n}\cdot\boldsymbol{k}_\gamma)(\boldsymbol{k}_\gamma\cdot\boldsymbol{k}_\mathbf{n}) - \frac{1}{3}(\boldsymbol{\sigma}_\mathbf{n}\cdot\boldsymbol{k}_\mathbf{n})\right)\\
&+ a_{12}(\boldsymbol{\sigma}_\mathbf{n}\cdot\boldsymbol{k}_\mathbf{n})\left((\boldsymbol{k}_\mathbf{n}\cdot\boldsymbol{k}_\gamma) - \frac{1}{3}(\boldsymbol{\sigma}_\mathbf{n}\cdot\boldsymbol{k}_\gamma)\right)\\
&+ a_{13}\boldsymbol{\sigma}_\gamma\cdot\boldsymbol{k}_\gamma + a_{14}(\boldsymbol{\sigma}_\gamma\cdot\boldsymbol{k}_\gamma)(\boldsymbol{k}_\mathbf{n}\cdot\boldsymbol{k}_\gamma)\\
&+ a_{15}(\boldsymbol{\sigma}_\gamma\cdot\boldsymbol{k}_\gamma)\boldsymbol{\sigma}_\mathbf{n}\cdot(\boldsymbol{k}_\mathbf{n}\times\boldsymbol{k}_\gamma) + a_{16}(\boldsymbol{\sigma}_\gamma\cdot\boldsymbol{k}_\gamma)\left((\boldsymbol{k}_\mathbf{n}\cdot\boldsymbol{k}_\gamma)^2 - \frac{1}{3}\right)\\
&+ a_{17}(\boldsymbol{\sigma}_\gamma\cdot\boldsymbol{k}_\gamma)(\boldsymbol{k}_\mathbf{n}\cdot\boldsymbol{k}_\gamma)(\boldsymbol{k}_\mathbf{n}\cdot(\boldsymbol{k}_\mathbf{n}\times\boldsymbol{k}_\gamma))\Bigg],
\end{aligned} \tag{2.1}$$

where $\boldsymbol{k}_\mathbf{n}$, $\boldsymbol{k}_\gamma$, $\boldsymbol{\sigma}_\mathbf{n}$, and $\boldsymbol{\sigma}_\gamma$ are unit vectors parallel to the incident neutron momentum, emitted γ-ray momentum, incident neutron spin, and emitted γ-ray spin, respectively. The expressions for the coefficients from a_0 to a_{17} given by the products of the amplitudes from V_1 to V_4 are summarized in Appendix B. The coefficients a_0, a_1, and a_3, which are the unpolarized terms for the neutron and γ-ray, are given by

$$\begin{aligned}
a_0 &= \sum_{J_\mathrm{s}}|V_1(E_\mathrm{n},J_\mathrm{s})|^2 + \sum_{J_\mathrm{p},j}|V_2(E_\mathrm{n},J_\mathrm{p})|^2,\\
a_1 &= 2\,\mathrm{Re}\sum_{J_\mathrm{s},J_\mathrm{p},j} V_1(E_\mathrm{n},J_\mathrm{s})V_2^*(E_\mathrm{n},J_\mathrm{p})P(J_\mathrm{s}J_\mathrm{p}\tfrac{1}{2}j1IF)z_j,\\
a_3 &= 3\sqrt{10}\,\mathrm{Re}\sum_{J_\mathrm{p},j,J'_\mathrm{p},j'} V_2(E_\mathrm{n},J_\mathrm{p})V_2^*(E_\mathrm{n},J'_\mathrm{p})P(J_\mathrm{p}J'_\mathrm{p}jj'2IF)z_jz_{j'}\begin{Bmatrix}2 & 1 & 1\\ 0 & \frac{1}{2} & \frac{1}{2}\\ 2 & j & j'\end{Bmatrix}.
\end{aligned}$$

The factor P is given as

$$\begin{aligned}
P\left(JJ'jj'kIF\right) &= (-1)^{J+J'+j'+I+F}\frac{3}{2}\sqrt{(2J+1)(2J'+1)(2j+1)(2j'+1)}\\
&\times\begin{Bmatrix}k & j & j'\\ I & J' & J\end{Bmatrix}\begin{Bmatrix}k & 1 & 1\\ F & J & J'\end{Bmatrix},
\end{aligned}$$

where J, j, I, and F are the spin of the compound state, total angular momentum of the neutron, spin of the target nuclei, and spin of the final state, respectively. The coefficient z_j, which is the ratio of the partial neutron width to the neutron width of the p-wave resonances, is given by

$$
z_j = \begin{cases} \sqrt{\dfrac{\Gamma^{\mathrm{n}}_{p,j=\frac{1}{2}}}{\Gamma^{\mathrm{n}}_{p}}} & \left(j=\frac{1}{2}\right) \\ \sqrt{\dfrac{\Gamma^{\mathrm{n}}_{p,j=\frac{3}{2}}}{\Gamma^{\mathrm{n}}_{p}}} & \left(j=\frac{3}{2}\right). \end{cases}
$$

Because the width is related to $\Gamma^{\mathrm{n}}_{p,j=1/2} + \Gamma^{\mathrm{n}}_{p,j=3/2} = \Gamma^{\mathrm{n}}_{p}$, z_j can be replaced by the mixing angle ϕ as follows:

$$
z_j = \begin{cases} x = \cos\phi & \left(j=\frac{1}{2}\right) \\ y = \sin\phi & \left(j=\frac{3}{2}\right), \end{cases}
$$

where the relationship in $x^2 + y^2 = 1$ is satisfied.

In the next section, this formula is used to depict the variation of the cross-section of the p-wave resonance with ϕ using ^{115}In as an example, and the procedure to determine the value of ϕ is explained.

2.2 Angular dependence of cross-section of (n, γ) with unpolarized neutrons

By extracting the unpolarized terms for the neutron and γ-ray from Eq. 2.1, the observable differential cross-section can be expressed as

$$
\begin{aligned}
\frac{d\sigma}{d\Omega} &= \tfrac{1}{2}\left(a_0 + a_1 \boldsymbol{k}_{\mathrm{n}} \cdot \boldsymbol{k}_{\gamma} + a_3\left((\boldsymbol{k}_{\mathrm{n}} \cdot \boldsymbol{k}_{\gamma})^2 - \tfrac{1}{3}\right)\right) \\
&= \tfrac{1}{2}\left(a_0 + a_1 \cos\theta_{\gamma} + a_3\left(\cos^2\theta_{\gamma} - \tfrac{1}{3}\right)\right) \qquad (2.2)
\end{aligned}
$$

where θ_γ is the polar angle of the emitted γ-ray direction with respect to the incident neutron momentum. Because the coefficients a_1 and a_3 contain ϕ, they are expressed in terms of the x- and y-components as follows:

$$
a_1 = a_{1x}x + a_{1y}y, \qquad (2.3)
$$

$$
a_3 = a_{3xy}xy + a_{3yy}y^2, \qquad (2.4)
$$

where

$$
\begin{aligned}
a_{1x} &= 2\,\mathrm{Re}\sum_{J_s,J_p} V_1\left(E_{\mathrm{n}}, J_s\right) V_2^*\left(E_{\mathrm{n}}, J_{\mathrm{p}}\right) P\left(J_s J_{\mathrm{p}} \frac{1}{2}\frac{1}{2} 1 I F\right), \\
a_{1y} &= 2\,\mathrm{Re}\sum_{J_s,J_p} V_1\left(E_{\mathrm{n}}, J_s\right) V_2^*\left(E_{\mathrm{n}}, J_{\mathrm{p}}\right) P\left(J_s J_{\mathrm{p}} \frac{1}{2}\frac{3}{2} 1 I F\right), \\
a_{3xy} &= 3\sqrt{10}\,\mathrm{Re}\sum_{J_{\mathrm{p}},J_{\mathrm{p}'}} V_2\left(E_{\mathrm{n}}, J_{\mathrm{p}}\right) V_2^*\left(E_{\mathrm{n}}, J'_{\mathrm{p}}\right) P\left(J_{\mathrm{p}} J'_{\mathrm{p}} \frac{1}{2}\frac{3}{2} 2 I F\right) \begin{Bmatrix} 2 & 1 & 1 \\ 0 & \frac{1}{2} & \frac{1}{2} \\ 2 & \frac{1}{2} & \frac{3}{2} \end{Bmatrix}, \\
a_{3yy} &= 3\sqrt{10}\,\mathrm{Re}\sum_{J_p,J_{p'}} V_2\left(E_{\mathrm{n}}, J_{\mathrm{p}}\right) V_2^*\left(E_{\mathrm{n}}, J'_{\mathrm{p}}\right) P\left(J_{\mathrm{p}} J'_{\mathrm{p}} \frac{3}{2}\frac{3}{2} 2 I F\right) \begin{Bmatrix} 2 & 1 & 1 \\ 0 & \frac{1}{2} & \frac{1}{2} \\ 2 & \frac{3}{2} & \frac{3}{2} \end{Bmatrix}.
\end{aligned}
$$

The coefficient a_{3xx} is zero because the P correlation approaches zero when $j = j' = 1/2$. Thus, ϕ can be obtained by measuring the angular distribution of individual γ-rays from the p-wave resonance, provided that both the spins of the compound state J and final state F are known.

As an example, considering only the 6.85 eV p-wave and 9.07 eV s-wave of the $^{115}\mathrm{In}(\mathrm{n},\gamma)$ reaction, the cross-sections of a_0, a_1, and a_3 as a function of neutron energy are shown in Fig. 2.2. The left side of each figure is shown for a_0, a_{1x}, and a_{1y}, and the right side is shown for a_0, a_{3xy}, and a_{3yy}. The solid line represents a_0, the dotted lines represent a_{1x} (left figure) and a_{3xy} (right figure), and the dashed lines represent a_{1y} (left figure) and a_{3yy} (right figure). Here, Tab. 1.3 is used as the resonance parameter, and the γ width of the p-wave resonance $\Gamma_{\mathrm{p}}^{\gamma}$ is used as the value obtained in Sec. 4.7.3. The transition ratios $B_{\mathrm{r},f}$ are assumed to be 1 for all resonances; in practice, the relative transition ratio between the s-wave and p-wave resonances must be obtained from an experiment and substituted. The transition ratios for each resonance are obtained in Sec. 4.8. The top, middle, and bottom panels in Fig. 2.2 correspond to $F = 4$, $F = 5$, and $F = 6$, respectively. Figures are not available for $F = 3$ or less, or for $F = 7$ or more, because the P correlation becomes zero when the F value changes by more than 2 with respect to the J value of the p-wave resonance. As these figures show, the a_1 term has the form of an odd function and the a_3 term has the form of an even function.

The observable differential cross-section in this study depends on both the polar angle θ_γ and mixing angle ϕ. Figure 2.3 shows ϕ and θ_γ dependencies of the differential cross-section around the p-wave resonance for $F = 4$ (top figure), $F = 5$ (middle figure) and $F = 6$ (bottom figure), respectively. The solid, dotted, and dashed lines show the curves for the different values of ϕ (left figure) and θ_γ (right figure). Because the shape of the p-wave resonance differs depending on ϕ and θ_γ, the ϕ value can be determined by measuring the cross-section of the p-wave resonance for each θ_γ.

To determine the ϕ value, we define the asymmetry of the peak shape of the p-wave resonance as

$$A_{\mathrm{LH}} \equiv \frac{I_{\mathrm{L}} - I_{\mathrm{H}}}{I_{\mathrm{L}} + I_{\mathrm{H}}}, \tag{2.5}$$

where I_{L} and I_{H} are the integrated values in the lower and higher regions from the resonance energy, respectively. They are defined as

$$\begin{aligned}
I_{\mathrm{L}} &\equiv \int_{\mathrm{L}} dE_{\mathrm{n}} \frac{d\sigma}{d\Omega} \\
&= \frac{1}{2}\int_{\mathrm{L}} dE_{\mathrm{n}} \left(a_0 + a_1 \cos\theta_\gamma + a_3\left(\cos^2\theta_\gamma - \frac{1}{3}\right)\right) \\
&= I_{\mathrm{L},a_0} + I_{\mathrm{L},a_1}\cos\theta_\gamma + I_{\mathrm{L},a_3}\left(\cos^2\theta_\gamma - \frac{1}{3}\right), \\
I_{\mathrm{H}} &\equiv \int_{\mathrm{H}} dE_{\mathrm{n}} \frac{d\sigma}{d\Omega} \\
&= \frac{1}{2}\int_{\mathrm{H}} dE_{\mathrm{n}} \left(a_0 + a_1 \cos\theta_\gamma + a_3\left(\cos^2\theta_\gamma - \frac{1}{3}\right)\right) \\
&= I_{\mathrm{H},a_0} + I_{\mathrm{H},a_1}\cos\theta_\gamma + I_{\mathrm{H},a_3}\left(\cos^2\theta_\gamma - \frac{1}{3}\right),
\end{aligned}$$

where

$$\begin{aligned} I_{\mathrm{L},a_i} &= \frac{1}{2}\int_{\mathrm{L}} a_i dE_{\mathrm{n}}, \\ I_{\mathrm{H},a_i} &= \frac{1}{2}\int_{\mathrm{H}} a_i dE_{\mathrm{n}}. \end{aligned}$$

By substituting I_{L} and I_{H} into Eq. 2.5, the asymmetry is expressed as follows:

$$\begin{aligned} A_{\mathrm{LH}} &= \frac{(I_{\mathrm{L},a_0} - I_{\mathrm{H},a_0}) + (I_{\mathrm{L},a_1} - I_{\mathrm{H},a_1})\cos\theta_\gamma + (I_{\mathrm{L},a_3} - I_{\mathrm{H},a_3})\left(\cos^2\theta_\gamma - \frac{1}{3}\right)}{(I_{\mathrm{L},a_0} + I_{\mathrm{H},a_0}) + (I_{\mathrm{L},a_1} + I_{\mathrm{H},a_1})\cos\theta_\gamma + (I_{\mathrm{L},a_3} + I_{\mathrm{H},a_3})\left(\cos^2\theta_\gamma - \frac{1}{3}\right)} \\ &\sim \frac{(I_{\mathrm{L},a_0} - I_{\mathrm{H},a_0}) + (I_{\mathrm{L},a_1} - I_{\mathrm{H},a_1})\cos\theta_\gamma}{(I_{\mathrm{L},a_0} + I_{\mathrm{H},a_0}) + (I_{\mathrm{L},a_3} + I_{\mathrm{H},a_3})\left(\cos^2\theta_\gamma - \frac{1}{3}\right)} \\ &= \frac{\frac{\left(I_{\mathrm{L},a_0} - I_{\mathrm{H},a_0}\right)}{\left(I_{\mathrm{L},a_0} + I_{\mathrm{H},a_0}\right)} + \frac{\left(I_{\mathrm{L},a_1} - I_{\mathrm{H},a_1}\right)}{\left(I_{\mathrm{L},a_0} + I_{\mathrm{H},a_0}\right)}\cos\theta_\gamma}{1 + \frac{\left(I_{\mathrm{L},a_3} + I_{\mathrm{H},a_3}\right)}{\left(I_{\mathrm{L},a_0} + I_{\mathrm{H},a_0}\right)}\left(\cos^2\theta_\gamma - \frac{1}{3}\right)} \\ &= \frac{A_0 + A_1\cos\theta_\gamma}{1 + A_3\left(\cos^2\theta_\gamma - \frac{1}{3}\right)}. \end{aligned} \tag{2.6}$$

where

$$\begin{aligned} A_0 &= \frac{I_{\mathrm{L},a_0} - I_{\mathrm{H},a_0}}{I_{\mathrm{L},a_0} + I_{\mathrm{H},a_0}}, \\ A_1 &= \frac{I_{\mathrm{L},a_1} - I_{\mathrm{H},a_1}}{I_{\mathrm{L},a_0} + I_{\mathrm{H},a_0}}, \\ A_3 &= \frac{I_{\mathrm{L},a_3} + I_{\mathrm{H},a_3}}{I_{\mathrm{L},a_0} + I_{\mathrm{H},a_0}}. \end{aligned}$$

The approximation in the second line of Eq. 2.6 utilizes the property of a_1 and a_3 being odd and even functions, respectively. The value of ϕ can be determined by fitting the angular dependence of A_{LH} obtained from the experimental results using Eq. 2.6 and comparing the theoretical calculation with A_1 and A_3.

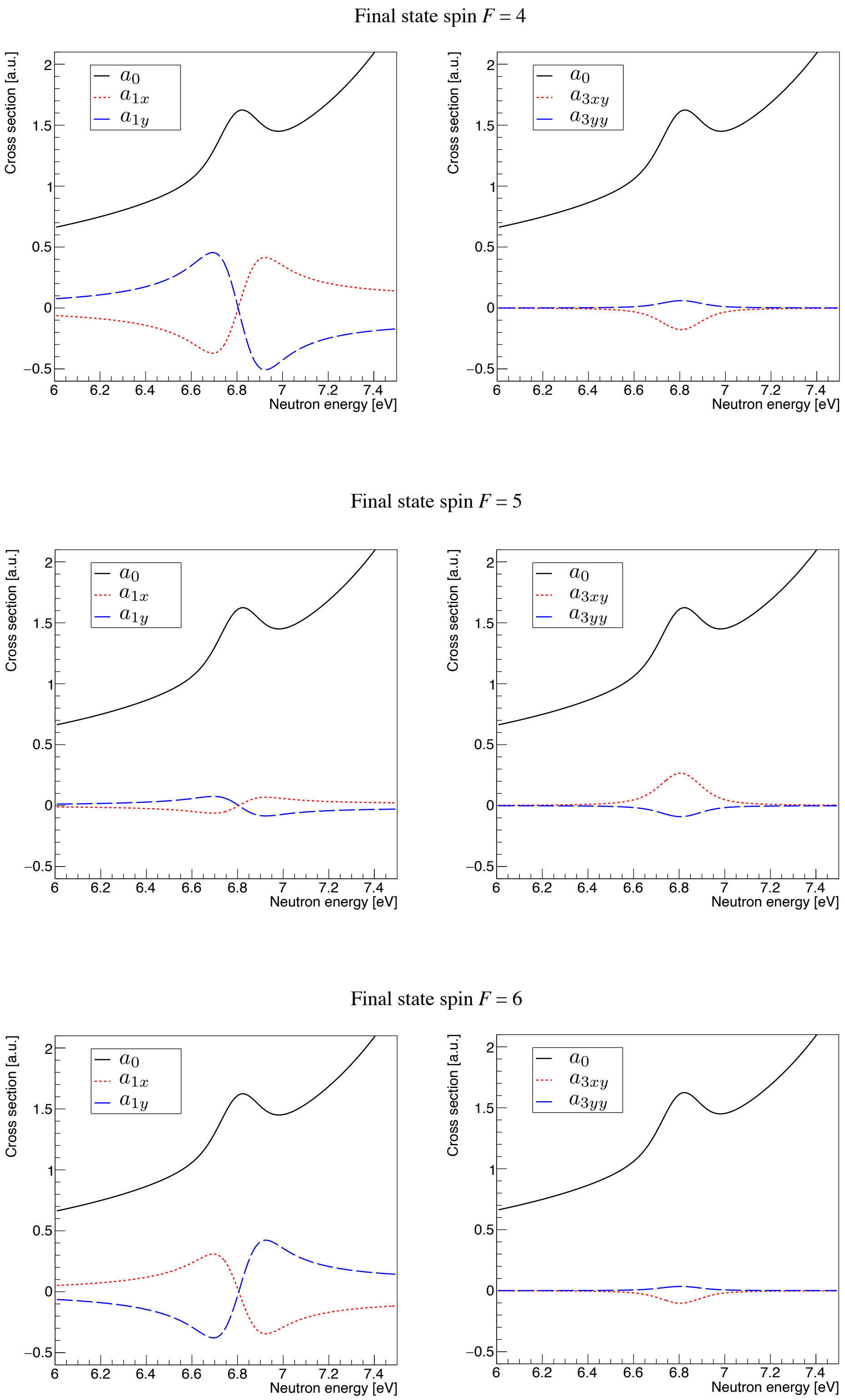

FIGURE 2.2: Coefficients a_0, a_{1x}, a_{1y}, a_{3xy}, and a_{3yy} in the ^{115}In(n,γ) reaction to the $F = 4$ final state, using the resonance parameters listed in Tab. 1.3. The top, middle, and bottom figures are for $F = 4$, $F = 5$, and $F = 6$, respectively. The solid line is a_0, the dotted lines are a_{1x} (left figure) and a_{3xy} (right figure), and the dashed lines are a_{1y} (left figure) and a_{3yy} (right figure).

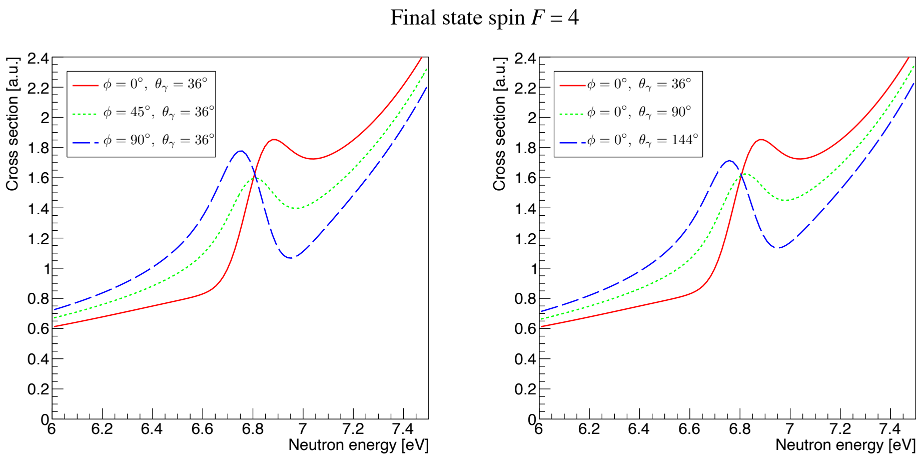
Final state spin $F = 4$

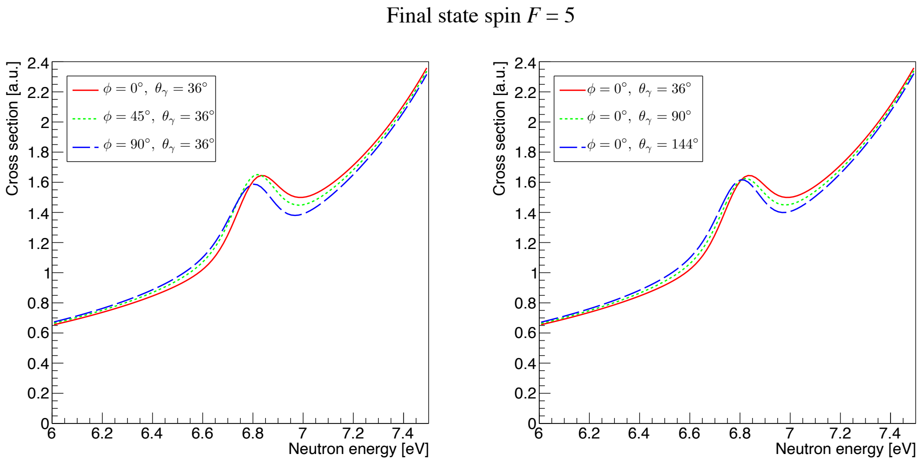
Final state spin $F = 5$

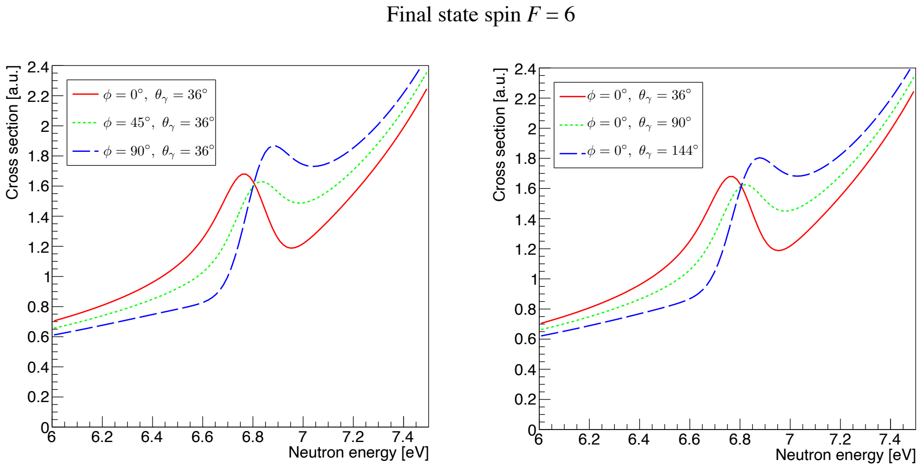
Final state spin $F = 6$

FIGURE 2.3: Variables ϕ and θ_γ dependencies of the p-wave resonance. The top, middle, and bottom figures are for $F = 4$, $F = 5$, and $F = 6$, respectively. The solid, dotted, and dashed lines show the curves for the different values of ϕ (left figure) and θ_γ (right figure).

Chapter 3

Measurement of γ ray from $\mathrm{In(n,\gamma)}$

Chap. 2 explains that the ϕ value can be obtained by comparing the θ_γ dependence of the peak shape of the p-wave resonance between the experimental results and theoretical calculations. In this chapter, an experimental facility and instruments suitable for this measurement are described.

3.1 Experimental facility and setup

3.1.1 J-PARC MLF

The Japan Proton Accelerator Research Complex (J-PARC) is a high-intensity proton accelerator facility in Tokai village, Ibaraki Prefecture. Various secondary particle beams, such as neutrons, muons, K mesons, and neutrinos, produced by the world's most intense proton beams are available. Figure 3.1 shows a bird's eye view of J-PARC. In the linear accelerator (LINAC), hydrogen gas is used to produce negative hydrogen ions, and a 400 MeV pulsed proton beam is produced using a radio-frequency electric field. The pulsed proton beam is then transported to the Rapid-Cycling Synchrotron (RCS), where it is accelerated to 3 GeV. Most of the pulsed proton beam is injected into the Materials and Life Science Facility (MLF), while the remainder is directed to the Main Ring (MR). The pulsed proton beam from the RCS has a width of 100 ns with an interval of 600 ns (double bunch) and a repetition rate of 25 Hz. In the experiments in this study, the average power of the pulsed proton beam was 710 kW.

The MLF is an experimental facility that uses powerful pulsed neutron beams. The pulsed proton beam accelerated to 3 GeV by the RCS is injected into the liquid mercury target of the MLF, where the nuclear separation reactions produce neutrons. The high-energy neutrons generated from the mercury target are moderated by a light water moderator and a liquid-hydrogen moderator at 20 K and 1.5 MPa, respectively, and are directed to the 23 neutron beam ports of the MLF. The MLF has three types of moderators: a coupled moderator, decoupled moderator, and poison moderator. The characteristics of each moderator are summarized in Tab. 3.1. There is a trade-off between neutron energy resolution and neutron flux between these moderators. The Accurate Neutron-Nucleus Reaction Measurement Instrument (ANNRI), the beamline where this study was performed, falls into the category of coupled moderators, which are moderators with the highest neutron flux. Sec. 3.1.2 and 3.1.3 describe the configurations of the beamline and detectors of the ANNRI.

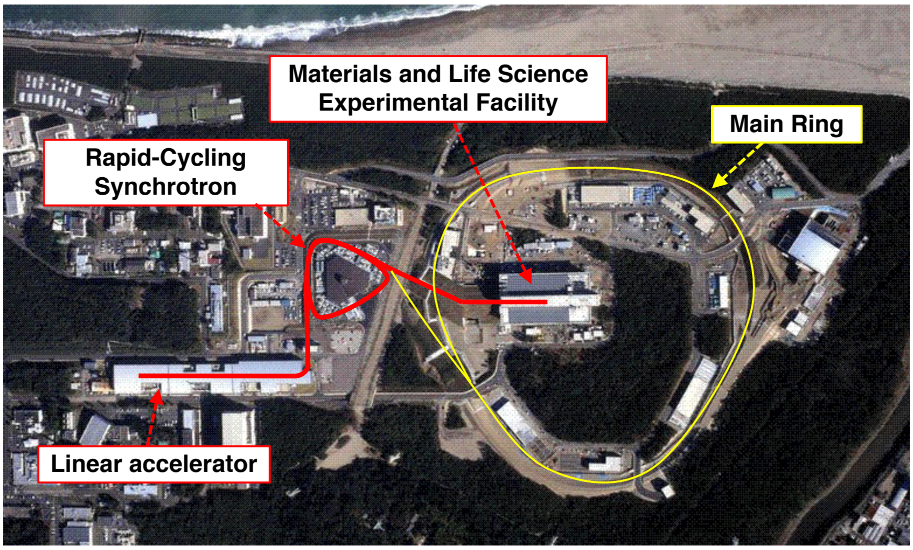

FIGURE 3.1: Bird's eye view of J-PARC [61].

TABLE 3.1: Characteristics of moderators in the MLF [62].

Type of Moderator	Number of beam port	Time-integrated thermal neutron flux $[\mathrm{n/s \cdot cm^2}]$	Peak neutron flux at 10 meV $[\mathrm{n/eV \cdot s \cdot cm^2}]$	Pulsed width in FWHM at 10 meV $[\mu s]$
Coupled	11	4.6×10^8	6.0×10^{12}	92
Decoupled	6	0.95×10^8	3.0×10^{12}	33
Poisoned (Thicker side)	3	0.65×10^8	2.4×10^{12}	22
Poisoned (Thinner side)	3	0.38×10^8	1.4×10^{12}	12

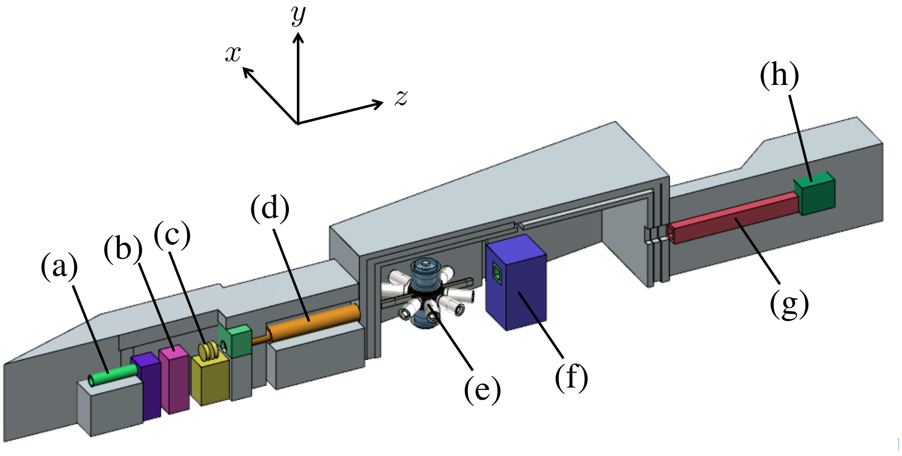

FIGURE 3.2: Schematic illustration of the ANNRI installed at the beamline BL04 of the MLF at J-PARC. (a) Collimator, (b) neutron filter, (c) disk chopper, (d) collimator, (e) detector configuration, (f) collimator, (g) boron resin, and (h) beam stopper (iron) [63].

3.1.2 BL04 ANNRI

An illustration of the experimental setup of the ANNRI, which is beamline 04 (BL04) of the MLF, is shown in Fig. 3.2. The beam axis is represented by the z-axis, the vertical direction is the y-axis, and the x-axis is defined such that it forms a right-handed coordinate system. The origin of the coordinate system is the position of the nuclear target. The pulsed neutron beam is transported through a collimator (Fig. 3.2(a)), neutron filters (Fig. 3.2(b)), a disk chopper (Fig. 3.2(c)), and a collimator (Fig. 3.2(d)) to the target position located 21.5 m from the moderator surface. The neutrons are absorbed by the target and emit γ-rays, which are detected by the detectors. The configuration of the detector in the ANNRI (Fig. 3.2(e)) is explained in Sec. 3.1.3. The neutrons transmitted to the target pass through a collimator (Fig. 3.2(f)) and a boron resin (Fig. 3.2(g)), and they are finally dumped by a beam stopper ((h) in Fig. 3.2).

The collimators consist of an upstream collimator (Fig. 3.2(a)) and downstream collimator (Fig. 3.2(d)), which are used to adjust the intensity and size of the neutron beam. The upstream collimator is available in three hole sizes: open (no collimator), 27 mm square, and 15 mm square. The downstream collimator is available in four holes with diameter sizes of 6 mm, 7 mm, 15 mm, and 22 mm. A disk chopper (Fig. 3.2(c)) was installed at 17 m to eliminate cold neutrons. The disk chopper is a half-disk with its surface coated with 95 wt% isotopically enriched boron carbide. The disk chopper is operated synchronously with the proton beam injection to suppress slow neutrons (below 3 meV) to avoid frame overlap. Several neutron filters (Fig. 3.2(b)) were also inserted between the upstream collimator and disk chopper to adjust the beam intensity in the energy region of interest. There are six lead (Pb) filters, one with a thickness of 12.5 mm and another with a thickness of 25 mm, and four with a thickness of 50 mm, which can be combined. The neutron filter material can be selected from manganese (Mn), cobalt (Co), aluminum (Al), silver (Ag), indium (In), lead (Pb), and cadmium (Cd).

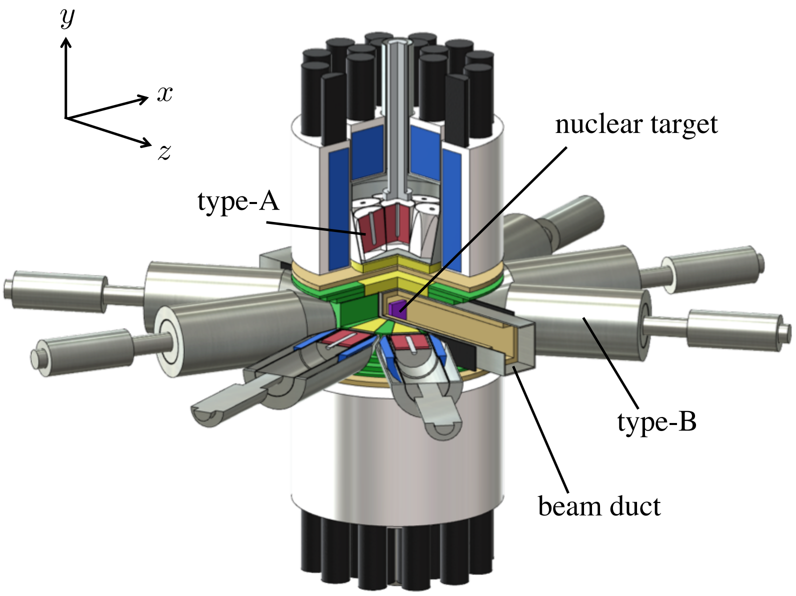

FIGURE 3.3: Configuration of the germanium detectors [63].

3.1.3 Detector configuration in the ANNRI

Germanium detectors are used at the ANNRI to measure the energy of the γ-rays emitted from the (n, γ) reaction with high-energy resolution. Figure 3.3 shows the germanium detectors and the surrounding material for the neutron shield. The top figure in Fig. 3.3 defines θ and the bottom figure defines φ in the polar coordinate system. The ANNRI has two types of germanium detectors: type-A and type-B. The shapes and sizes of type-A and type-B crystals are shown in Fig 3.4. The front end of the type-A crystal is hexagonal, and the back end has a hole for inserting the electrode. Owing to their hexagonal shape, type-A crystals can be installed closely together. The type-A clusters are placed directly above and below the target. The front end of the type-B crystal is circular and the back end has a hole for inserting an electrode. Type-B crystals are placed in the xz-plane, with the cylindrical base facing the target.

Seven type-A crystals form a detector unit (Fig. 3.5). Type-A germanium detectors are covered by two neutron shields (Fig. 3.5(f) and (h)) composed of lithium hydride (LiH) with thicknesses of 22.3 mm and 17.3 mm. The neutron shield (Fig. 3.5(g)) is composed of lithium fluoride (LiF) with a thickness of 5 mm. The central crystal is directed toward the center of the target, whereas the surrounding six detectors are directed farther away from the center. Therefore, they have different solid angles of $0.010 \times 4\pi$ sr (central) and $0.0091 \times 4\pi$ sr (one of the six surrounding detectors), respectively. The side and back of the assembly of type-A detectors are surrounded by bismuth germanate (BGO) scintillation detectors (Fig. 3.5(d)). However, they were not used in our study because the time information was not synchronized with the germanium detectors. Two clusters of type-A crystals are placed at $(\theta, \varphi) = (90°, 90°)$ and $(90°, 270°)$. The number of detectors and their positions are summarized in Fig. 3.6 and Tab. 3.2. The central crystal of the upper (lower) type-A crystal is denoted by d1 (d8), and the other six surrounding detectors are denoted by d2 to d7 (d9 to d14).

Eight type-B crystals are assembled as shown in Fig. 3.7. These detectors are

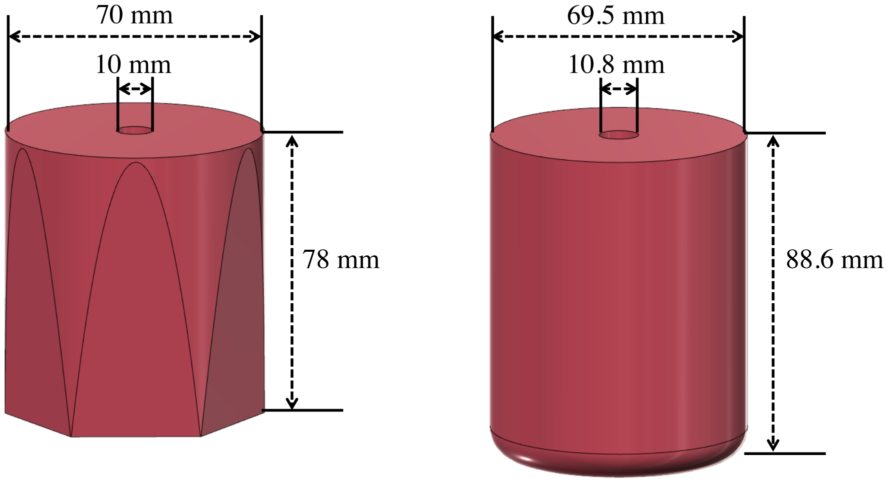

FIGURE 3.4: Schematics of type-A (left) and type-B (right) germanium crystals [63].

TABLE 3.2: Values of θ and φ at the center of the front-end of each detector.

Detector ID	θ [°]	φ [°]
d1	90.0	90.0
d2	90.0	66.3
d3	70.9	78.2
d4	70.9	101.8
d5	90.0	113.7
d6	109.1	101.8
d7	109.1	78.2
d8	90.0	270.0
d9	90.0	293.7
d10	70.9	281.8
d11	70.9	258.2
d12	90.0	246.3
d13	109.1	258.2
d14	109.1	281.8
d15	144.0	180.0
d16	108.0	180.0
d17	72.0	180.0
d18	36.0	180.0
d19	36.0	0.0
d20	72.0	0.0
d21	108.0	0.0
d22	144.0	0.0

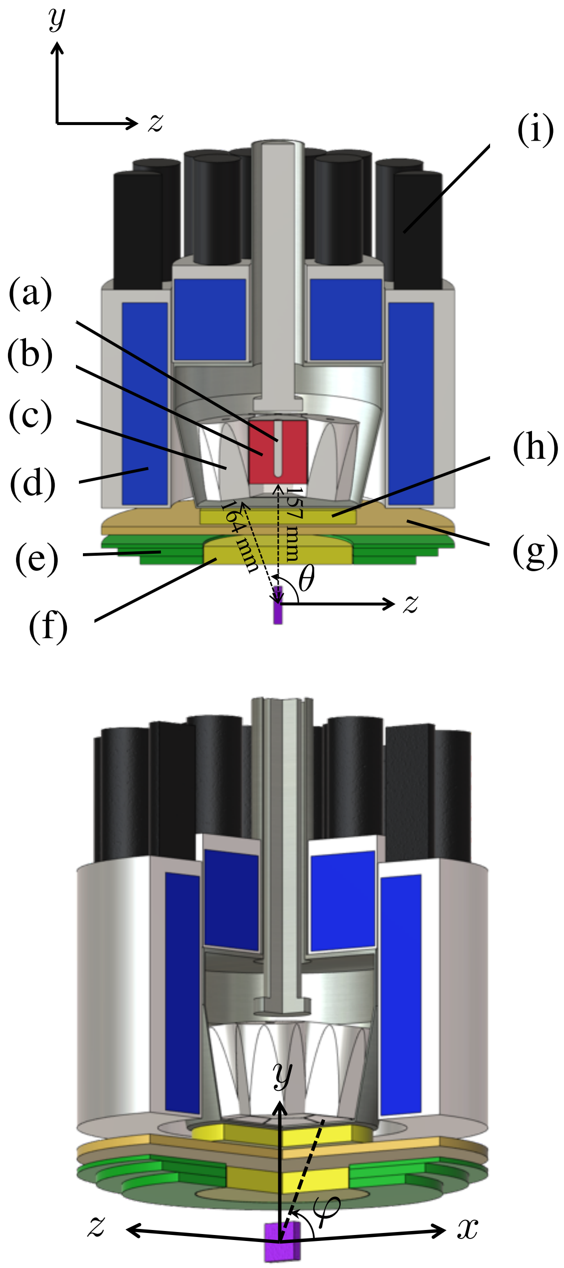

FIGURE 3.5: Schematic of a unit of type-A crystals consisting of seven type-A germanium detectors. Top figure: (a) electrode, (b) germanium crystal, (c) aluminum case, (d) BGO crystal, (e) γ-ray shield (Pb collimator), (f) neutron shield-1 (22.3 mm LiH), (g) neutron shield-2 (5 mm LiF), (h) neutron shield-3 (17.3 mm LiH), and (i) photomultiplier tube for the BGO crystal. The bottom figure shows the definition of the φ angle [63].

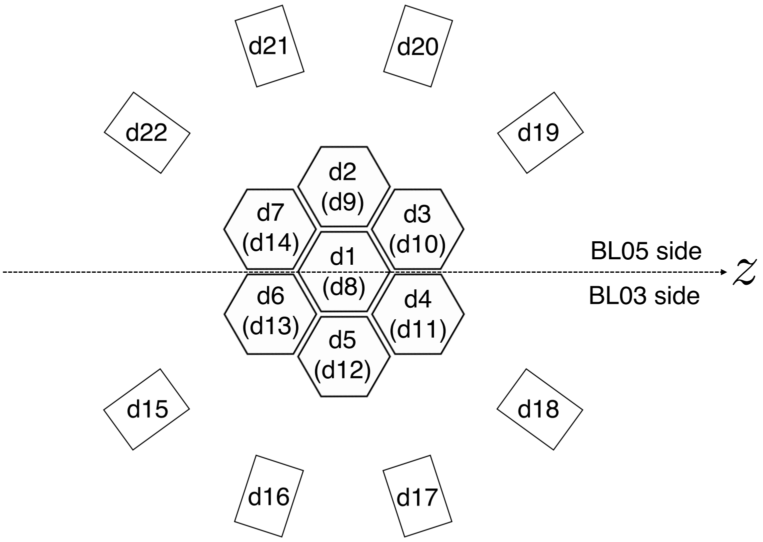

FIGURE 3.6: Schematic of positions of germanium detectors.

numbered from d15 to d22, and they are summarized in Fig. 3.6 and Tab. 3.2. Note that the germanium crystal of detector d16 is smaller than that of the other detectors. All type-B crystals are towards the center of the target. Therefore, except for detector d16, they all have the same solid angle of $0.0072 \times 4\pi$ sr. The solid angle of detector d16 is $0.0048 \times 4\pi$ sr.

A conical-shaped γ-ray collimator created from lead is placed between the type-B crystal and the nuclear target. The diameter of the collimator at the front end of the type-B crystal is 60 mm. The inside of the collimator is filled with LiF powder, which was encapsulated in an aluminum case, to absorb the scattered neutrons.

The beam duct consists of two layers. The outer layer is fabricated aluminum with a thickness of 3 mm. The cross-sectional dimension is 86 mm × 96 mm. The inner layer is fabricated from LiF with a thickness of 10.5 mm to absorb scattered neutrons.

3.2 Neutron energy resolution

The neutron energy resolution of the pulsed neutron beam is explained by the time structure caused by two factors: the pulse structure of the incident proton beam and neutron moderation process in the MLF moderator. Several functions have been proposed to describe the time structure of pulsed neutron beams. Some of the representative functions are the Ikeda–Carpenter function [64], Cole–Windsor function [65], Ganzing function [66], and Gaussian function [67, 68]. The pulse structure of the neutron beam at BL04 has already been studied by K. Kino *et al.* [69] and is known to be described by the Ikeda–Carpenter function. The Ikeda–Carpenter function ψ is described by the following equation using the neutron energy E_n and neutron arrival time t with the origin at the injection of the pulsed proton beam into the MLF:

$$\begin{aligned}\psi\left(E_\mathrm{n}, t\right) = \tfrac{\alpha C}{2} \Big\{ & (1-R)(\alpha t)^2 e^{-\alpha t} + 2R\tfrac{\alpha^2\beta}{(\alpha-\beta)^3} \\ & \times \left[e^{-\beta t} - e^{-\alpha t}\left(1 + (\alpha-\beta)t + \tfrac{1}{2}(\alpha-\beta)^2 t^2\right)\right]\Big\} \end{aligned} \tag{3.1}$$

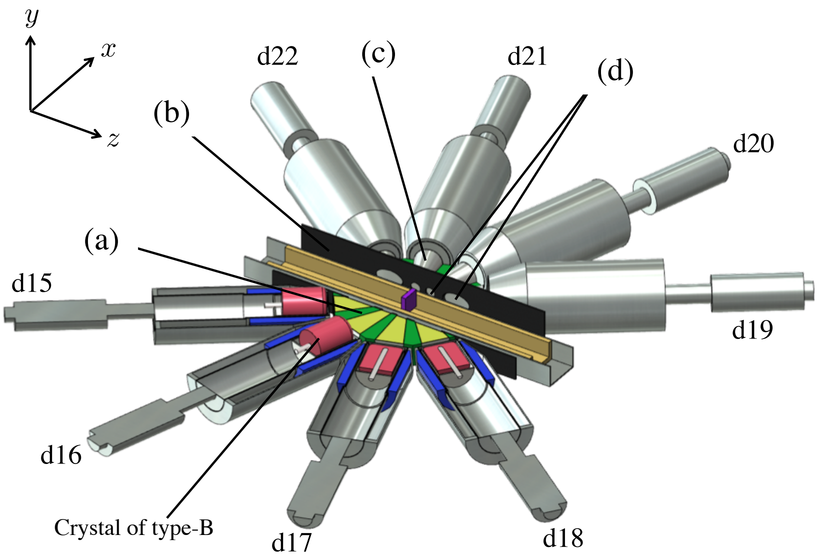

FIGURE 3.7: Schematic of the assembly of type-B crystals. (a) Pb collimator, (b) carbon board, (c) LiH powder, and (d) collimator holes [63].

where the parameters α, β, and R depend on E_n, and C is an E_n-independent scaling factor for normalization. Equation 3.1 is composed of two physical terms: the slowing-down and storage terms. These are $1-R$ and R in the ratio ($0 \leq R \leq 1$) of the total neutron intensity. The time was modified to $t - t_0$, where t_0 is the time of flight (TOF) of neutrons after emission from the moderator. The value of $t - t_0$ indicates the moderation and storage time inside the moderator. Each parameter of the Ikeda–Carpenter function was obtained using a Monte Carlo simulation that implemented the MLF moderator geometry. Figure 3.8 shows examples of the time structure of the neutron beam obtained from the simulation and the results of the fitting using Eq. 3.1. The solid lines represent Eq. 3.1. The dashed and dotted lines correspond to the slowing-down and storage terms, respectively, in Eq. 3.1. The higher the neutron energy, the wider the time structure. Figure 3.9 shows the results of fitting the neutron energy dependence of t_0, α, β, and R with a polynomial function. Convolving these parameters into the calculations in Chap. 2 facilitates a more accurate comparison of the theoretical calculations and experimental data. They are used in Sec. 4.7 and 4.8.

The time structure of the neutron beam has been experimentally demonstrated in the neutron energy of the thermal and epithermal regions. Figure 3.10 shows a comparison of the neutron energy dependence of the full width half maximum (FWHM) of the time structure of a single bunch mode between simulation (the solid line in Fig. 3.10) and measurement (the points in Fig. 3.10). The results for the neutron energy of the thermal region were obtained from the measurement of the Bragg peak using a mica sample (the points of in Fig. 3.10(a)), and in the neutron energy of the epithermal region were obtained from the measurement of the well-known resonance peak in the neutron capture reaction of ^{181}Ta (the points in Fig. 3.10(b)). The simulations reproduced the measurement results.

J-PARC has two types of proton beam operation modes. One is a single-bunch mode, in which the pulsed protons consist of bunches with a width of approximately 100 ns. The other is a double-bunch mode, in which the time interval between the two proton bunches is approximately 600 ns. Figure 3.11 shows the energy resolution of

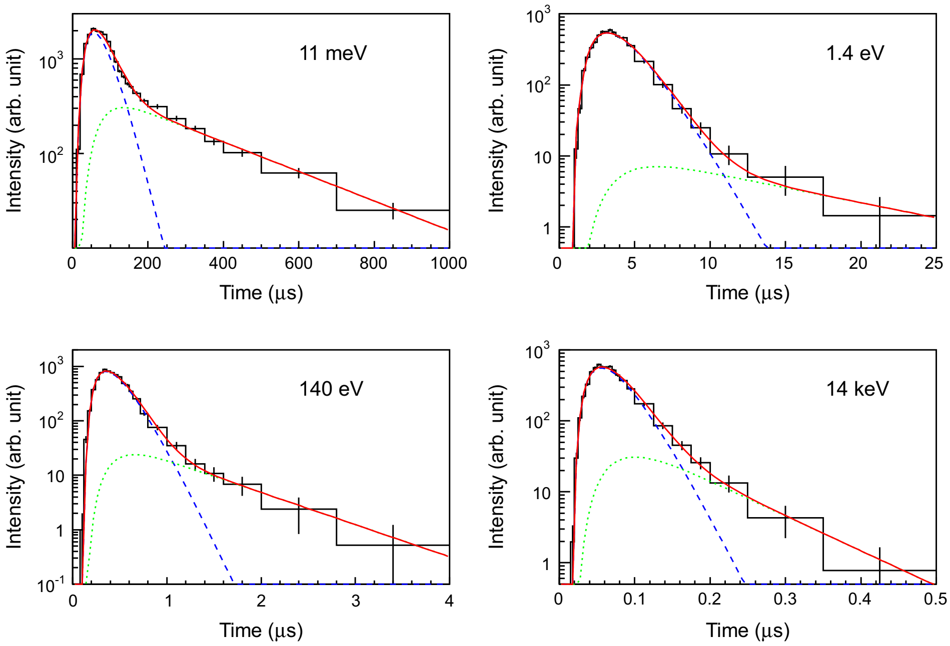

FIGURE 3.8: Examples of fits of Eq. 3.1 to the in structures of the neutron pulses obtained in the simulation [69]. The solid lines represent Eq. 3.1. The dashed and dotted lines correspond to the slowing-down and storage terms in Eq. 3.1, respectively.

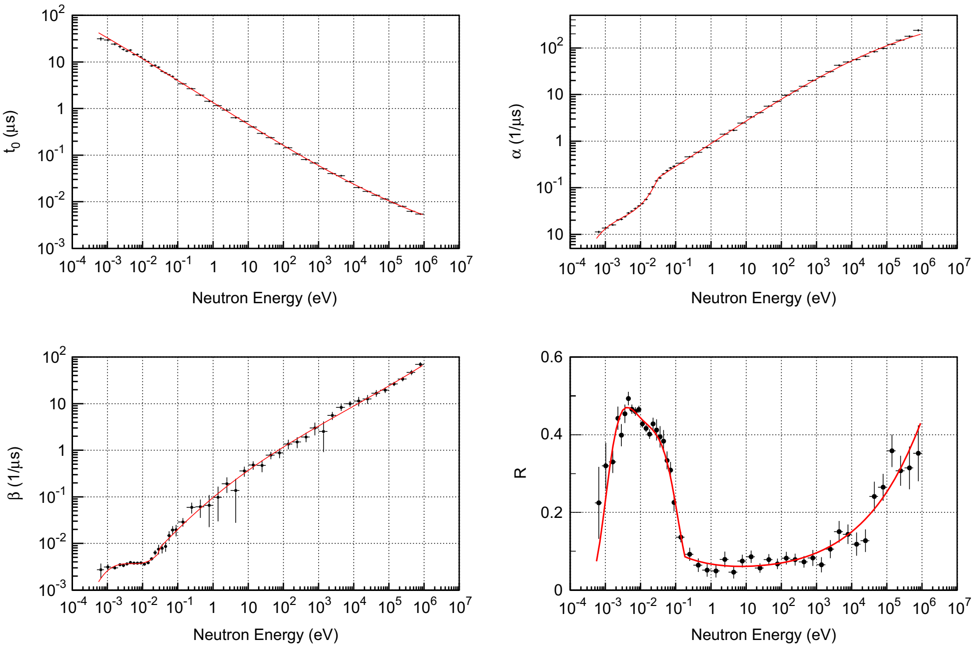

FIGURE 3.9: Fit parameters t_0, α, β, and R [69]. The solid lines are polynomial functions fitted to the data points.

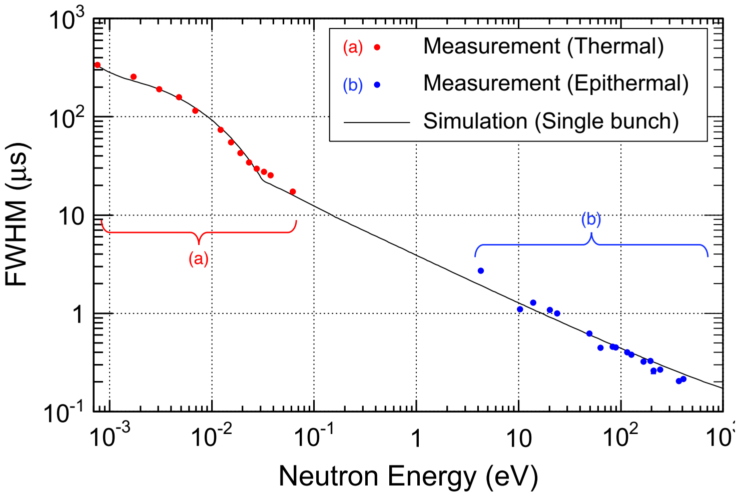

Figure 3.10: Comparison of the simulation and measurements of the FWHM values of the time structures of neutron pulses for single bunch mode [69].

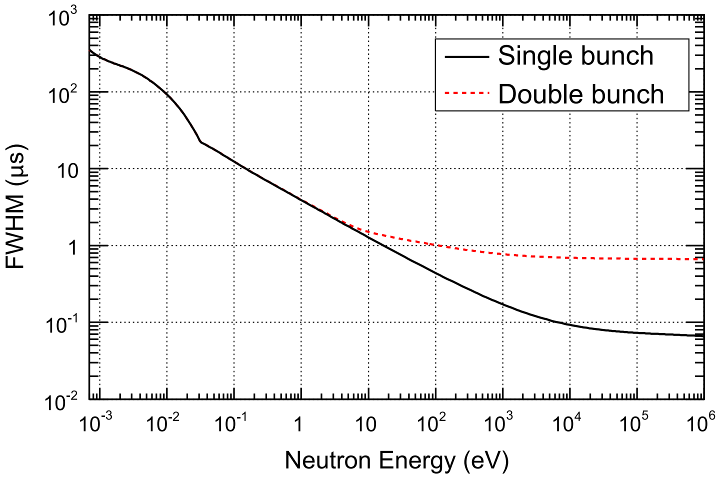

Figure 3.11: FWHM values for the time structure using the simulation as a function of neutron energy. The solid and dashed lines represent single- and double-bunch modes, respectively [69].

the neutron beam in both modes, with the horizontal and vertical axes representing the neutron energy and FWHM, respectively. The solid and dotted lines represent the single and double-bunch modes, respectively. The effect of the double bunch is observed above ~ 5 eV as a function of the neutron energy. In this study, J-PARC was operated in the double-bunch mode. Therefore, the values of the parameters t_0, α, β, and R in the theoretical calculations were used for the double-bunch mode.

3.3 Data acquisition system

The signals generated by the incident γ-rays on germanium are collected using a data acquisition system (DAQ) (Fig. 3.12). The output signal from each germanium detector is amplified using a preamplifier and then processed using four CAEN V1724 modules. Details of the operation of each part of this module and the signal-processing flow are described in Ref. [70]. This section describes the acquisition of the time and γ-ray energy information of the signal associated with the injection of γ-rays into the germanium detector. In this experiment, four V1724 modules were used to process the signals from 22 detectors. These four modules operate in synchronization with proton beam injection and are controlled by the DAQ PC. The signal input to a CAEN V1724 module is divided into two branches: one for timing and triggering, and the other for pulse height. The former is converted into a bipolar signal that acts as a trigger when the amplitude of the bipolar signal exceeds a threshold value. This signal is processed by the upper branch (Fig. 3.12). The threshold is set to approximately 100 keV. The timing information of the trigger is measured using an internal clock with a frequency of 10 ns. The internal clock is reset after each proton beam injection. Because the flight time of γ-rays is negligible compared with that of neutrons, the trigger timing information is almost synonymous with the TOF. The timing information can be measured in 64 bits; therefore, it will not overflow even if the accelerator is stopped for a long time. The pulse-height signal is converted into a trapezoidal signal, and the average trapezoidal height in the flat top region is recorded as the pulse height. This signal is processed by the lower branch (Fig. 3.12). The pulse height can be measured up to 15 bits, i.e., 16384 ADC ch. Because the γ-rays emitted by the (n, γ) reaction have a maximum energy of approximately 10 MeV, attenuators are used to maintain it within the dynamic range of the pulse height. By using the attenuators, one analog-to-digital converter (ADC) channel is adjusted to approximately 1 keV.

Figure 3.13 shows a simplified signal scheme of the four patterns for processing the time information (TT filter, trigger, and peaking) and energy information (input and trapezoid). If the time interval between two signals is small at a high counting rate, the flat top regions will overlap, and determining the pulse height will not be possible. The CAEN V1724 module processes signals in four patterns depending on the time interval between the two signals, as shown in the figure. Here, the pulse height of the i-th signal is E_i, the time information is T_i, and the time interval at the boundary of each pattern is t_0, t_1, and t_2, respectively.

- Pattern 1 ($T_{i+1} - T_i > t_0$)
  This pattern corresponds to the top left of Fig. 3.13. The time interval between the two signals is sufficiently large that the trapezoidal signals do not overlap. The pulse heights E_i and E_{i+1} and the time information T_i and T_{i+1} can be recorded correctly.

- Pattern 2 ($t_1 < T_{i+1} - T_i < t_0$)
  This pattern corresponds to the top right of Fig. 3.13. The first pulse height E_i

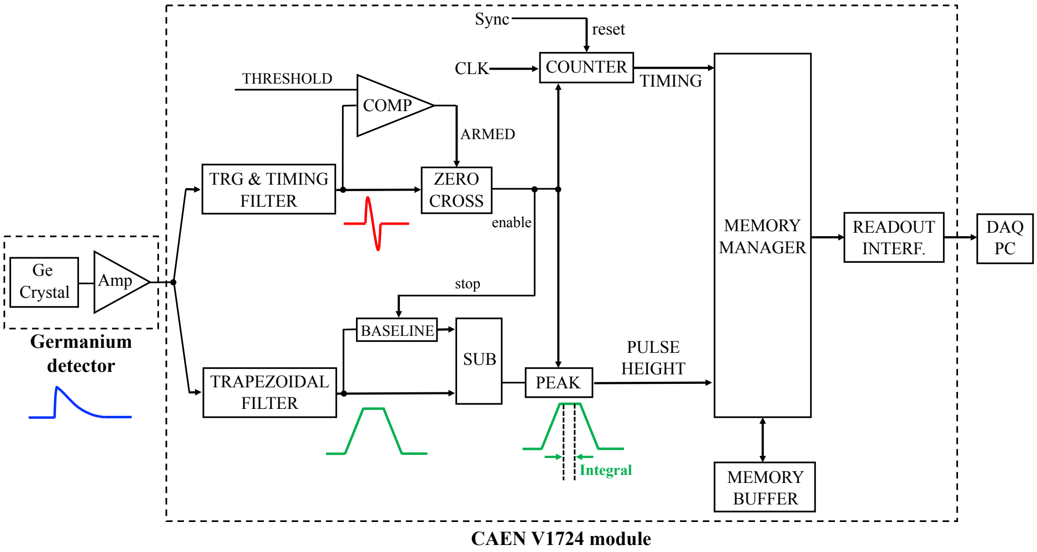

FIGURE 3.12: Block diagram of V1724 module [70]. A signal from the germanium detector is divided into two branches: one for timing and triggering and the other for the pulse height.

can be recorded correctly, but the second pulse height E_{i+1} cannot be recorded correctly because the flat top region of the second trapezoid is not flat. Here, E_{i+1} is recorded as zero. In contrast, T_i and T_{i+1} can be recorded correctly.

- Pattern 3 ($t_2 < T_{i+1} - T_i < t_1$)
  This pattern corresponds to the bottom left of Fig. 3.13. Because the two trapezoidal plane regions overlap, the pulse heights E_i and E_{i+1} are both recorded as zero. In addition, because the timing of the trigger can be determined, time information can be recorded correctly.

- Pattern 4 ($T_{i+1} - T_i < t_2$)
  This pattern corresponds to the bottom right of Fig. 3.13. Two input pulses overlap, and the two signals are considered as one. The pulse height E_i is recorded as the sum of the heights of the two pulses, and the time information T_i is recorded as the trigger timing of the first signal.

The values of t_0, t_1, and t_2 were 3.54 μs, 2.38 μs, and 0.52 μs, respectively. These values were observed to be independent of the pulse height. CAEN V1724 transfers the accumulated data to the computer when the local buffer has accumulated data for 1024 events. If the speed of accumulating data in the local buffer exceeds the speed of writing records to the computer (approximately 300 kcount/s), the CAEN V1724 module will stop. Because the time information is recorded in the data for the events in patterns 2 and 3, the number of lost events can be estimated and restored based on the energy information of each event. This recovery method is described in Sec. 4.4. The events in pattern 4 are impossible to restore because both time and energy information are lost. Therefore, the experiment must be performed under conditions with sufficiently few events in pattern 4.

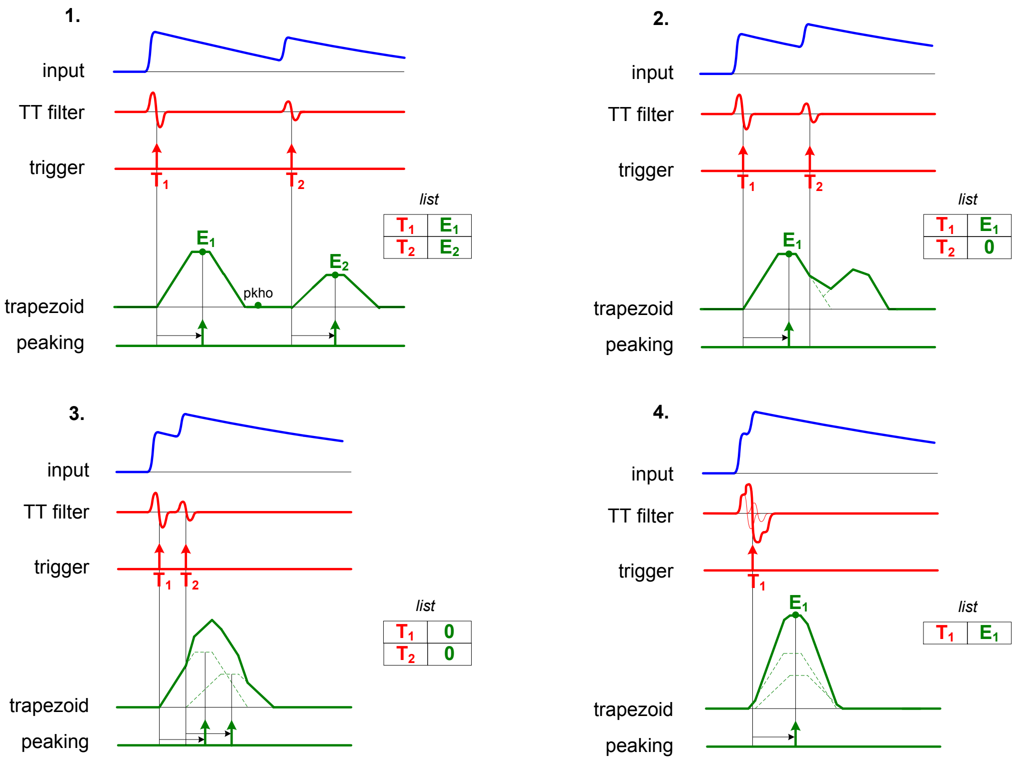

FIGURE 3.13: The effect of trapezoid overlapping in the four main scenarios: 1. The two trapezoids are well separated (top left). 2. The second trapezoid begins at the falling edge of the first trapezoid (top right). 3. The second trapezoid begins at the rising edge of the first trapezoid (bottom left). 4. The two input pulses accumulate in the input rise time (bottom right) [70].

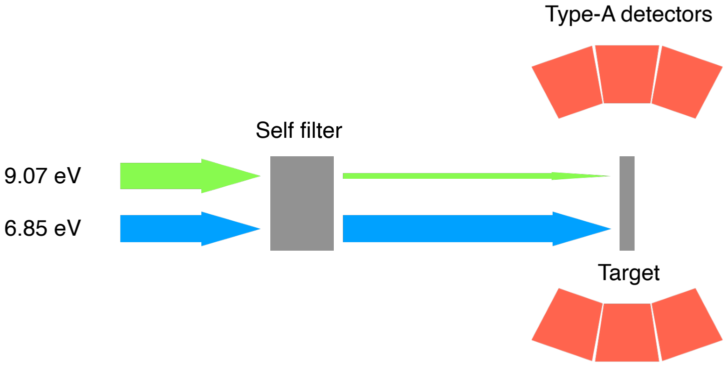

FIGURE 3.14: Schematic of the self-filtering method.

3.4 Measurement conditions and collected data

3.4.1 Measurement conditions

As mentioned in Chap. 1, s-wave resonances with large cross-sections exist near the p-wave resonance in the ^{115}In(n, γ) reaction. Because the large s-wave resonances cause enormous dead-time effects, as described in Sec. 3.3, this problem should be prevented. A self-filtering method is a useful solution to this problem. Figure 3.14 shows a schematic of the self-filtering method. In this method, an indium filter is placed upstream from the target such that the filter absorbs neutrons of the energy of the s-wave resonance. For example, neutrons with energies comparable to the s-wave resonance of 9.07 eV are mostly absorbed by the filter and do not reach the target, whereas neutrons with energies comparable to the p-wave resonance of 6.85 eV are transmitted. This means that the rapid increase in the count rate owing to the γ-rays generated by the s-wave resonance can be suppressed. The self-filter method prevents the V1724 module from stopping when the speed of accumulating data in the local buffer exceeds the speed of writing records to the computer, as described in Sec. 3.3. The indium filter was placed about 1 m upstream from the indium target. Because this position is in the middle of the downstream collimator, the γ-rays emitted from the indium filter were attenuated by the iron collimator material before reaching the germanium detectors. The upstream and downstream collimators were set to open and ϕ7 mm, respectively. The thickness of the lead filter was set to 62.5 mm. A cadmium filter was also installed to prevent excessive activation of the indium target and the filter. Several germanium detectors could not be used because of detector shutdowns caused by insufficient liquid nitrogen filling and significant deterioration of the γ-ray energy resolution owing to radiation damage. During this experiment, among the 22 detectors listed in Tab. 3.2, 16 detectors were available, except for d1, d5, d7, d15, d17, and d21.

3.4.2 Collected data

Three types of measurements were performed in this experiment: an indium target, an empty holder (blank), and a boron carbide target in the target holder. The aim of each measurement and the spectra obtained are explained in the following subsections. For each experimental data, the pulse height acquired using the DAQ was converted to γ-ray energy and TOF was converted to neutron energy. The calibration method is explained in Appendix C.

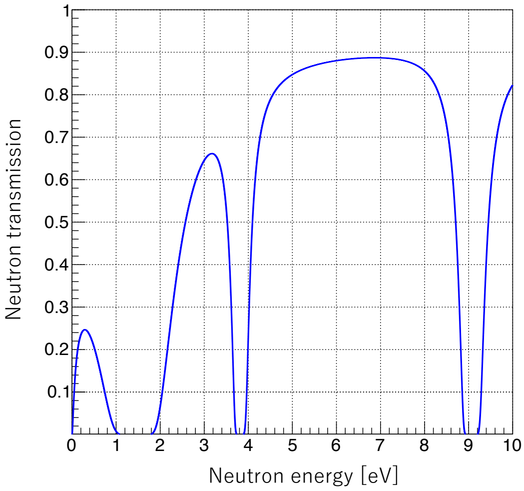

FIGURE 3.15: Neutron transmission of the 4 mm-thick self-filter as a function of the neutron energy.

Indium target

The indium target was measured for three objectives: to determine the asymmetry of the shape of the p-wave resonance of ^{115}In (6.853 eV), to determine the resonance parameter of the p-wave resonance, and to determine the relative transition probability between the respective s-wave (1.46 eV, 3.85 eV, and 9.07 eV) and p-wave resonance. These are in Sec. 4.6, 4.7, and 4.8

The experiment was conducted using indium plates with natural abundance and a purity of 99.99%. The indium target had a size of $40 \times 40 \times 1$ mm^3. The indium self-filter had a thickness of 4 mm and covered the entire ϕ7 mm of the downstream collimator. Figure 3.15 shows a neutron transmission of the 4 mm-thick self-filter as a function of the neutron energy. The neutron transmission of the indium self-filter was calculated as $T_{\mathrm{In}} = \exp(-n_{\mathrm{In}}\sigma_{\mathrm{tot,In}}d_{\mathrm{t}})$, where n_{In} is the number density, $\sigma_{\mathrm{tot,In}}$ is the total cross-section, and d_{t} is the self-filter thickness. Approximately 90% of neutrons with an energy of approximately 6.85 eV, which corresponds to p-wave resonance, pass through the self-filter. Neutrons with energies of 1.46 eV, 3.85 eV, and 9.07 eV, which correspond to s-wave resonances, rarely transmit through the self-filter. As described in Sec. 4.4, under these measurement conditions, pattern 4 events explained in the previous section are sufficiently small and can be ignored in the energy region of the p-wave resonance.

The spectra of the γ-ray and neutron energies are shown in Figs. 3.16 and 3.17, respectively. The values on the vertical axis in these figures were normalized to the number of events per neutron pulse. In these figures, the hatched area represents the indium target measurement, and the shaded area represents the blank measurement. In the γ-ray energy spectrum of the indium target measurement shown in Fig. 3.16, the peaks listed in Tab. 1.4 with higher intensity were observed, which were sufficiently high statistics compared with the spectrum of the blank measurement. In the neutron energy spectrum, the s-wave count rate decreased significantly owing to the self-filtering effect. Neutrons with energies corresponding to the s-wave resonance peak should never reach the target; however, the events were recorded in the region. This can be explained by the data from the blank measurement, as can be observed in the region of 1.46 eV, which has the largest absorption cross-section (3×10^4 barn)

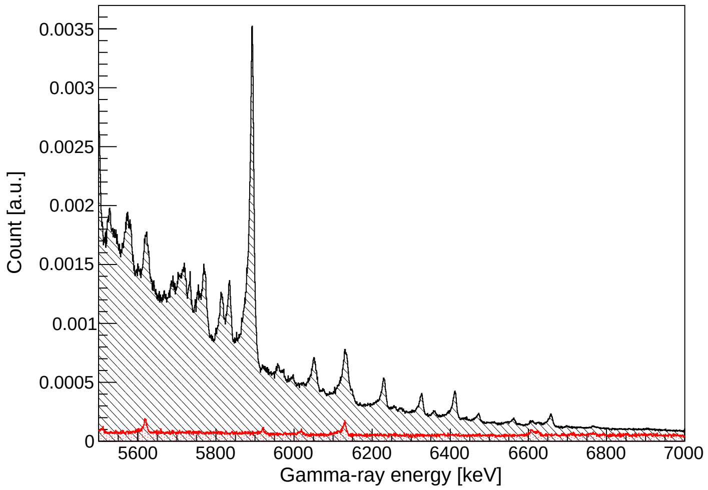

FIGURE 3.16: γ-ray energy spectrum of the indium target measurement (hatched) and blank measurement (shaded). The value on the vertical axis was normalized to the number of events per neutron pulse.

among the resonances of $^{115}\mathrm{In} + \mathrm{n}$.

Boron carbide target

The neutron beam intensity at the MLF has a neutron energy dependence. For the three measurements mentioned above, the neutron energy dependence of beam intensity was required to be corrected. Measurement data using a boron target is useful for this correction. A cross-section of $^{10}\mathrm{B}$ is dominated by the $^{10}\mathrm{B}+\mathrm{n} \rightarrow {}^{7}\mathrm{Li}^{*}+\alpha$ reaction (Fig. 3.18 [71]). This reaction does not have a resonance peak in the region below 10^5 eV and emits only a monochromatic energy γ-ray (477.6 keV) because of $^{7}\mathrm{Li}^{*}$ de-excitation, which makes it easy to separate the background γ-rays from contamination of the target and detector materials. Boron carbide B_4C powder with a mass of 20.1 mg, containing 95% enriched $^{10}\mathrm{B}$, was pressed into tablets of size $\phi 5.08 \times 0.59\ \mathrm{mm}^3$ and used as targets. A 4 mm-thick indium filter was also installed upstream in this measurement to adjust the measurement condition with the indium target measurement. Because the $^{10}\mathrm{B}(\mathrm{n}, \alpha)$ reaction does not have a resonance peak in the extrathermal neutron region and the count rate does not fluctuate rapidly, the event loss owing to the dead time of the DAQ can be ignored.

The spectra of the γ-ray and neutron energies are shown in Figs. 3.19 and 3.20, respectively. The values on the vertical axis in these figures were normalized to the number of events per neutron pulse. In these figures, the hatched area represents the boron target measurement, and the shaded area represents the blank measurement. The 477 keV peak was observed, and the γ-ray events in the energy region above this peak were consistent with the blank measurement data. In the neutron energy spectrum, as for indium measurements, fewer events occurred in the neutron region corresponding to the energy of the s-wave resonance.

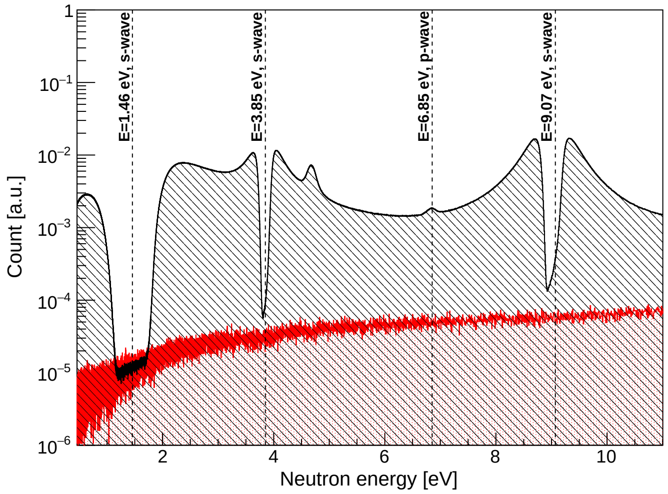

FIGURE 3.17: Neutron energy spectrum of the indium target measurement (hatched) and the blank measurement (shaded). The value on the vertical axis was normalized to the number of events per neutron pulse.

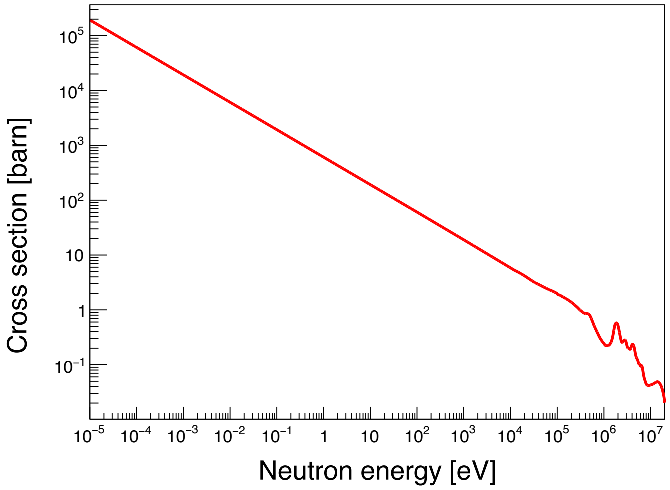

FIGURE 3.18: Cross-sections for each reaction of ^{10}B(n, α) [71].

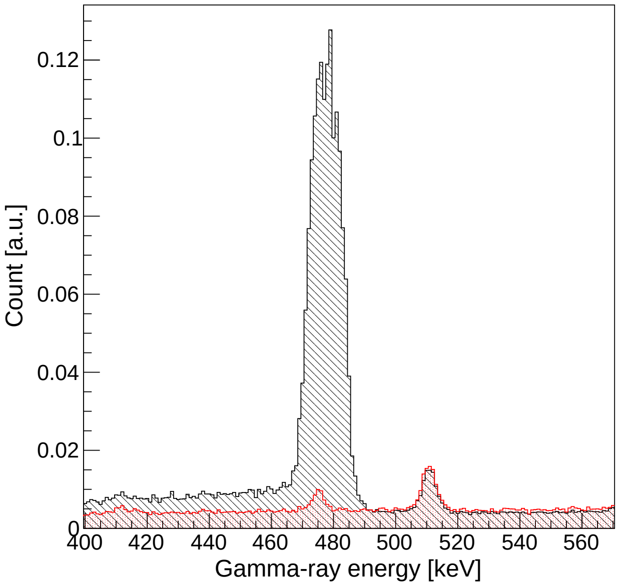

Figure 3.19: 477 keV peak of ^{7}Li* de-excitation by the ^{10}B + n $\rightarrow$ ^{7}Li* + α reaction. The hatched and shaded histograms show the boron carbide target and blank measurements, respectively. The value on the vertical axis was normalized to the number of events per neutron pulse.

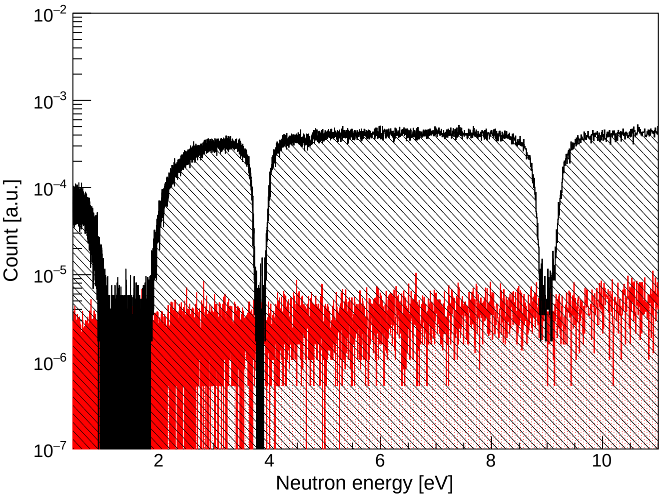

Figure 3.20: Neutron energy spectrum of the boron carbide target measurement. The hatched and shaded histograms represent the boron target and blank measurements, respectively. The value on the vertical axis was normalized to the number of events per neutron pulse.

Chapter 4

Analysis for ϕ and $\kappa(J)$ values

In this chapter, the analysis method of determining ϕ and $\kappa(J)$ values is explained. The analysis flow in this study is described in Sec. 4.1. In the subsequent sections, each part of the analysis flow is explained. Finally, the ϕ and $\kappa(J)$ values are obtained.

4.1 Overview of analysis

Figure 4.1 shows a flow chart of the analysis in this study. The data obtained from the experiments explained in Chap. 3 are used in this analysis, and the ϕ value is obtained by comparing the analysis results with theoretical calculations.

In the analysis of the experimental data, the first step is to perform event selection using γ-ray peaks. This is because the final state spins must be fixed in the theoretical calculations explained in Chap. 2. The γ-rays used in the analysis are discussed in Sec. 4.2. After event selection, the backgrounds considered in this study and subtracting them are explained in Sec. 4.3. Section 4.4 describes the recovery of the event loss due to the DAQ dead time, as discussed in Sec. 3.3. Section 4.5 describes the normalization of the beam intensity of the experimental facility with respect to neutron energy dependence. Section 4.6 presents the experimental results of the angular dependence of the asymmetries of the p-wave resonance.

The theoretical calculations are based on Chap. 2. Among the input parameters for the theoretical calculations, the resonance width and transition probability of the p-wave resonance was determined in this study. The methods used to determine them are described in Sec. 4.7 and4.8. Finally, in Sec. 4.9, the asymmetry of the p-wave resonance obtained using theoretical calculations with these parameters as input is described, and the values of ϕ and $\kappa(J)$ obtained by comparing them with the experimental results are presented.

4.2 Selection of γ-ray peak to fix final state spin

The value of ϕ can be determined by evaluating the shape of the p-wave resonance using a neutron energy distribution, where the events are selected using γ-ray peaks for which the value of the final state spin F is already known. The first step is to select γ-ray peaks with a large transition probability from the p-wave resonance state. The γ-ray energy spectrum shown in Fig. 4.2 was obtained by selecting events with neutron energy in the range of ±0.30 eV from the p-wave resonance energy of 6.85 eV and adding them to all detectors. Full absorption peaks of γ-rays can be observed at 6471 keV ($F = 5$), 6136 keV ($F = 6$), 5971 keV, 5956 keV ($F = 4$), 5892 keV ($F = 4$), and 5833 keV ($F = 4$). As the final state spins assigned to these γ-ray peaks are all $F = 4,\ 5,$ or 6, which are listed in Tab. 1.4, they can potentially determine the ϕ value, as described in Sec. 2.2. These γ-ray peaks are tagged from (a) to (e).

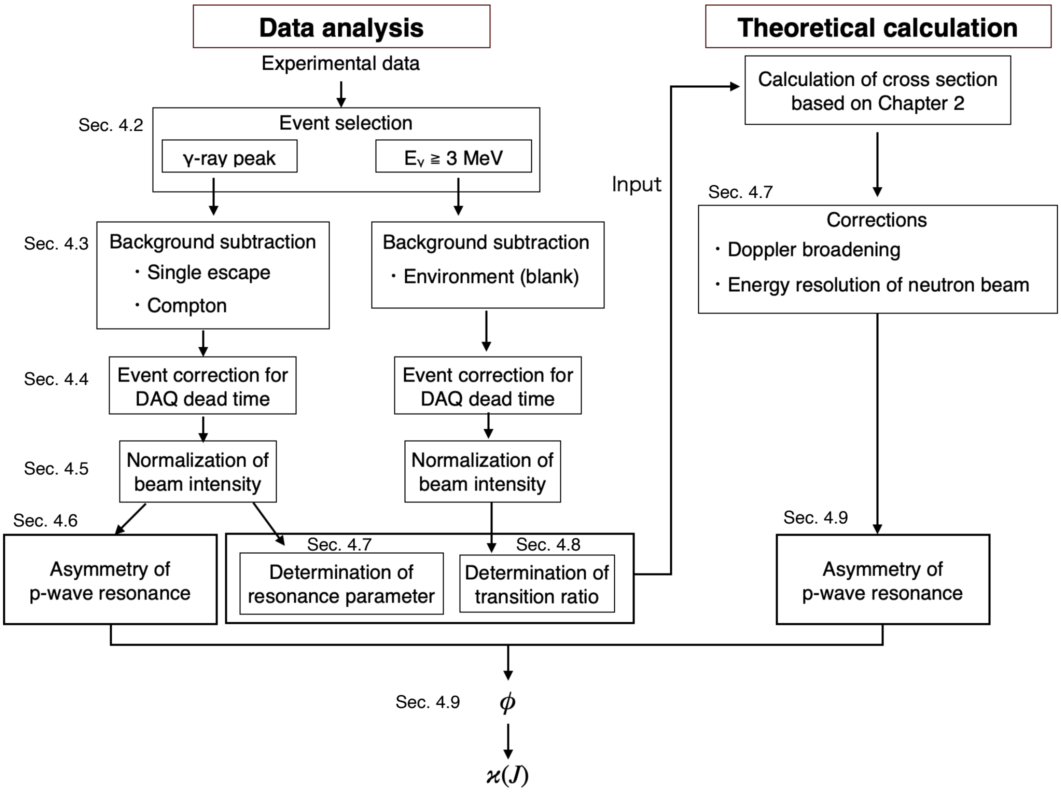

FIGURE 4.1: Analysis flow chart to determine ϕ and $\kappa(J)$ values for ^{115}In.

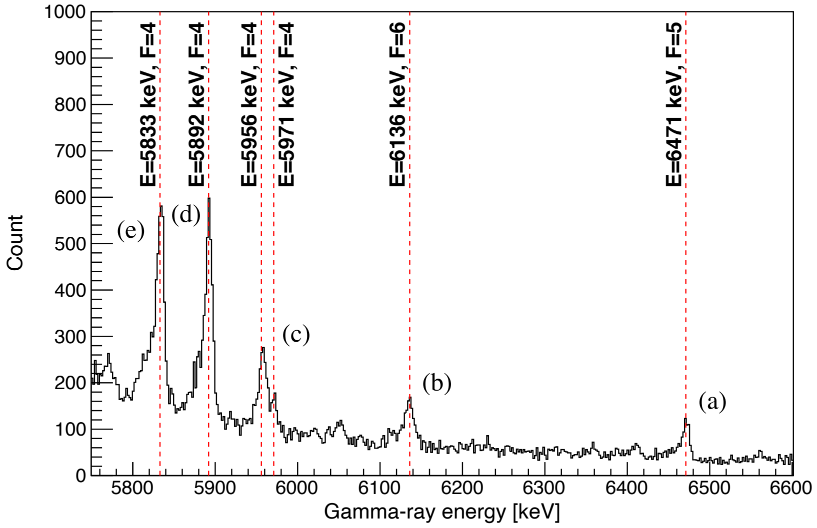

FIGURE 4.2: γ-ray energy spectrum gated with p-wave energy region (6.85 ± 0.30 eV). (a) 6471 keV ($F = 5$) peak, (b) 6136 keV ($F = 6$), (c) 5971 keV and 5956 keV ($F = 4$) peaks, (d) 5892 keV ($F = 4$) peak, and (e) 5833 keV ($F = 4$) peak.

However, the 5971 keV and 5956 keV peaks are difficult to separate from the energy resolution of the germanium detector. The two peaks are considered as one 5960 keV peak, which is tagged as (c) because they have the same final state spin $F = 4$. In the γ-ray energy region above 6471 keV, no higher-energy peaks than those listed in Tab. 1.4 are visible. The energy region below 5800 keV is neglected in the following discussion because multiple γ-ray peaks with different final state spins F overlap and are difficult to separate.

Figure 4.3(a) shows the neutron energy spectra obtained by selecting events and adding them for all detectors for γ-ray energies from 6435 keV to 6480 keV, (b) from 6125 keV to 6145 keV, (c) from 5930 keV to 5980 keV, (d) from 5880 keV to 5900 keV, and (e) from 5820 keV to 5840 keV. Here, each condition from (a) to (e) in Fig. 4.3 corresponds to the energy region containing the γ-ray peak tagged in Fig. 4.2. Comparing each of the distributions from (a) to (e), the p-wave resonance is most clearly visible when the events are selected in region (c). This means that the γ-ray peak in region (c) has a higher probability of being emitted from the p-wave resonance, whereas the other peaks have a higher probability of being emitted from the s-wave resonance than from the p-wave resonance. It is easier to evaluate the peak shape of the p-wave resonance quantitatively if the p-wave resonance is observed significantly more than the base of the s-wave resonance. Therefore, region (c) is defined as the signal region, and the analysis and results for the signal region are described below.

4.3 Subtraction of backgrounds

4.3.1 Structure of backgrounds and subtraction methods

The signal region has two types of backgrounds: the single escape background, which is formed by a single escape of 6471 keV γ-rays, and the Compton background, which

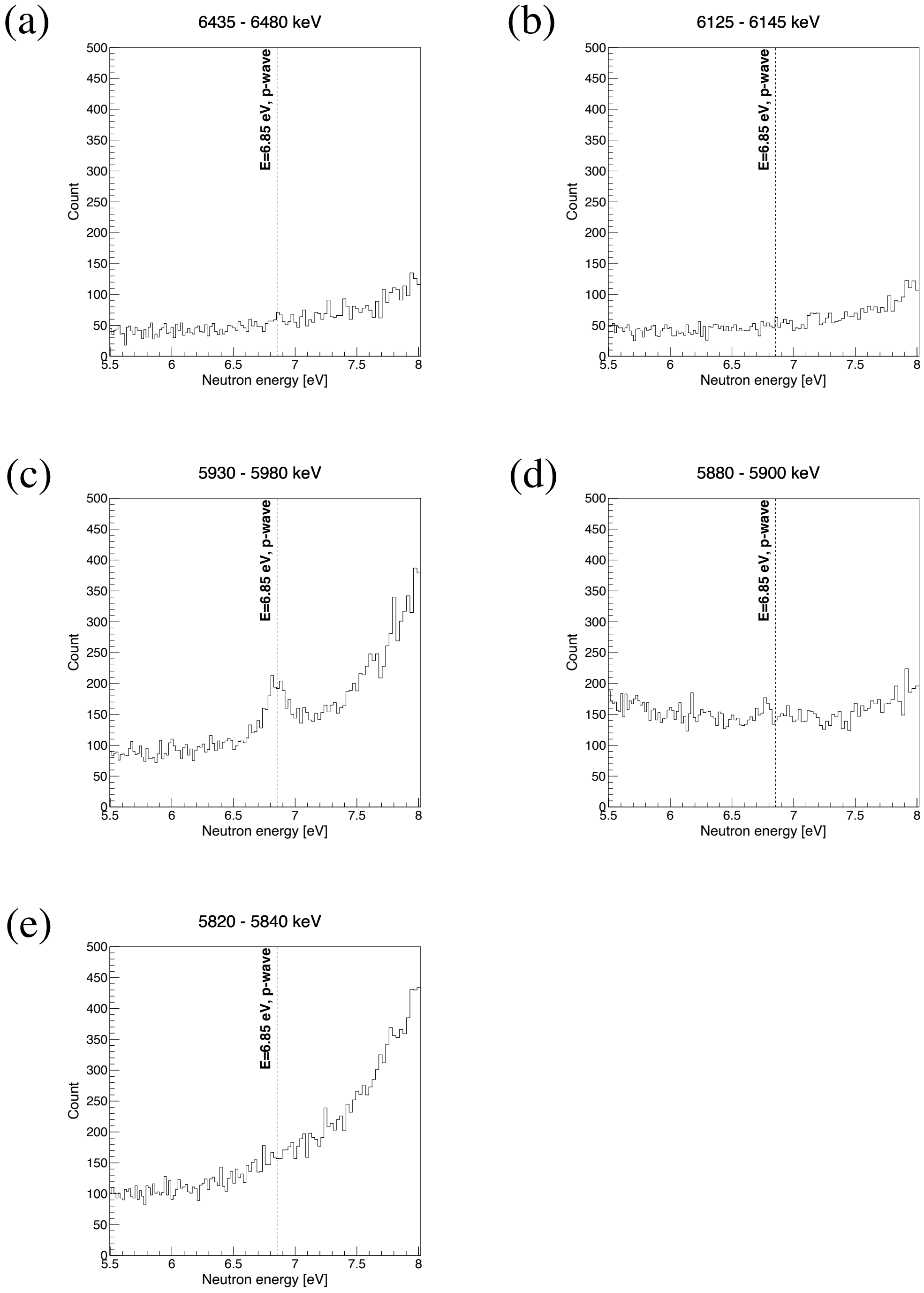

FIGURE 4.3: Neutron energy spectrum for p-wave region gated with each γ-ray energy region.

is formed by a γ-ray peak with an energy higher than 5960 keV being absorbed after Compton scattering and energy reduction.

Figure 4.4 shows a schematic diagram of the structure of these backgrounds. The solid lines depict the γ-ray energy spectrum obtained from the measurement of the indium target, and the dotted lines depict each background. The single escape peak of 6471 keV γ-ray is the main background. The single escape peak at 6471 keV overlapped with the signal region (Fig. 4.4). The 5960 keV ($F = 4$) and 6471 keV ($F = 5$) peaks have different final state spins F, which may result in an incorrect angular dependence of the asymmetry of the p-wave resonance. This background was estimated using the Geant4 simulation with accurate implementation of the ANNRI detector and surrounding materials. Figure 4.5 shows a picture of the detectors in the ANNRI implemented in the Geant4 simulation, cut in the plane containing the y-axis in the coordinate system described in Chap. 3. As the details of the simulation are explained in Ref. [63], the following is a description of estimating the spectra and background obtained from the simulation. The amount of leakage of the 6471 keV single escape peak into the signal region was estimated by simulating the isotropic emission of the 6471 keV monoenergetic γ-rays from the target. Figure 4.6 shows an example of the estimation of the single escape background for detector d22. Scaling between the experimental and simulated data was performed to match the intensities of the full absorption peak of 6471 keV. The open area is the γ-ray energy spectrum selecting events with neutron energy in the range of ±0.30 eV from the p-wave resonance energy of 6.85 eV. The shaded area is the response function for the 6471 keV monoenergetic γ-ray using the simulation in Ref. [63]. The single escape peak of 6471 keV was comparable in magnitude to that of the 6471 keV peak. A correction owing to the individuality of the germanium crystal size was considered in the simulation, which is discussed in Sec. 4.3.2.

The Compton background is a flat-structured background (Fig. 4.4(b)). This background is formed by the stacking of Compton tails of γ-rays of various energies, resulting in a continuous spectrum. Therefore, the filled region (Fig. 4.4(b)) and the immediately neighboring shaded region were considered to be the energy spectrum of the same structure. The Compton background was subtracted using the neutron energy spectrum obtained by gating in the 5980 keV to 6130 keV region.

Figure 4.7 shows the neutron energy spectrum obtained by subtracting these backgrounds and summing them for all detectors. The open area is the neutron energy spectrum selecting the events of region (c). The shaded area is the neutron energy spectrum after subtracting the backgrounds described above. The restoration of event loss owing to the dead time of the DAQ system and the normalization of the neutron flux (described in Sec. 4.4 and 4.5, respectively) were applied to this shaded spectrum, and the shape of the p-wave resonance was quantitatively evaluated based on its asymmetry.

(a) Single escape background

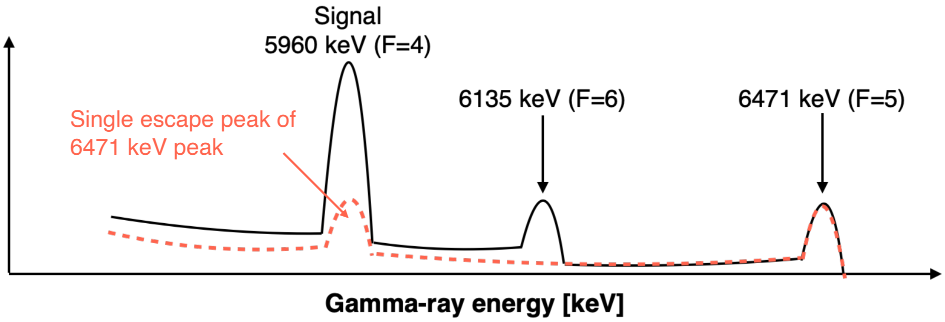

(b) Compton background

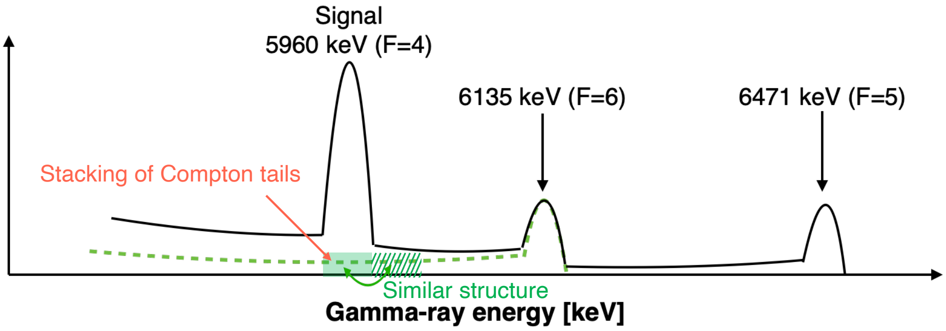

FIGURE 4.4: Structure of γ-ray energy spectrum near the 5960 keV peak. The solid line indicates the measured spectrum. The dotted lines in (a) depict a single escape background and those in (b) depict the Compton background.

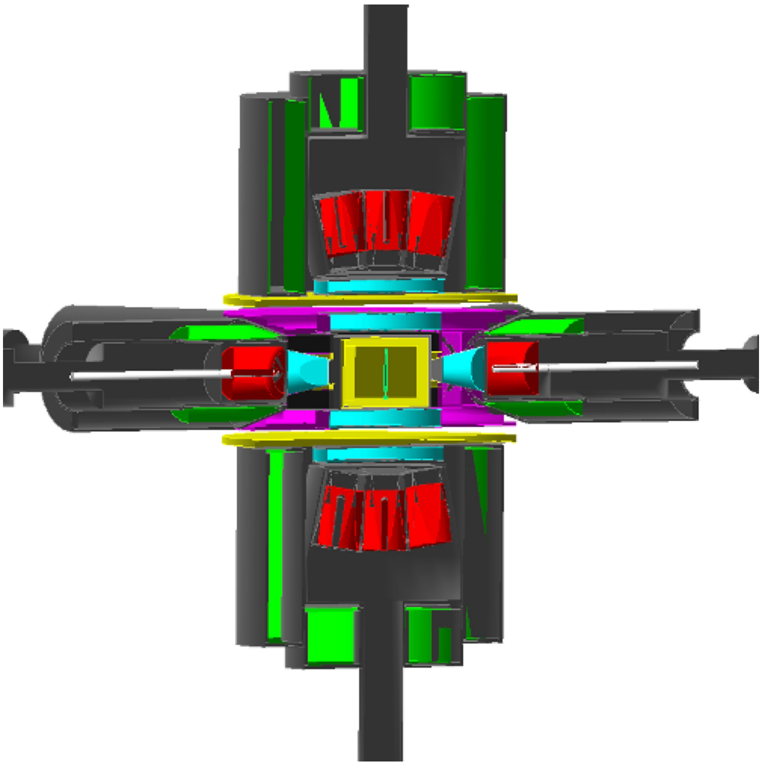

FIGURE 4.5: Image of the detectors in the ANNRI implemented in the Geant4 simulation.

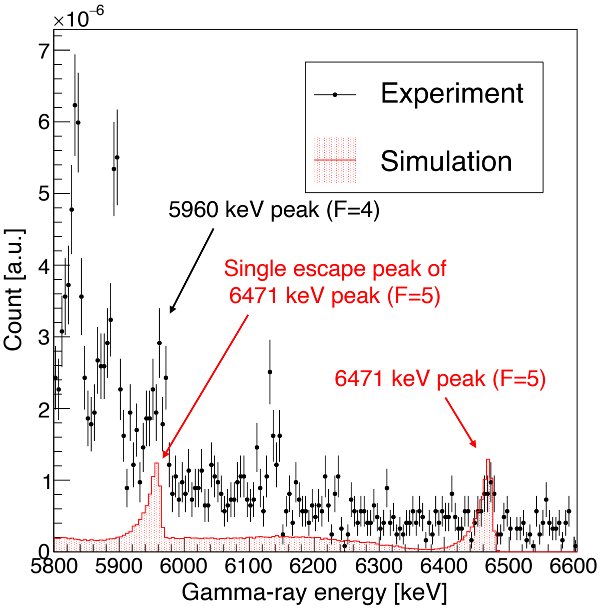

FIGURE 4.6: Estimation of the single escape background caused by 6471 keV, example for detector d22. The open spectrum represents the measurement data, and the shaded area represents the simulated response function of the monoenergetic γ-ray of 6471 keV. The response function was obtained in the Geant4 simulation [63].

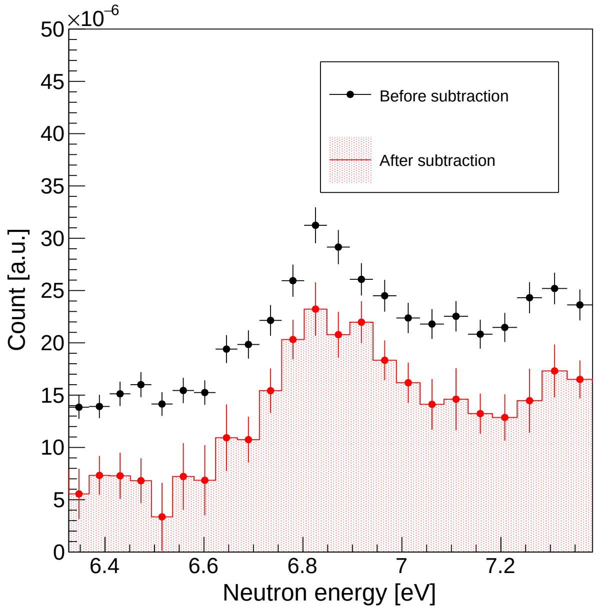

Figure 4.7: Comparison of γ-ray energy spectra between before (open) and after (shaded) subtraction of the backgrounds.

4.3.2 Correction for the simulation of single escape peak

Typical values of germanium crystal sizes from the specification sheets were applied to the simulations. However, owing to the individuality of crystal growth, the actual germanium crystal size varied between the detectors. The exact crystal size was unknown because the crystal container was completely sealed. This meant that the area of the single escape peak determined by the simulation had uncertainty and required to be corrected for each detector. The correction factors for the simulation were calculated by comparing the experimental and simulation values of the 10829 keV γ-ray peak of $^{14}\mathrm{N}(\mathrm{n},\gamma)$ in the melamine target with its single escape peak. Because the maximum neutron separation energy for the compound nucleus was approximately 12 MeV, this energy region had almost no background. Figure 4.8 shows a comparison of the γ-ray energy spectrum obtained from the experiment of a melamine target and a simulation for the 10829 keV γ-ray; this is an example for detector d22. The open spectrum shows the experimental data of the melamine target, and the shaded spectrum is the response function for the monoenergetic 10829 keV γ-ray simulated using the Geant4 simulation in Ref. [63]. The experimental and simulated spectra were normalized to the area of the total absorption peak. The ratios of the experimental and simulation values of the single escape peak were averaged at approximately 5%., which are summarized in Tab. 4.1. These values were applied as corrections when subtracting the single escape background, but the effect of this correction on the final results of ϕ and $\kappa(J)$ was sufficiently small compared with the statistical error.

Table 4.1: Correction factor of the simulation of the single escape peak.

Detector	Ratio of single escape peak (Experiment/Simulation)
d1	–
d2	1.035 ± 0.026
d3	1.095 ± 0.029
d4	1.040 ± 0.026
d5	–
d6	1.028 ± 0.025
d7	–
d8	1.123 ± 0.028
d9	1.007 ± 0.026
d10	1.011 ± 0.025
d11	1.114 ± 0.027
d12	1.105 ± 0.028
d13	1.060 ± 0.027
d14	1.049 ± 0.026
d15	–
d16	0.670 ± 0.019
d17	–
d18	1.098 ± 0.030
d19	1.012 ± 0.026
d20	0.918 ± 0.023
d21	–
d22	1.366 ± 0.038

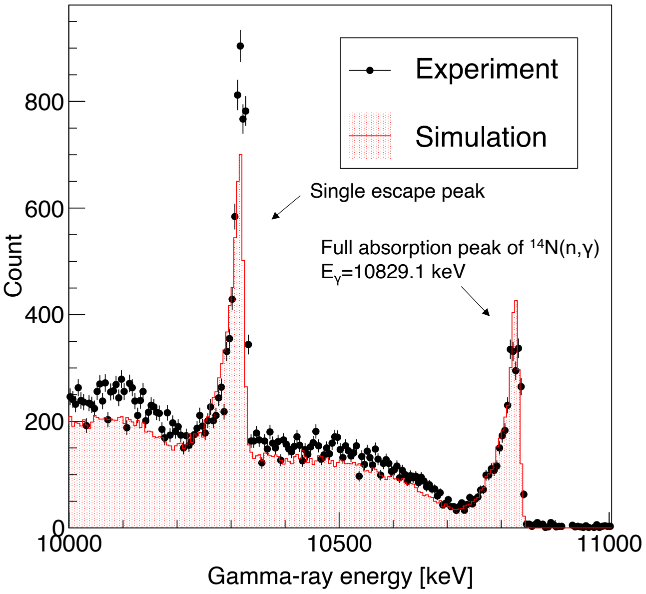

FIGURE 4.8: Comparison of γ-ray energy spectra of the experiment and simulation for monoenergetic 10829 keV γ-ray; example for detector d22. The experimental spectrum was measured using the melamine target. The simulated spectrum was obtained for the monoenergetic 10829 keV γ-ray.

4.4 Restoration of the event loss caused by the dead time of the DAQ system

As discussed in Sec. 3.3, the DAQ system may record the pulse height as zero depending on the time intervals between the two signals owing to the behavior of patterns 2 and 3. Some of the γ-rays with energies of approximately 5960 keV were recorded as events with a pulse height of zero. This event can be recovered by the following equation

$$N_{E_\gamma=5960\ \mathrm{keV,true}} = N_{E_\gamma=5960\ \mathrm{keV}} \times \frac{N_{E_\gamma>0} + N_{E_\gamma=0}}{N_{E_\gamma>0}}, \tag{4.1}$$

where $N_{E_\gamma=5960\ \mathrm{keV,true}}$ is the original number of events in the signal region, $N_{E_\gamma=5960\ \mathrm{keV}}$ is the number of events recorded as approximately 5960 keV, $N_{E_\gamma=0}$ is the number of events recorded with a zero pulse height, and $N_{E_\gamma>0}$ is the number of events with a nonzero pulse height. The restoration factor $\frac{N_{E_\gamma>0}+N_{E_\gamma=0}}{N_{E_\gamma>0}}$ has the following relationship:

$$\frac{N_{E_\gamma>0}}{N_{E_\gamma>0} + N_{E_\gamma=0}} = 1 - \frac{N_{E_\gamma=0}}{N_{E_\gamma>0} + N_{E_\gamma=0}}.$$

Because the ratio $\frac{N_{E_\gamma=0}}{N_{E_\gamma>0}+N_{E_\gamma=0}}$ is the probability of loss of the γ-ray energy information because of pattern 2 or 3 of the DAQ dead time explained in Sec. 3.3, a restoration factor close to 1 implies that the restoration amount is small. Because the probability of event loss depends on the count rate, the restoration factor depends on the neutron energy and has a large value, particularly near the resonance peak. Furthermore, because the radio activation of $^{\mathrm{nat}}\mathrm{In}(\mathrm{n},\gamma)$ saturates over several hours, the count rate varies gradually over the first few hours of beam injection (i.e., the first few hours of data acquisition) and when the facility stops and restarts the beam operation. Therefore, the lost events were repaired in two dimensions: neutron energy and data acquisition time. Focusing on the neutron energy region around the p-wave resonance of 6.85 eV, the probability of the event loss was less than 4% and did not depend on the data acquisition time.

The amount of loss for the unrecoverable events in pattern 4 can be estimated from this restoration value. Assuming that the counting rate is nearly constant in the p-wave resonance region, the ratio of t_2 to t_0, described in Sec. 3.3, indicates the ratio of the number of events lost in pattern 4 to the number of events recorded as the pattern 2 or 3. The value of the ratio t_2/t_0 was $\sim 6.8\%$. The probability of the occurrence of an unrecoverable event was estimated by multiplying this value by the probability of the event loss obtained above. The probability in the pattern 4 is approximately $4\% \times 6.8\% \sim 0.3\%$. This is a sufficiently small value compared with the error of ϕ, which is discussed later, and the effect of the event loss due to pattern 4 can be ignored.

4.5 Normalization of neutron energy dependence of the beam intensity

The intensity of the neutron beam reaching the target depends on the neutron energy for two reasons: First, the neutron beam intensity of the MLF has a neutron energy dependence. Second, the beam intensity was unique to this experiment because of the insertion of a self-filter. Eliminating these contributions enables a direct comparison with theoretical calculations.

The neutron energy dependence can be normalized using the measurement data of the boron target, as described in Sec. 3.4. The main component of the data obtained with the boron target was the 477 keV γ-ray peak owing to the $^{10}\mathrm{B}(\mathrm{n},\alpha)$ reaction. Because the γ-ray events above the 477 keV peak were background owing to the (n,γ) reaction caused by the materials around the detector, they were subtracted using the data of the blank measurement. To select the events more purely, we gated each experimental data point in the region from 470 keV to 480 keV, which contained the 477 keV peak. Figure 4.9 shows the neutron energy dependence of the neutron beam intensity finally obtained from the data analysis of the boron target measurement data. Here, because the absorption cross-section of the boron target also had a neutron energy dependence, its effect was already removed by dividing by the $^{10}\mathrm{B}(\mathrm{n},\alpha)$ cross-section shown in Fig. 3.18. The depression near the resonance energy of the indium s-wave resonance in the spectrum shown in Fig. 4.9 shows the effects of self-filtering. The dependence of the beam intensity on the neutron energy was normalized by dividing the spectrum shown in Fig. 4.7 with the beam intensity spectrum shown in Fig. 4.9.

4.6 Asymmetry of p-wave resonance

The p-wave resonance shapes obtained by applying the analysis described in Sec. 4.3 through to Sec. 4.5 to the experimental data are shown in Fig. 4.10 for each detection angle. The data obtained at the 36.0°, 70.9°, 72.0°, 90.0°, 108.0°, 109.1°, and 144.0° detectors are plotted from top left to bottom right, respectively. The horizontal axis

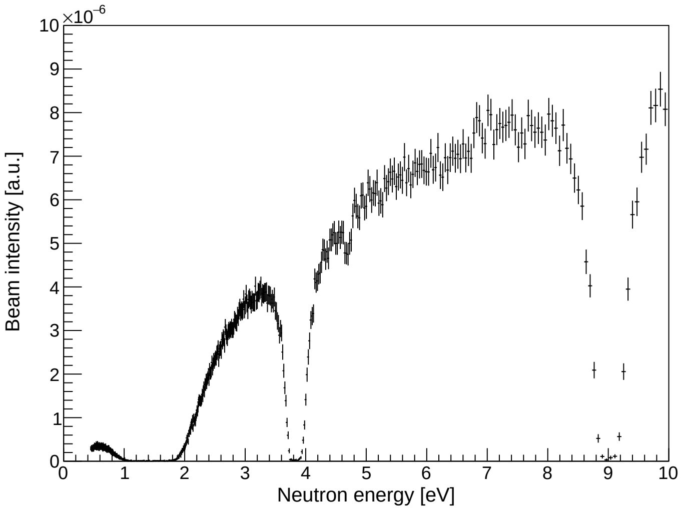

FIGURE 4.9: Neutron beam intensity as a function of neutron energy.

represents the neutron energy, and the vertical axis represents an arbitrary unit proportional to the cross-section. Here, the vertical axes of these figures were normalized such that the area of each histogram was the same in the energy region of the figure. The solid line is the p-wave resonance plotted according to the theoretical calculations in Chap. 2. Here, ϕ obtained in Sec. 4.9 was used. The ϕ value was obtained by comparing the shape of the p-wave resonance at each of these detection angles with the values obtained from theoretical calculations.

To quantitatively evaluate the shape of the p-wave resonance, we defined the integration region to calculate asymmetries. The regions at energies lower and higher than the resonance energy of the p-wave resonance are depicted in Fig. 4.11, using 109.1° in Fig. 4.10 as an example. The low-energy side ranged from 6.53 eV to 6.85 eV and the high-energy side ranged from 6.85 eV to 7.18 eV. The range of the integration region is arbitrary provided it is consistent between the analysis of the experimental data and the theoretical calculation.

The effective detection angle of the γ-rays should be considered before discussing the angular dependence of asymmetries. The angles at which the γ-rays were fully absorbed in the germanium crystal differed slightly from the installed angles, as summarized in Tab. 3.2. This was because of the location of the germanium crystals and the Pb γ-ray collimators described in Sec. 3.1.3. This has been observed using simulations and reported in Ref. [63]. Because the effective angles depend on the γ-ray energy, simulations for 5960 keV γ-rays were performed in this study and are summarized in Tab. 4.2. This effect has been particularly observed in some type-A detectors (installed angles of 70.9° and 109.1°), where the angle changes by 1.6°.

Figure 4.12 shows the asymmetries with respect to the effective detection angle. Each point represents the asymmetry of the peak shape of the p-wave resonance at each angle in Fig. 4.10, calculated using Eq. 2.5. The angular dependence of the asymmetry can be fitted using Eq. 2.6, as described in Chap. 2, and it is represented by the solid line in Fig. 4.12. The asymmetries of coefficients A_0, A_1, and A_3 were obtained as

$$A_0 = -0.068 \pm 0.046,$$

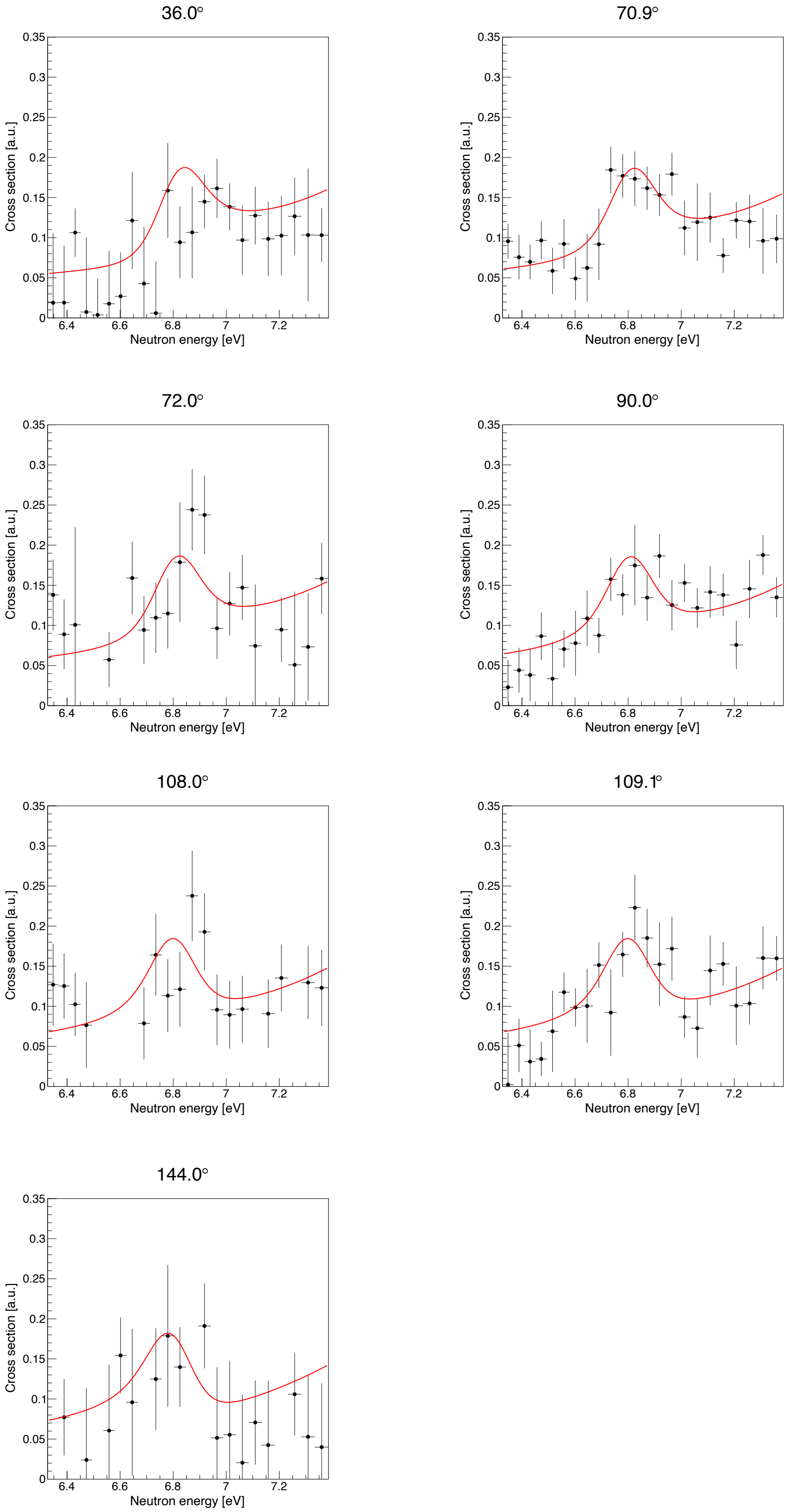

FIGURE 4.10: Shapes of the p-wave resonance for each angle. The solid lines are plotted based on theoretical calculations in Chap. 2. Here, the ϕ value obtained in Sec. 4.9 was used.

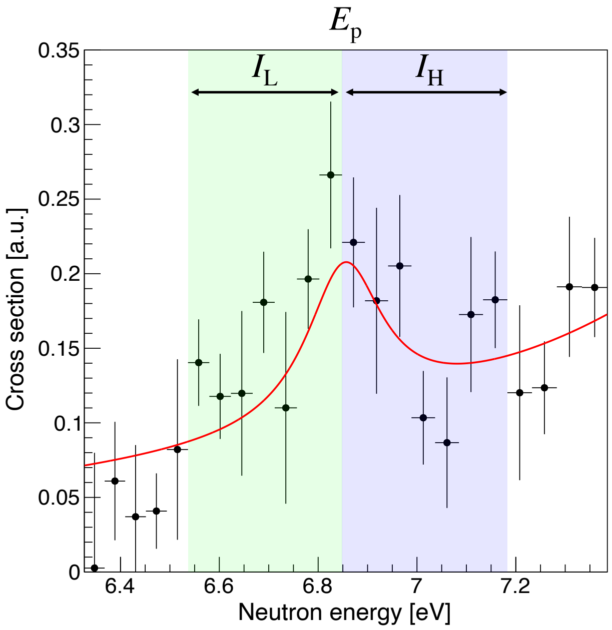

FIGURE 4.11: Definition of the integral ranges for the calculation of the asymmetry A_{LH}. The solid line represents the eye-guide. The bands show the integral ranges for the lower and higher-energy regions.

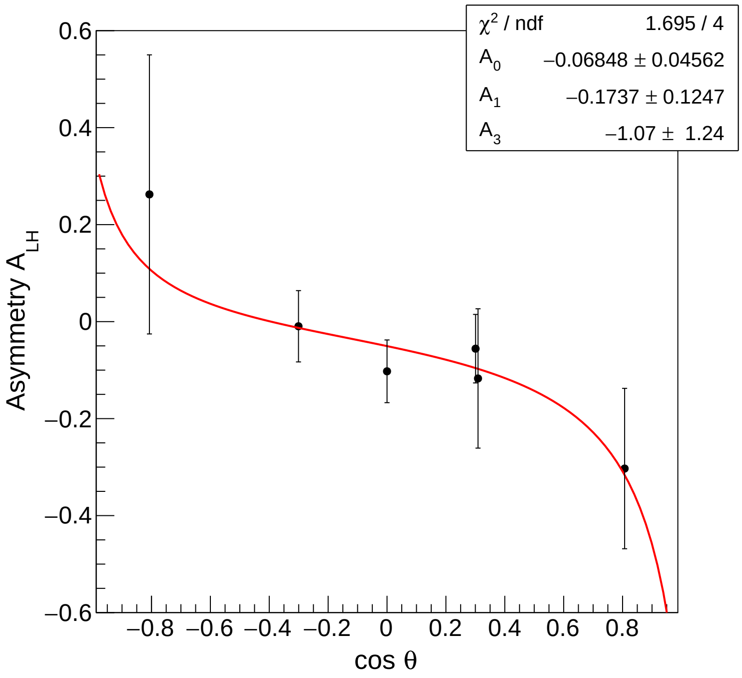

FIGURE 4.12: Angular dependence of the A_{LH} value. The solid line represents the fitting results obtained using Eq. 2.6.

TABLE 4.2: Effective detection angles of the germanium detectors for the full absorbed events of γ-rays. They were obtained using the Geant4 simulation [63] for a γ-ray energy of 5960 keV.

Installed angle [°]	Effective detection angle [°]
36.0	36.2
70.9	72.5
72.0	72.0
90.0	90.0
108.0	108.0
109.1	107.5
144.0	143.8

$$\begin{aligned} A_1 &= -0.174 \pm 0.125, \text{ and} \\ A_3 &= -1.070 \pm 1.240. \end{aligned} \tag{4.2}$$

The value of ϕ can be obtained by comparing this value with the theoretical calculation. First, in Sec. 4.7 and 4.8, some parameters necessary for theoretical calculations obtained from the experiment are described.

4.7 Resonance parameters

In the theoretical calculations based on s-p mixing described in Chap. 2, the resonance width and energy of each resonance are necessary as input parameters. The resonance parameters of ^{115}In can be obtained by fitting Breit–Wigner functions to the neutron energy spectrum measured with the $^{\mathrm{nat}}$In target. Here, the broadening of the resonance peak caused by the Doppler effect and time structure of the pulsed neutron beam cannot be eliminated by the analyses described from Sec. 4.3 to 4.5 and must be convoluted into a Breit–Wigner function. Most of the resonance parameters for ^{115}In are summarized in Tab. 1.3, but only the γ width of the p-wave resonance was not determined in previous studies [47]. In this section, the convolution method of each broadening effect is presented, and the resonance width of the p-wave resonance of 6.85 eV is obtained.

4.7.1 Doppler broadening effect

The apparent energy of the neutron, as observed from the nucleus, oscillates because the nucleus in the target is thermally oscillating. Considering the ideal gas model [72, 73], the cross-section including the thermal oscillations of the nucleus can be expressed as follows:

$$\bar{\sigma}(E) = \int dE_{\mathrm{cm}} S\left(E, E_{\mathrm{cm}}\right) \sigma\left(E_{\mathrm{cm}}\right), \tag{4.3}$$

$$E_{\mathrm{cm}} = \frac{1}{2} m_{\mathrm{n}} (v \pm u)^2 \approx E_{\mathrm{n}} \pm u \sqrt{2 m_{\mathrm{n}} E_{\mathrm{n}}} \tag{4.4}$$

where E_{cm} is the center-of-mass energy between a neutron flying at velocity v and the target nucleus when it thermally vibrates at velocity u. The function $S\left(E, E_{\mathrm{cm}}\right)$ is the energy transfer function [74] owing to thermal oscillations, and it is expressed by the following equation, which follows the Maxwell–Boltzmann distribution:

$$S\left(E, E_{\mathrm{cm}}\right)=\frac{1}{\Delta \sqrt{\pi}} \exp \left[-\left(\frac{E_{\mathrm{cm}}-E}{\Delta}\right)^{2}\right], \tag{4.5}$$

$$\Delta \equiv \sqrt{\tfrac{4 E k_{\mathrm{B}} T}{M / m_{\mathrm{n}}}}, \tag{4.6}$$

where k_B is the Boltzmann constant, M is the mass of the nucleus, and Δ is the Doppler width. Because $E \gg \Delta$, the convoluted cross-section $\bar{\sigma}(E)$ can be approximated by the following equation [75]:

$$\bar{\sigma}(E)=\frac{1}{\Delta \sqrt{\pi}} \int d E_{\mathrm{cm}} \exp \left[-\left(\frac{E_{\mathrm{cm}}-E}{\Delta}\right)^{2}\right] \sqrt{\frac{E_{\mathrm{cm}}}{E}} \sigma\left(E_{\mathrm{cm}}\right). \tag{4.7}$$

This expression implies that the width of the resonance peak is broadened by Δ, which depends on the temperature T of the experimental environment and the neutron energy E_{n}.

4.7.2 Energy resolution of a pulsed neutron beam

The neutron energy is converted from the TOF of the neutron from the moderator surface to the target using Eq. C.1. However, because the trigger for the time information recorded by the DAQ system is synchronized with the timing of the proton injection, as described in Sec. 3.3, the neutron moderation time in the moderator, which is explained in Sec. 3.2, must be considered. The neutron moderation process in the moderator was simulated, and the equation is explained in Sec. 3.2. The cross-section that considers the neutron moderation process is described by the following equation:

$$\begin{aligned}
\tilde{\sigma}\left(E_{\mathrm{n}}^{\mathrm{m}}\right) &= \int d E_{\mathrm{n}} \psi\left(E_{\mathrm{n}}, t^{\mathrm{m}}\right) \sigma\left(E_{\mathrm{n}}\right) E_{\mathrm{n}}^{-\frac{3}{2}} \\
&= \int d \tilde{E} \psi\left(E_{\mathrm{n}}^{\mathrm{m}}+\tilde{E}, t^{\mathrm{m}}\right)\left(E_{\mathrm{n}}^{\mathrm{m}}+\tilde{E}\right)^{-\frac{3}{2}}, \quad (\tilde{E} \geq 0).
\end{aligned} \tag{4.8}$$

4.7.3 Resonance width of p-wave resonance

The cross-section convoluted with the Doppler broadening effect and energy resolution of the pulsed neutron beam, $\sigma'\left(E_{\mathrm{n}}^{\mathrm{m}}\right)$, is described as

$$\begin{aligned}
\sigma'\left(E_{\mathrm{n}}^{\mathrm{m}}\right) = & \int d \tilde{E} \psi\left(E_{\mathrm{n}}^{\mathrm{m}}+\tilde{E}, t^{\mathrm{m}}\right)\left(E_{\mathrm{n}}^{\mathrm{m}}+\tilde{E}\right)^{-\frac{3}{2}} \frac{1}{\Delta \sqrt{\pi}} \\
& \times \int d E_{\mathrm{cm}} \exp \left[-\left(\frac{E_{\mathrm{cm}}-\left(E_{\mathrm{n}}^{\mathrm{m}}+\tilde{E}\right)}{\Delta}\right)^{2}\right] \sqrt{\frac{E_{\mathrm{cm}}}{E_{\mathrm{n}}^{\mathrm{m}}+\tilde{E}}} \sigma\left(E_{\mathrm{cm}}\right),
\end{aligned}$$

$$\Delta=\sqrt{\frac{4\left(E_{\mathrm{n}}^{\mathrm{m}}+\tilde{E}\right) k_{\mathrm{B}} T}{M / m_{\mathrm{n}}}}.$$

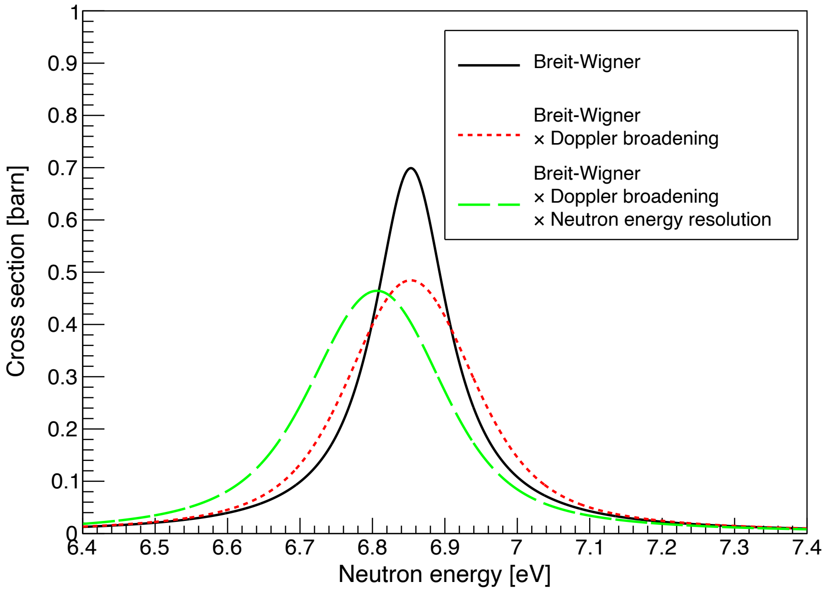

FIGURE 4.13: Scheme of convolutions for each correction. The solid, dotted, and dashed lines represent the normal Breit–Wigner function, Breit–Wigner function with Doppler broadening, and Breit–Wigner function with Doppler broadening and neutron energy resolution, respectively.

The Breit–Wigner functions convoluted with the effects of Doppler broadening and neutron energy resolution are shown in Fig. 4.13. The solid, dotted, and dashed lines represent the normal Breit–Wigner function, Breit–Wigner function with Doppler broadening, and Breit–Wigner function with Doppler broadening and neutron energy resolution, respectively. The convolution of these effects does not change the area of the resonance peak but increases its width.

The p-wave resonance width was obtained by fitting the convoluted Breit–Wigner function to the experimental neutron energy spectrum. The neutron energy spectrum was gated at $E_\gamma \geq 3$ MeV to exclude low-energy background events, such as γ-rays emitted by transitions from low excited states and electrical noise. The method described in Sec. 4.4 and 4.5 was applied to recover the event loss due to the dead time of the DAQ and normalize the beam intensity. Background contamination due to (n, γ) reactions in the detector components was subtracted using the data from the blank measurement. The convoluted Breit–Wigner function used for fitting consisted of three s-wave resonances and one p-wave (Tab. 1.3). The result of the fitting is shown in Fig. 4.14. The solid line is the convoluted Breit–Wigner function, where the free parameters are the height of the function C and the γ width of the p-wave resonance $\Gamma_{\gamma,3}$. In addition, the resonance parameters and temperatures were fixed at the central values listed in Tab. 1.3 and room temperature, respectively. The γ width of the p-wave resonance was obtained as $\Gamma_{\gamma,3} = 125 \pm 2$ meV. The resonance parameters of ^{115}In are summarized in Tab. 4.3, including the results of the study.

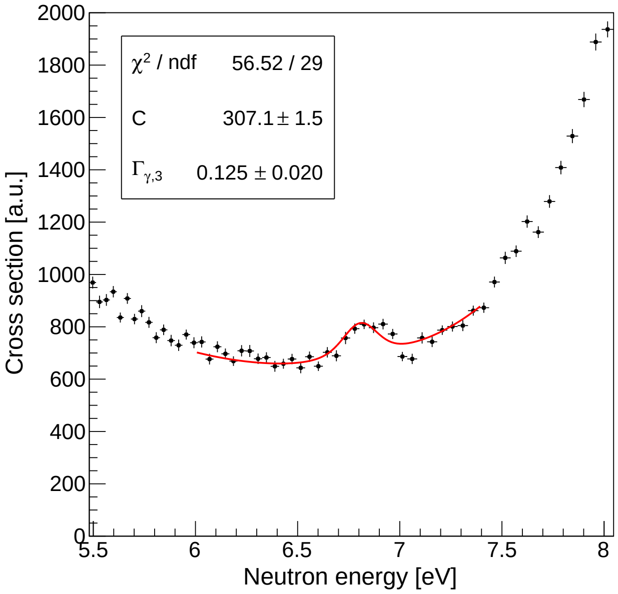

FIGURE 4.14: Fitting result of resonance width of p-wave resonance. The solid line represents the convoluted Breit–Wigner function.

TABLE 4.3: Resonance parameters of ^{115}In, including the result of this study.

r	E_0 [eV]	J	l	$2g\Gamma_{\rm n}$ [meV]	Γ_γ [meV]
1	1.457 ± 0.002	5	0	3.28 ± 0.06	72 ± 2
2	3.85 ± 0.01	4	0	0.339 ± 0.013	81 ± 4
3	6.853 ± 0.009	5	1	0.00046 ± 0.00004	125 ± 2 (this work)
4	9.07 ± 0.04	5	0	1.69 ± 0.12	80 ± 40

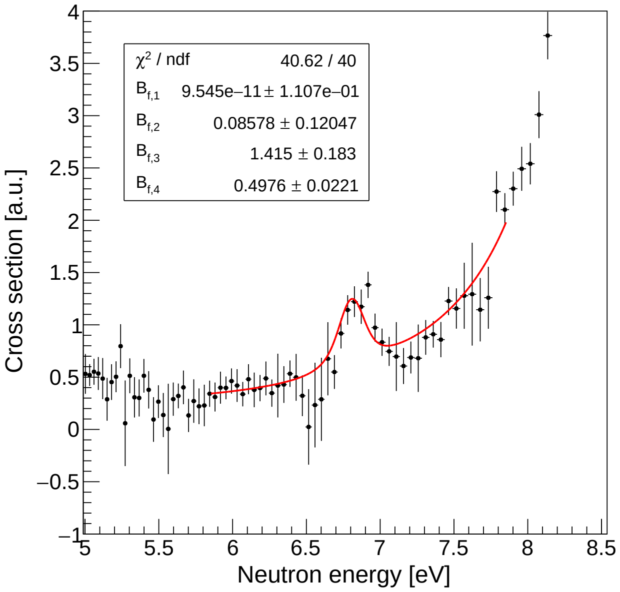

FIGURE 4.15: Relative values of the transition ratio for each resonance. The solid line represents the convoluted Breit–Wigner function.

4.8 Determination of transition ratio

To obtain the value of ϕ, the conditions between the experimental data analysis and theoretical calculation must correspond. Because the event selection in this study was applied for the 5960 keV peak, which was the mixed state of 5971 keV and 5956 keV, the transition probability of the compound nucleus to these excited states for each resonance, which is called the transition ratio, was included in the theoretical calculations. Figure 4.15 is a fitting result with the convoluted Breit–Wigner function explained in the previous section to a neutron energy spectrum obtained by summing the neutron energy spectra at each detection angle obtained in Sec. 4.6. The solid line represents the convoluted Breit–Wigner function, where the free parameters are the heights of the resonances, i.e., the transition ratios. The resonance parameters and temperature were fixed at the values listed in Tab. 4.3 and room temperature, respectively, and only the heights of each resonance peak were set as the free parameters. The transition ratios of the 5971 keV and 5956 keV mixed states for each resonance were

$$B_{f,1} : B_{f,2} : B_{f,3} : B_{f,4} = 0.00 \pm 0.11 : 0.09 \pm 0.12 : 1.42 \pm 0.18 : 0.50 \pm 0.02.$$

Here, the subscript B_f denotes the index r of each resonance in Tab. 4.3. The 5960 keV γ-ray peak was dominated by a p-wave resonance at 6.85 eV and its nearest s-wave resonance at 9.07 eV. These transition ratio values were expressed in arbitrary units and only the relative value for each resonance was essential.

By applying them to the theoretical calculations in Chap. 2, the coefficients a_0, a_{1x}, a_{1y}, a_{3xy}, and a_{3yy} in ^{115}In(n, γ) were obtained for the mixed states of 5971 keV and 5956 keV (Fig. 4.16). The solid line represent a_0, the dotted lines represent a_{1x} (left figure) and a_{3xy} (right figure), and the dashed lines represent a_{1y} (left figure) and a_{3yy}

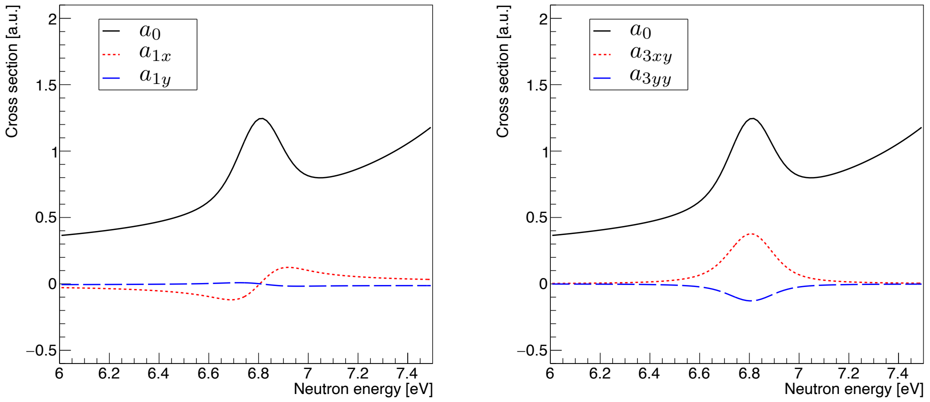

FIGURE 4.16: Coefficients a_0, a_{1x}, a_{1y}, a_{3xy} and a_{3yy} in the $^{115}\mathrm{In(n,\gamma)}$ reaction to the $F = 4$ final state using the resonance parameters in Tab. 4.3 and transition ratios.

(right figure). In the next section, the asymmetries from these curves are obtained through theoretical calculations and compared with the experimental asymmetries described in Sec. 4.6 to obtain ϕ.

4.9 Determination of ϕ and $\kappa(J)$

4.9.1 Theoretical calculation considering the transition ratios

The respective coefficients of the $\cos\theta_\gamma$ dependence of asymmetry can be redefined using Eqs. 2.3 and 2.6 as follows:

$$\begin{aligned} A_1 &= \frac{\int_{\mathrm{L}} a_1 dE_{\mathrm{n}} - \int_{\mathrm{H}} a_1 dE_{\mathrm{n}}}{\int_{\mathrm{L}} a_0 dE_{\mathrm{n}} + \int_{\mathrm{H}} a_0 dE_{\mathrm{n}}} x + \frac{\int_{\mathrm{L}} a_1 dE_{\mathrm{n}} - \int_{\mathrm{H}} a_1 dE_{\mathrm{n}}}{\int_{\mathrm{L}} a_0 dE_{\mathrm{n}} + \int_{\mathrm{H}} a_0 dE_{\mathrm{n}}} y \\ &= A_{1x} x + A_{1y} y, \end{aligned} \tag{4.9}$$

$$\begin{aligned} A_3 &= \frac{\int_{\mathrm{L}} a_1 dE_{\mathrm{n}} - \int_{\mathrm{H}} a_3 dE_{\mathrm{n}}}{\int_{\mathrm{L}} a_0 dE_{\mathrm{n}} + \int_{\mathrm{H}} a_0 dE_{\mathrm{n}}} xy + \frac{\int_{\mathrm{L}} a_3 dE_{\mathrm{n}} - \int_{\mathrm{H}} a_1 dE_{\mathrm{n}}}{\int_{\mathrm{L}} a_0 dE_{\mathrm{n}} + \int_{\mathrm{H}} a_0 dE_{\mathrm{n}}} y^2 \\ &= A_{3xy} xy + A_{3yy} y^2. \end{aligned} \tag{4.10}$$

The coefficients A_0, A_{1x}, A_{1y}, A_{3xy}, and A_{3yy} are defined as

$$\begin{aligned} A_0 &= -0.068, \\ A_{1x} &= -0.308, \\ A_{1y} &= 0.283, \\ A_{3xy} &= -0.111, \\ A_{3yy} &= 0.038, \end{aligned} \tag{4.11}$$

by integrating the p-wave resonance region as shown in Fig. 4.16, where the integral region is the same as that described in Sec. 4.6. The value of A_0 obtained from the theoretical calculation is consistent with the fitting result shown in Fig. 4.12, implying that the calculation is reasonable.

4.9.2 Determination of ϕ and $\kappa(J)$

By comparing the $\cos\theta_\gamma$-dependent term between the experimental results (Fig. 4.12) and theoretical calculations (Eq. 4.11), the following functions are obtained:

$$\begin{aligned} A_1 &= A_{1x}x + A_{1y}y \\ -0.174 \pm 0.125 &= -0.308x + 0.283y, \end{aligned} \tag{4.12}$$

$$\begin{aligned} A_3 &= A_{3xy}xy + A_{3yy}y^2 \\ -1.070 \pm 1.240 &= -0.111xy + 0.038y^2. \end{aligned} \tag{4.13}$$

The value of ϕ can be obtained by calculating the intersection of Eqs. 4.12 and 4.13 with $x^2 + y^2 = 1$. Figure 4.17 shows Eq. 4.12 and $x^2 + y^2 = 1$ in the xy-plane; thus, the obtained x and ϕ values with statistical errors of 1σ are

$$\begin{aligned} x &= 0.93^{+0.07}_{-0.17} \text{ or } x = -0.31^{+0.36}_{-0.28}, \\ \phi &= 23.0^{+17.8}_{-21.0}{}^{\circ} \text{ or } \phi = 252.0^{+21.0}_{-17.8}{}^{\circ}. \end{aligned} \tag{4.14}$$

Systematic errors are studied for the region where the asymmetries are calculated. The definition of the integration region has already been shown in Fig. 4.11. The integrations are performed both in the upper and lower intervals from the resonance energy E_p. Here, the interval of the integrations corresponds to $2.5\Gamma_\mathrm{p}$ using the Γ_p obtained in Sec. 4.7. First, a consideration related to an uncertainty of E_p is discussed below. The $E_\mathrm{p} = 6.85$ eV used in this study is the value given in Ref. [47]. The uncertainty of the neutron energies in ANNRI, which has been discussed in Ref. [69], is $\sim 0.5\%$ near 6.85 eV, thus $6.85 \times 0.005 \sim 0.034$ eV is given. When E_p is changed in the range of $E_\mathrm{p} \pm 0.034$ eV, the variation of the median value of ϕ is negligible, being one order of magnitude smaller than the statistical error. Second, an consideration related to the integration range is described below. When the integration range is changed in the range of $2.5\Gamma_\mathrm{p} \pm 0.5\Gamma_\mathrm{p}$, there is a significant variation in the center value of ϕ. Therefore, the variations in the center value is recorded as a systematic error and the ϕ values were obtained as

$$\phi = 23.0^{+17.8+4.7}_{-21.0-6.9}{}^{\circ} \text{ or } \phi = 252.0^{+21.0+6.9}_{-17.8-4.5}{}^{\circ}.$$

The solid line and shaded area represent the central value and 1σ statistical error, respectively. Here, these values are obtained using A_1 only, because the statistical error of A_3 does not permit a restriction on the unit circle. The values of $|\kappa(J)|$ are obtained as

$$\kappa(J) = 1.10^{+0.29+0.07}_{-0.26-0.09} \text{ or } \kappa(J) > 1.66. \tag{4.15}$$

by substituting the ϕ values in Eq. 4.14 into Eq. 1.4 (Fig. 4.18). The solid line represents the $\kappa(J)$ curve of Eq. 1.4. The dotted lines represent the central values of ϕ. The shaded areas represent the limitations of the ϕ values with the 1σ statistical error. The numerical value of ϕ that indicates $|\kappa(J)| = 0$, which is closest to the central value of ϕ obtained in this study, is $\phi = 309^\circ$ from Fig. 4.18. Therefore, the value of $|\kappa(J)|$ obtained in this study deviates by 2.0σ from $|\kappa(J)| = 0$.

Finally, by substituting the x values in Eq. 4.14 and the resonance parameters of the s-wave resonances that have the same J value as the p-wave resonance in Tab. 4.3

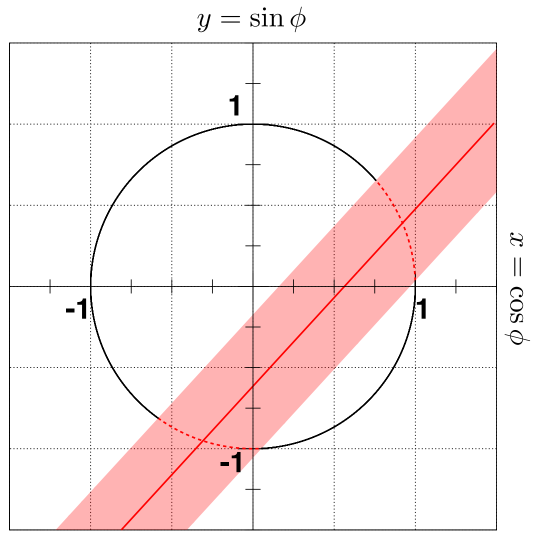

FIGURE 4.17: Visualization of ϕ on the xy-plane. The solid line and shaded area represent the central value and 1σ statistical error, respectively.

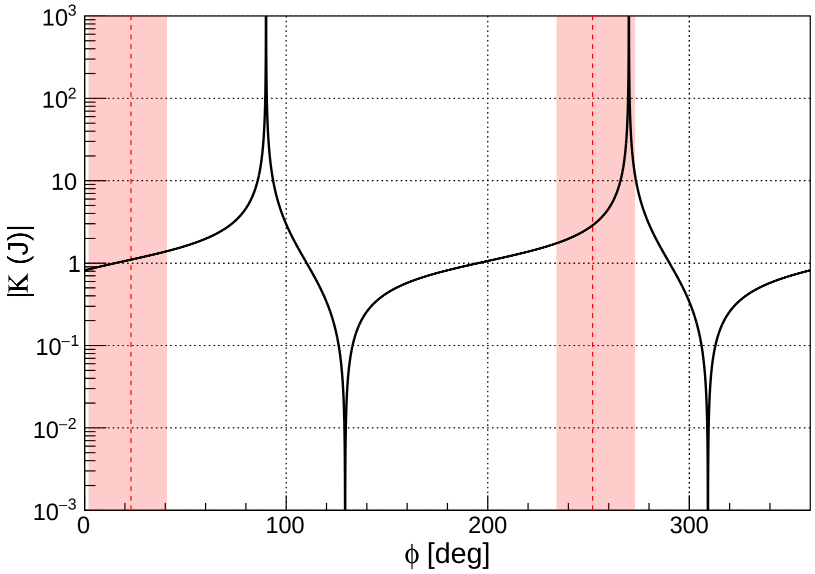

FIGURE 4.18: Limitation area of $|\kappa(J)|$ as a function of ϕ. The solid line represents the $\kappa(J)$ curve of Eq. 1.4. The dotted lines represent the central values of ϕ. The shaded areas represent the limitations of the ϕ values with the 1σ statistical error.

into Eq. 1.1, the weak matrix elements W are calculated to be

$$W = -3.2^{+0.3}_{-0.7} \text{ meV or } W = 9.6^{+4.5}_{-66.3} \text{ meV}. \tag{4.16}$$

Using two values of each ϕ and W obtained in this chapter, the estimation of target thicknesses and estimation of the experimental sensitivities of T violation search using an optimization indium target are discussed in Chap. 6. The ϕ, $\kappa(J)$, and W values are uniquely determined by measuring the other coefficient terms described in Chap. 2 using a polarized neutron beam.

Chapter 5

Development of the neutron spin filter for epithermal neutrons

In this chapter, the development of a neutron spin filter, a device that realizes the spin polarization of epithermal neutrons, is described. In this study, a proton-polarized neutron spin filter was used as the neutron spin filter. The principle of neutron polarization by a proton spin filter is explained in Sec. 5.1. In Sec. 5.2, some methods of proton polarization are introduced, and the dynamic nuclear polarization using photo-excited triplet electrons adopted in this study is explained. The design of the neutron spin filter using the polarization method and the developed spin filter is described in Sec. 5.3 and5.4. In Sec. 5.5, the experimental method and results of the performance evaluation of the developed spin filter are explained.

5.1 Polarization principle of epithermal neutrons using the neutron spin filter

The proton spin filter is the only neutron spin polarization device available in the wide energy range of epithermal neutrons, as mentioned in Sec. 1.3.2. The principle of neutron polarization using the polarized proton spin filter relies on the fact that the singlet-state cross-section of neutron–proton scattering is 20 times larger than that of the triplet-state cross-section [56, 76]. The total cross-section for neutron–proton scattering is conventionally defined as the sum of the spin-dependent and spin-independent cross-sections (σ_p and σ_0) [58, 77, 78]

$$\sigma = \sigma_0 + \sigma_\mathrm{p} P(\boldsymbol{S} \cdot \boldsymbol{I}),$$

where P is the proton polarization and $\boldsymbol{S}$ and $\boldsymbol{I}$ are the unit vectors of the incident neutron and proton spins, respectively. Thus, neutrons polarized antiparallel to protons interact much more strongly than neutrons polarized parallel to protons. The value of σ_p in the epithermal region is almost constant and approximate to the value of $-\sigma_0$ [56].

The neutron transmissions of polarized and unpolarized proton spin filters (T_pol and T_unpol) are expressed as

$$\begin{aligned} T_\mathrm{unpol} &= \exp(-n\sigma_0 d), \\ T_\mathrm{pol} &= \exp(-n\sigma_0 d)\cosh\left(n\sigma_\mathrm{p} P d\right), \\ \frac{T_\mathrm{pol}}{T_\mathrm{unpol}} &= \cosh\left(n\sigma_\mathrm{p} P d\right), \end{aligned}$$

where n is the proton density, d is the filter thickness, and σ_0 is the cross-section of neutron scattering with the unpolarized proton. The neutron polarization P_n after passing through the spin filter is expressed as [76]

$$P_\mathrm{n} = \tanh\left(n\sigma_\mathrm{p} P d\right).$$

5.2 Polarization method of protons

5.2.1 Brute force polarization and dynamic nuclear polarization

The simplest technique to polarize the spin of a particle is brute force polarization. The central notion of brute force polarization is that as the temperature is reduced and the field is increased, the equilibrium nuclear polarization increases, according to the Boltzmann distribution. The polarization of a spin $\boldsymbol{I}$ particle in the brute force method is calculated as

$$\begin{aligned} P &= \frac{1}{I}\frac{\sum_{i=I}^{-I} iN_i}{\sum_{i=I}^{-I} N_i}, \\ N_i &= \exp\left(-\frac{i\hbar\gamma B_0}{k_B T}\right), \end{aligned} \tag{5.1}$$

where B_0 is the magnetic field, T is the temperature, γ is the gyromagnetic ratio, k_B is the Boltzmann constant, and $\hbar$ is the Planck constant. In particular, for spin $I = 1/2$, it can be expressed as

$$P = \tanh\frac{\gamma\hbar B_0}{2k_B T}.$$

Figure 5.1 depicts the polarization for several particles based on Eq. 5.1, with B_0/T in the horizontal axis. The filled circle is for electrons, the open circle for protons, the filled square for ^{117}Sn, the open square for ^{115}In, and the filled triangle for ^{139}La. For brute force polarization, a magnetic field of 10 T and a temperature of 100 mK are required to obtain a proton polarization of 10%.

The theory of dynamic nuclear polarization (DNP) as a method to significantly improve polarization was proposed by A. W. Overhauser [79] and experimentally proven by T. R. Carver and C. P. Slichter [80] in 1953. DNP is a method of transferring the polarized state of the electron spin to the nuclear spin via microwave irradiation. As the gyromagnetic ratio of electron spins is 660 times greater than that of proton spins, the polarization of electron spins at thermal equilibrium is 660 times greater than that of proton spins. Figure 5.1 shows that the electron reaches a polarization of almost 100% at B_0/T, which is significantly smaller than that of the proton. Therefore, if DNP is performed using thermally equilibrated electron spins as the polarization source, the nuclear spin polarization can be improved up to 660 times. Today, proton polarizations of over 90% are obtained using DNP at temperatures of the magnetic field of $O(10^0)$ T and a temperature of $O(10^0)$ K [81–84].

5.2.2 Dynamic nuclear polarization using photo-excited triplet electron spins

The DNP method using non-equilibrium photoexcited triplet electron spins as the polarization source instead of electron spins in the thermal equilibrium state is called triplet DNP. Because the distribution of populations of the photoexcited triplet electron spins is highly polarized independent of the temperature and magnetic field,

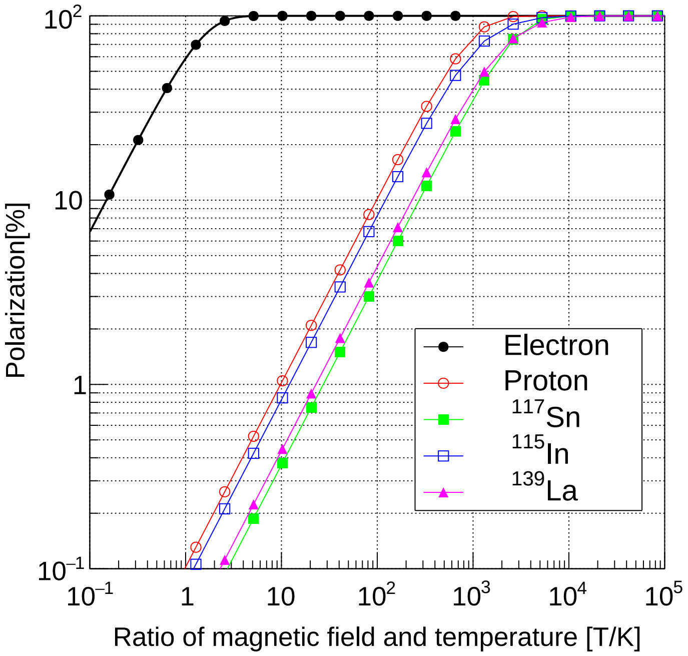

FIGURE 5.1: Polarizations of spin $\boldsymbol{I}$ particles as a function of the ratio of the magnetic field and temperature. The filled circle represents electrons, the open circle represents protons, the filled square represents ^{117}Sn, the open square represents ^{115}In, and the filled triangle represents ^{139}La.

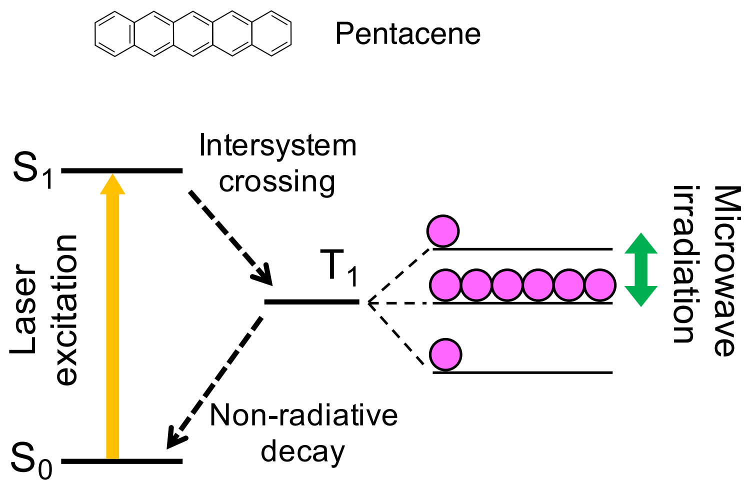

FIGURE 5.2: Simplified energy diagram of pentacene showing a pathway during triplet DNP [86].

triplet DNP can be performed at higher temperatures and lower magnetic fields than conventional DNP.

The triplet DNP polarization procedure, explained in Ref. [85], begins with laser irradiation to generate electron polarization. Figure 5.2 shows the energy diagram of deuterated pentacene. Light irradiation with a wavelength of 589 nm induces a transition from the ground singlet state S_0 to its excited triplet state T_1 via its excited singlet state S_1. The states of pentacene electrons are gradually attracted to the T_1 states using laser irradiation because the transition probability due to non-radiative decay is smaller than the transition probability from the S_1 to T_1 states owing to intersystem crossing. This transition probability determines the population of triplet states. For deuterated pentacene doped with naphthalene single crystals, the populations of electrons in the triplet state are 0.045, 0.910, and 0.045, which correspond to an electronic polarization of 0.906 when the long axis of the molecule is aligned parallel to the magnetic field B_0 [85, 87]. The polarization of the triplet electron in deuterated pentacene is transferred to the proton spin in naphthalene [88] by matching the Rabi frequency of the electron spin to the Larmor frequency of the proton spin (Hartmann–Hahn condition [89]). A magnetic field sweep and microwave irradiation are simultaneously applied. The inhomogeneously broadened electron spin packets are swept adiabatically. The polarization exchange of electron and proton spins owing to this process is known as the integrated solid effect (ISE) [90, 91]. By repeating the ISE cycle, proton polarization can be accumulated until the build-up and proton spin-lattice relaxation are balanced. In a recent study of triplet DNP, a proton polarization of 0.34 was also obtained at room temperature and 0.40 T [92]. In addition, this method has been applied not only in accelerator science but also in chemical and medical fields [93–95].

In this thesis, the proton spin filter based on proton polarization by triplet DNP is called a triplet-DNP spin filter. Studies on triplet-DNP spin filters for cold neutrons have been conducted at the Paul Scherrer Institute (PSI) in Switzerland [85, 96–99]. They achieved a proton polarization of 0.80 at 25 K and in 0.36 T, using a single crystal of naphthalene doped with deuterated pentacene with a size of $5 \times 5 \times 5$ mm^3.

5.3 Optimum thickness of the triplet-DNP spin filter for the epithermal neutrons

The triplet-DNP spin filter utilizes the polarization of the hydrogen nuclei in a naphthalene crystal. Considering that the main component of the triplet-DNP spin filter is naphthalene, the neutron transmissions T_{unpol} and T_{pol} and neutron polarization P_{n} are redefined as

$$\begin{aligned} T_{\text{unpol}} &= \exp\left\{-\left(n\sigma_0 + n_{\text{C}}\sigma_{\text{C}}\right)d\right\}, \\ T_{\text{pol}} &= \exp\left\{-\left(n\sigma_0 + n_{\text{C}}\sigma_{\text{C}}\right)d\right\}\cosh\left(n\sigma_{\text{p}}Pd\right), \\ \frac{T_{\text{pol}}}{T_{\text{unpol}}} &= \cosh\left(n\sigma_{\text{p}}Pd\right), \\ P_{\text{n}} &= \tanh\left(n\sigma_{\text{p}}Pd\right). \end{aligned} \tag{5.2}$$

where n_{C} is the carbon density and σ_{C} is the neutron scattering cross-section with carbon nuclei.

As the thickness of the neutron spin filter increases, the neutron transmission rate decreases, but the neutron polarization rate increases. The FOM is discussed as a statistically relevant factor in the optimization of the spin-filter performance [59] and is defined as

$$\text{FOM} = P_{\text{n}}^2 T_{\text{pol}}. \tag{5.3}$$

Figure 5.3 shows the neutron polarization, neutron transmission (top figure), and FOM (bottom figure) for the $P = 0.1$ (dotted line), $P = 0.3$ (solid line) and $P = 0.5$ (dashed line) scenarios as a function of the thickness d. Here, $n_{\text{p}} = 4.29 \times 10^{22}$ /cm^3, $n_{\text{C}} = 5.36 \times 10^{22}$ /cm^3, $\sigma_0 = 20.5$ barn, $\sigma_{\text{p}} = 16.7$ barn, and $\sigma_{\text{C}} = 4.74$ barn were used. The optimal thickness of the triplet-DNP spin filter is the thickness d at which the FOM is a maximum, which is approximately 15 mm thick. This value is almost independent of the proton polarization and neutron energy. This is why the proton spin filter is the only neutron polarization method available today for a wide energy range of epithermal neutrons. For the ^{3}He spin filter, the neutron transmission, neutron polarization, and FOM are defined by similar equations. The difference from the proton scenario is that the neutron-^{3}He cross-section is dominated by the neutron capture reaction. Therefore, the neutron transmission, neutron polarization, and FOM of the ^{3}He spin filter decrease with increasing neutron energy.

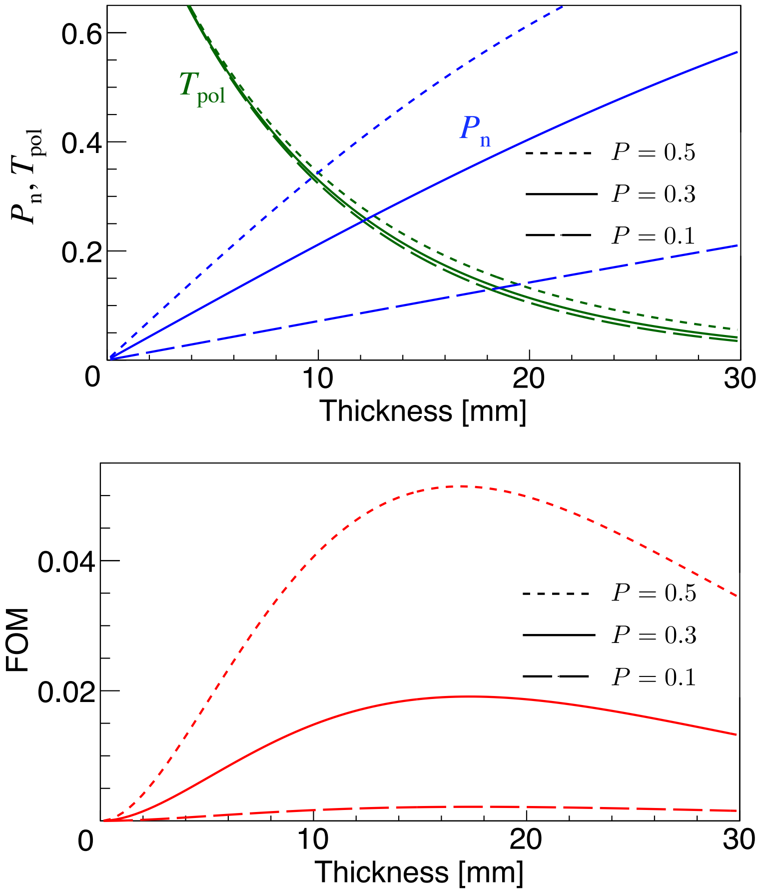

FIGURE 5.3: Performance of the polarized proton spin filter with proton polarization $P = 0.1$ (dotted line), $P = 0.3$ (solid line), and $P = 0.5$ (dashed line) for epithermal neutrons [86]. Neutron polarization (P_n) and neutron transmission (T_n) as functions of the spin-filter thickness d (top). Figure of merit (FOM) as a function of the spin-filter thickness d (bottom).

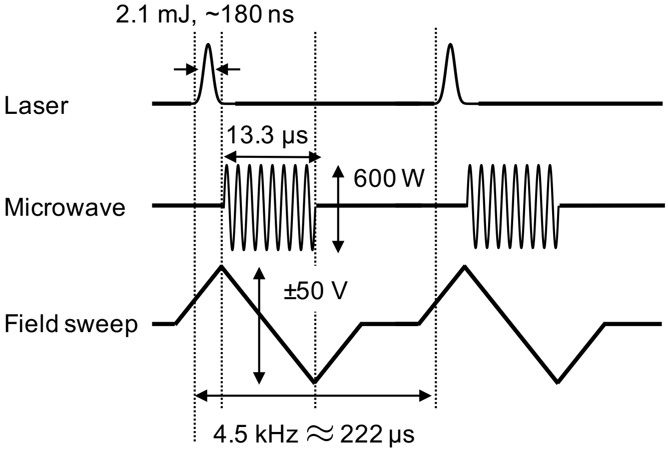

FIGURE 5.4: Pulse sequence of triplet DNP [86]. One cycle is composed of a laser pulse for generating polarized triplet electrons, microwave pulse, and field sweep for polarization transfer.

5.4 Structure of the triplet-DNP system

The polarization system for the triplet-DNP spin filter was previously reported in Ref. [86]. Triplet DNP was performed at 0.35 T using a C-type electromagnet with a gap of 100 mm and pole diameter of 220 mm. The resonance frequencies of electrons and protons were 9.2 GHz and 15.0 MHz (high-field transition), respectively. Figure 5.4 shows the ISE cycle. The electron polarization created using laser irradiation was adiabatically transferred to protons via the injection of microwaves and a swept magnetic field. A diode-pumped solid-state (DPSS) laser (CNI, HPL-589-Q) was used to excite the pentacene electrons. The wavelength, pulse width, pulse energy, and repetition rate were 589 nm, $\sim$ 180 ns, 2.1 mJ, and 4.5 kHz, respectively. The laser pulses were sampled using a photodiode and converted to transistor–transistor logic (TTL) levels. This signal was used to trigger subsequent microwave and electric-field sweeps. The microwaves were amplified to 600 W using a pulsed traveling wave tube amplifier (IFI, PT188-1KW, max duty 6%) and swept with a width of 13.3 μs and an electric field with a voltage of ±50 V.

The triplet DNP system was then placed in a double-walled chamber (Fig. 5.5(a)). The inner chamber was cooled to 90 K using cooled nitrogen gas, and the outer chamber was maintained at 20 Pa to prevent frosting. The chambers were equipped with optical windows. The laser was introduced from three locations: one from upstream and two from downstream. A dielectric-coated silicon substrate mirror with a thickness of 1 mm was used at the upstream side to minimize the neutron transmission loss. The inside of the chamber is shown in Fig. 5.5(b). Naphthalene crystals doped with 0.003 mol% deuterated pentacene were placed at the center of the electromagnet. The crystal was cut to a size of $\phi 15 \times 4$ mm^3 because the laser power was insufficient to polarize a 15 mm-thick filter. This was mounted in a Teflon holder; a TE011 cylindrical cavity equipped with field sweep and split coils for NMR was used. The resonance frequency of the TE011 mode [100] is

$$f = \frac{c\sqrt{1+\left(\frac{2l}{1.64a}\right)^2}}{2l\sqrt{\mu_r \epsilon_r}},$$

where c, μ_r, and ϵ_r are the speed of light in a vacuum, magnetic permeability, and relative permittivity, respectively. The parameters a and l are the diameter and length of the cylindrical cavity, and they were 21 mm and 25 mm, respectively. A coaxial microwave transmission line was adapted to the waveguide and coupled to the cavity through an iris. The crystal could be rotated using a crystal rotation gear and its alignment could be precisely adjusted. Polarized proton signals were monitored using an OPENCORE nuclear magnetic resonance (NMR) spectrometer [101, 102].

5.5 Performance evaluation at RANS

5.5.1 Experimental setup of performance evaluation

The performance evaluation experiment of the triplet DNP spin filter was performed at the RIKEN Accelerator-Driven Compact Neutron Source (RANS) in Wako, Saitama, Japan. RANS has been in operation since 2013 and has been applied to develop nondestructive testing methods for infrastructure and industrial products, such as concrete and steel [103–107]. RANS consists of a linear accelerator and a target station (Fig. 5.6(a)). Protons were accelerated to 7 MeV in a linear accelerator and injected into a Be target [103]. The $^9\mathrm{Be(p,n)}$ reaction produced neutrons with a maximum energy of 5 MeV. The neutrons were moderated using a 40 mm-thick polyethylene moderator and were extracted from the target station. The energy spectrum at 5 m from the Be target was presented in Ref. [108]. The Be target and moderator were surrounded by carbon blocks as neutron reflectors, boron polyethylene (BPE) powder in an aluminum box as neutron and gamma shielding, and lead blocks in steel enclosures.

The experimental setup is shown in Fig. 5.6(b). A BPE collimator (hole diameter of 15 mm^2) was installed at the exit of the neutron beam at the RANS target station. The neutron shielding to reduce the background signal consisted of BPE blocks and boron rubber sheets. A resistive photomultiplier tube (RPMT) detector consisting of a ZnS (Li) scintillator and a position-sensitive photomultiplier tube [109] was used for the two-dimensional position and TOF measurements. The detector was set in an aluminum box containing BPE powder to shield the background neutrons and was placed 0.55 m behind the naphthalene crystal. At this position, the stray field from the electromagnet was less than 10 G and did not affect the photomultiplier tube of the detector. The spatial resolution and neutron beam intensity are functions of the distance from the neutron source to the spin filter. The longer the distance, the better the spatial resolution but the smaller the neutron beam intensity. The distance was set to 4.31 m, the spatial resolution in the full energy range was approximately 2 mm, and the neutron intensity was 8.3×10^5 count/h^{-1}.

5.5.2 Neutron transmission measurements

The structure of the neutron pulse determines the maximum and minimum available neutron energy. The shorter the pulse width, the larger the maximum available neutron energy but the smaller the neutron beam intensity. In this experiment, the pulse width and repetition rate were set as 60 μs and 105 Hz, respectively. Considering this repetition rate and the distance from the Be target to the detector, the minimum available neutron energy was 1 meV. To calculate neutron transmission, we also performed measurements without a target (blank measurements). The measurements were also performed using a boron rubber target (33 mm thick) instead of a naphthalene crystal (background measurement) to subtract accidental events, such as scattering between

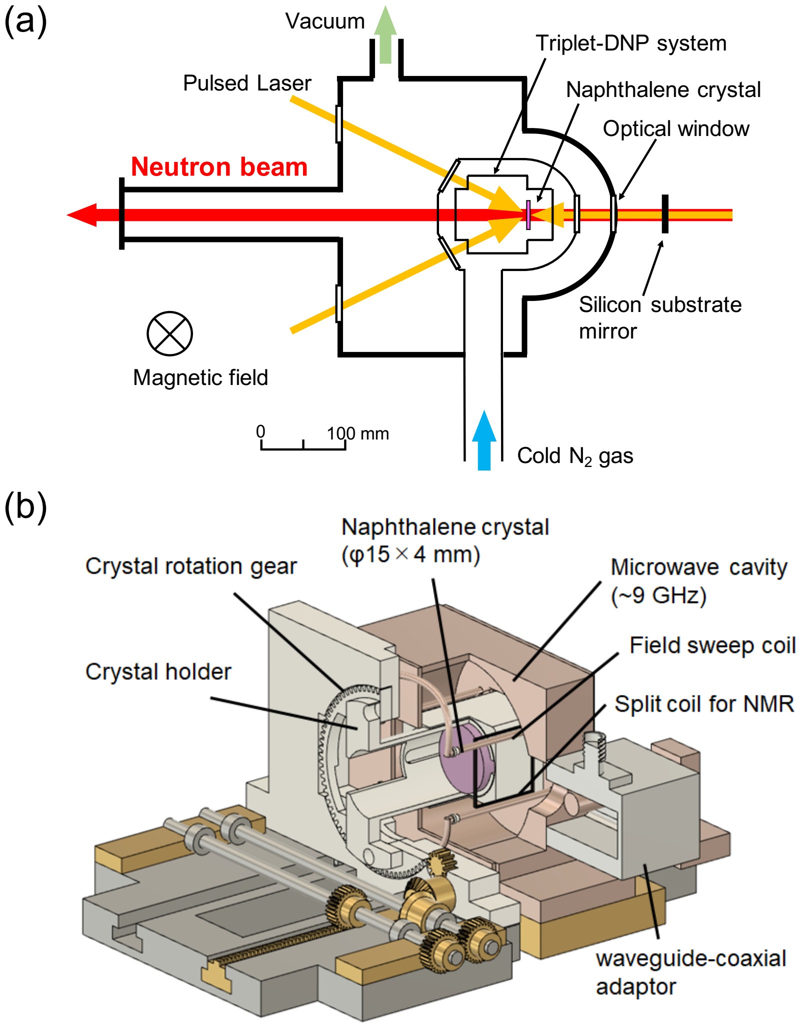

FIGURE 5.5: Experimental setup of triplet DNP [86]. (a) A double-walled chamber was placed in an electromagnet. The inner chamber was cooled to 90 K, and the outer chamber was maintained at 20 Pa. The lasers were irradiated from three lines. (b) Schematic of the home-built TE011 cylindrical cavity equipped with a field-sweep coil and split coil for NMR. The naphthalene crystal could be rotated using a crystal rotation gear.

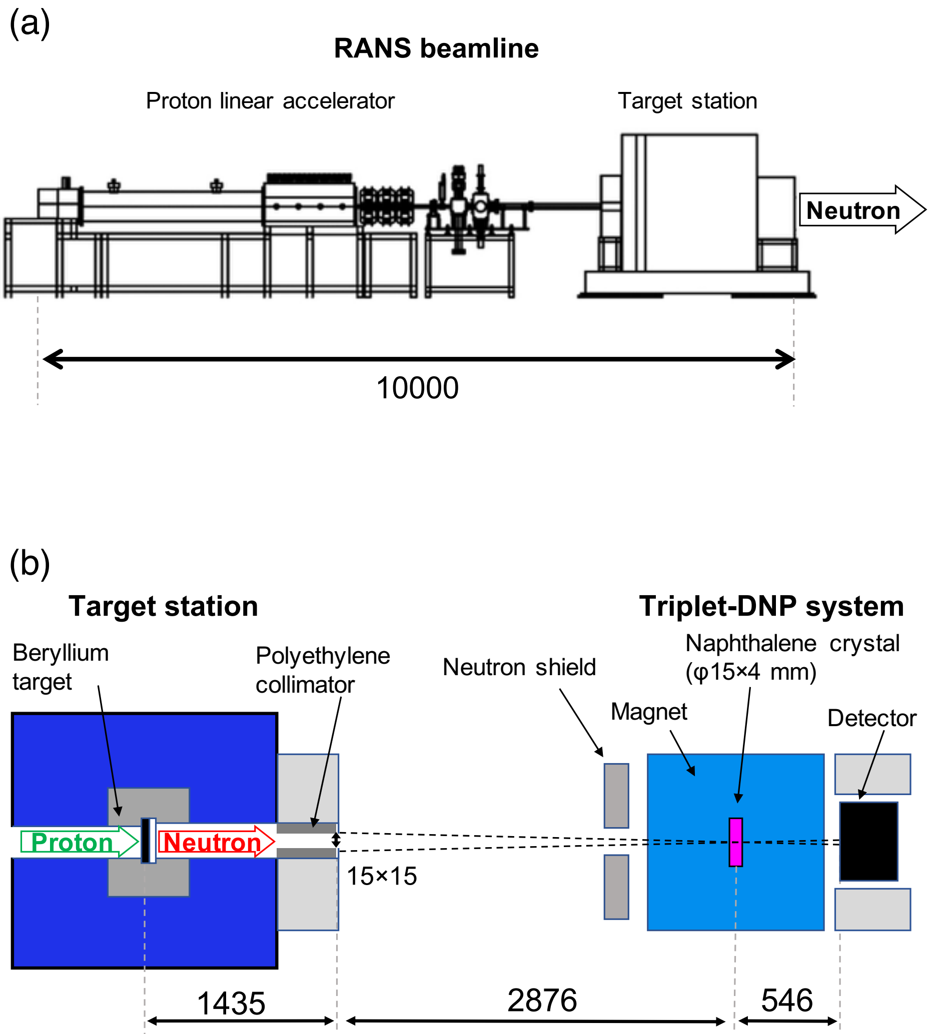

FIGURE 5.6: Experimental setup of the neutron transmission measurement at RANS [86]. (a) Side view of RANS. (b) Top view of setup for the neutron transmission experiment using RANS.

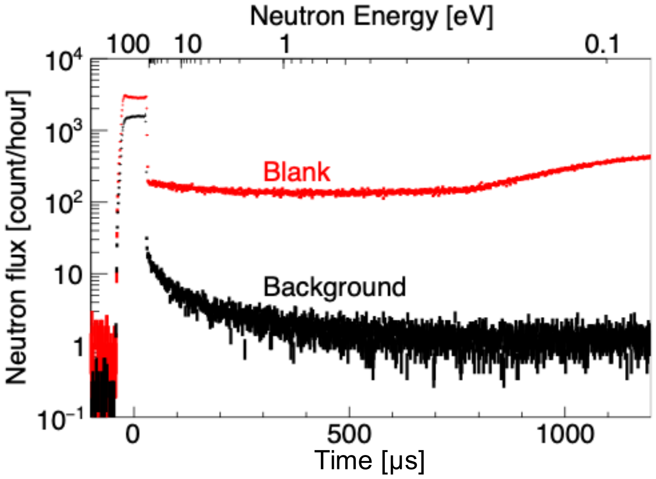

FIGURE 5.7: Neutron beam intensity of blank and background measurements in the epithermal region as a function of the TOF [86].

the microwave cavity and neutrons. The TOF spectra obtained from the blank and background measurements are shown in Fig. 5.7 for the epithermal neutron region. The figure shows that the neutron beam intensity of the background measurement was 10 to 10^2 lower than that of the corresponding blank measurement in all time regions of the TOF spectrum. The rectangular peak at approximately 0 μs is the structure of the neutron pulse caused by the proton beam pulse. Considering the pulse width and the distance from the Be target to the detector, the maximum available neutron energy was 10 eV. The neutron beam intensity was 1.7×10^5 count/h^{-1} in the range of 0.1 eV to 10 eV.

5.5.3 Monitoring proton polarization using nuclear magnetic resonance

The relative magnitude of proton polarization was monitored using NMR techniques. A rotating magnetic field of 15.0 MHz was injected using an NMR coil (Fig. 5.5), which caused proton spins to rotate by $\pi/2$. The proton spins rotated in the NMR coil, producing an induced electromotive force, and the signal was detected. Figure 5.8 shows the intensity of the NMR signal recorded during the beam time. The shaded area indicates the irradiation time of the neutron beam. The neutron beam was irradiated after the build-up of the proton polarization was completely saturated. The signal intensity did not decrease during the neutron irradiation. This implied that the damage to the crystal by neutron radiation was negligible. The protons were depolarized at approximately $T = 80$ h and this state was maintained. The depolarized state was realized by shifting the relative timing of the microwave and field sweep to the laser, instead of cutting off the polarization sequence (Fig. 5.4) to maintain the environment inside the inner chamber. The plot of the filled circles in Fig. 5.9 shows an expanded version of Fig. 5.8 for 0 h to 15 h. The build-up time of polarization using DNP was approximately 2.5 h. In offline measurements, the relaxation time during laser irradiation (open circles in Fig. 5.9) was 5.8 h.

The proton polarization is calculated as

$$P = \frac{T_B}{T_B'} P_e \left[1 - \exp\left(-\frac{t}{T_B}\right)\right],$$

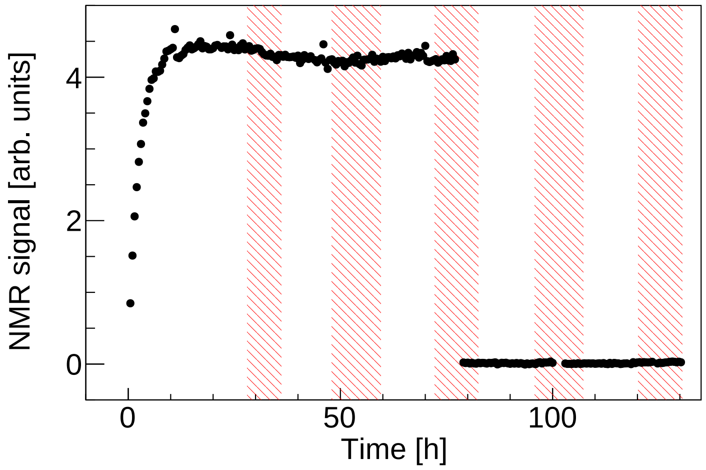

Figure 5.8: Relative intensity of the proton polarization during the beamtime [86]. The shaded areas correspond to neutron irradiation.

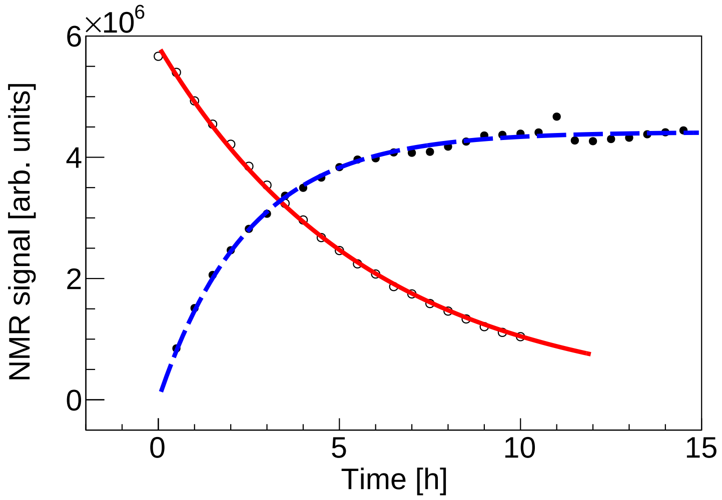

Figure 5.9: Relative intensity of the proton polarization [86]. Build-up of the NMR signal (filled circle) and relaxation of the NMR signal during laser irradiation (open circle).

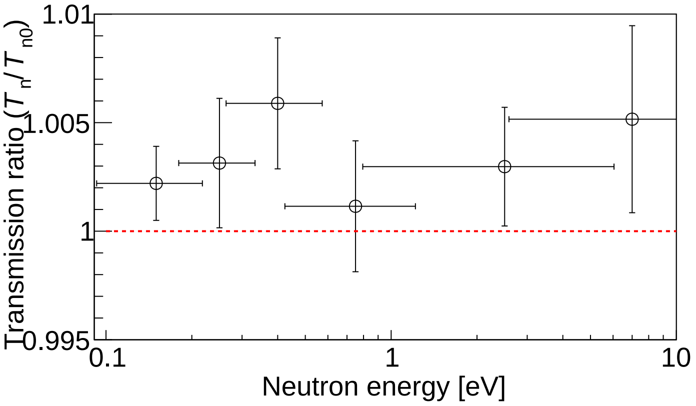

FIGURE 5.10: Ratio of neutron transmissions ($T_{\mathrm{pol}}/T_{\mathrm{unpol}}$) as a function of neutron energy [86].

$$\frac{1}{T_B} = \frac{1}{T'_B} + \frac{1}{T_1},$$

where P_e is the electron polarization, which is assumed to be 90% here, t is the measurement time, and T_B and T_1 are the buildup and relaxation times of the experimental values, respectively [110, 111]. Under the limit $t \to \infty$, using the build-up constant and relaxation time obtained from the NMR results, the proton polarization was calculated to be $P = \frac{T_B}{T'_B} P_e \sim 51.2\%$. However, an unpolarized area owing to the lack of laser power was not included in this estimation. The total proton polarization must be measured using neutrons.

5.5.4 Data analysis of the neutron transmission measurements

The absolute value of proton polarization was analyzed by comparing the number of neutrons passing through the triplet-DNP spin filter with and without proton polarization.

Figure 5.10 shows the ratio of TOF spectrum of naphthalene crystals with and without proton polarization, which was consistent with the ratio of neutron transmission $T_{\mathrm{pol}}/T_{\mathrm{unpol}}$. Here, TOF was converted to neutron energy E_{n} using an equation similar to Eq. C.1. The ratio of neutron transmission $T_{\mathrm{pol}}/T_{\mathrm{unpol}}$ as a function of neutron energy was reasonable according to Eq. 5.2, because it was greater than 1 in the entire region (Fig. 5.10).

The filled circles in Fig. 5.11(a) show $\sigma_{\mathrm{p}}P$ calculated by substituting the ratio of neutron transmission $T_{\mathrm{pol}}/T_{\mathrm{unpol}}$ (Fig. 5.10) into Eq. 5.2. The error in $\sigma_{\mathrm{p}}P$ included the statistical error of the transmitted neutrons and the filter thickness of 4.1 ± 0.1 mm. The absolute value of proton polarization was calculated by dividing $\sigma_{\mathrm{p}}P$ in Fig. 5.11(a) using the literature values of $\sigma_{\mathrm{p}}P$. The absolute value was only obtained in the energy region of 0.1 eV to 10 eV because the neutron—proton scattering cross-section was practically constant in the region higher than 0.1 eV, independent of the filter material and temperature [112–116]. Thus, the average value of $\sigma_{\mathrm{p}}P$ from 0.1 eV to 10 eV was applied from Ref. [56]. Consequently, an average proton polarization value of $P = 0.250 \pm 0.050$ was obtained. This value differed from that obtained in Sec. 5.5.3, which indicated that proton polarization inside the crystal is nonuniform. This is because the intensity of the laser and microwave irradiation differs between the surface and interior of the crystal. Figure 5.11(b) shows the neutron polarization P_n (open circle) and neutron transmission T_pol (filled circle). The neutron transmission T_pol (T_unpol) was obtained by dividing the TOF spectrum of the polarized (unpolarized) naphthalene measurement using the TOF spectrum of the blank measurement. By substituting the transmission T_unpol into Eq. 5.2, the cross-section of naphthalene was obtained (open circles in Fig. 5.11(a)). Here, the number density of the naphthalene was 5.36×10^{21} cm^{-3}. The FOM is shown in Fig. 5.11(c), which was calculated by substituting the obtained neutron transmission and neutron polarization values into Eq. 5.3. The average values between 0.1 eV to 10 eV were observed to be $P_\mathrm{n} = 0.076 \pm 0.015$, $T_\mathrm{pol} = 0.555 \pm 0.001$, and $\mathrm{FOM} = 0.0032 \pm 0.0009$. These results are expected to be similar up to keV because of the flatness of the neutron–proton scattering cross-section.

The practicality of the triplet-DNP spin filter in terms of its current performance can be discussed by comparing it with the performance of the ^{3}He spin filter in a previous study. Assuming the performance of the ^{3}He spin filter at a ^{3}He polarization of 0.785 and a ^{3}He density of 41.5 bar cm [117], the FOM of the triplet DNP spin filter exceeds that value at a neutron energy of 120 eV. Further improvements are required to achieve a higher FOM. In Chap. 6, methods to improve the FOM of the triplet-DNP spin filter are discussed.

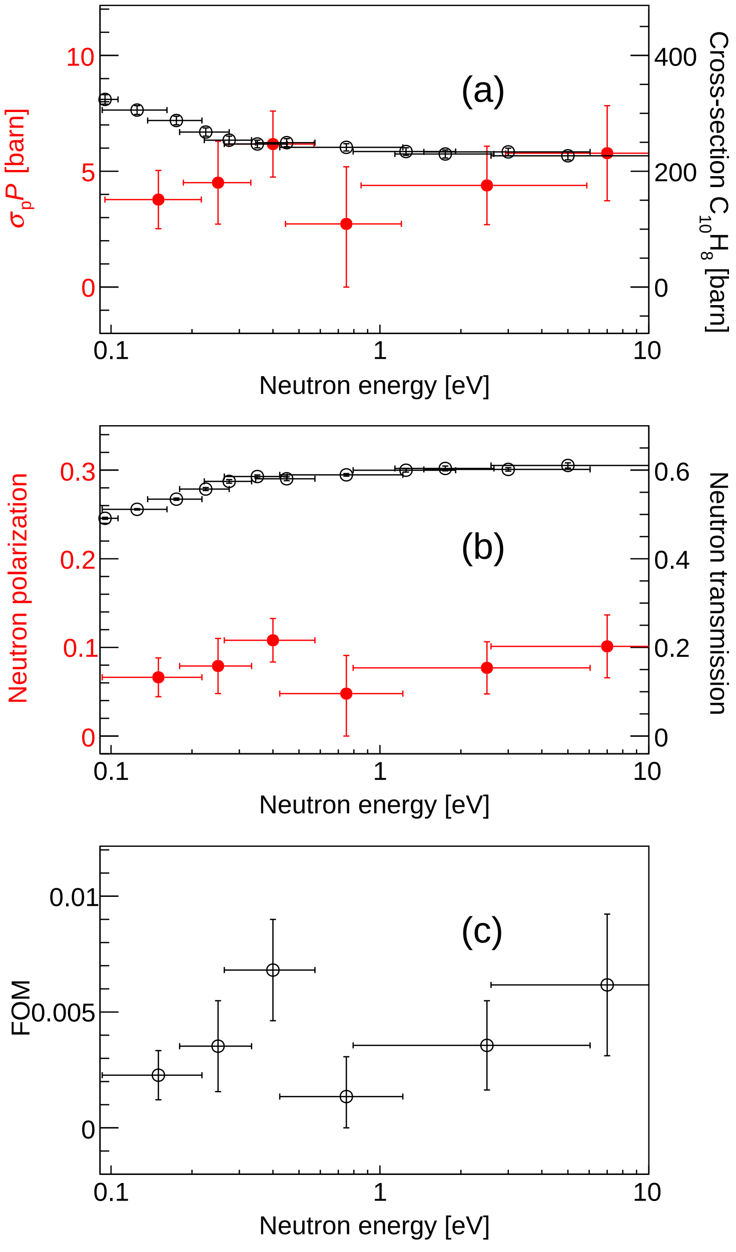

FIGURE 5.11: Results of the neutron transmission experiment at RANS [86]. (a) $\sigma_\mathrm{p}P$ (filled circle) and total cross-section of naphthalene (open circle). (b) Degree of neutron polarization (filled circles) and neutron transmission (white circles). (c) Figure of merit. These results were measured at 90 K and 0.35 T.

Chapter 6

Discussion

In Chap. 4, the mixing angle ϕ for ^{115}In was determined. In Chap. 5, the polarization of an epithermal neutron beam using a triplet-DNP spin filter was demonstrated. This chapter discusses future studies of epithermal neutron polarization and T violation search using indium. Section 6.1 suggests upgraded items to increase the FOM of the triplet-DNP spin filter. In Sec. 6.2, the sensitivities and measurement times of the T violation search using an indium target are estimated.

6.1 Upgrade to improve the figure of merit of the triplet-DNP spin filter

In this section, several methods to improve the FOM of the triplet-DNP spin filter are discussed. Figure 6.1 shows FOMs of the triplet-DNP spin filter as a function of the crystal thickness for several proton polarizations. The solid lines show the FOM curves for each proton polarization P, from top to bottom: $P = 0.9$, $P = 0.5$, and $P = 0.3$. Because the electron polarization of pentacene, the polarization source in triplet-DNP, is approximately 90% (as described in Sec. 5.2), the maximum achievable proton polarization is assumed to be 90%. Increasing the thickness of naphthalene crystals (dotted arrow in Fig. 6.1) and proton polarization (solid arrow in Fig. 6.1) is effective for improving the FOM of the triplet-DNP spin filter. The current FOM (dotted circle in Fig. 6.1) may still be improved up to 50 times. Several methods to realize each are presented in the following.

Two main methods are used to improve the proton polarization. The first is to lower the internal temperature of the chamber. According to previous research at PSI, applying DNP to a naphthalene crystal at a temperature of 25 K, which was achieved by spraying cooled helium gas to the crystal, increased the proton spin-lattice relaxation time to 800 h and proton polarization to 0.80 [98]. Another method is to increase the laser power. As mentioned in Sec. 5.4, the current laser power cannot reach the inside of the 15 mm-thick crystal. Since pentacene molecules are uniformly distributed inside the crystal, a distance that the laser passes through the crystal is proportional to the laser power. Assuming that the laser can reach the inside of the crystal at a current thickness of 4 mm, this can be achieved by increasing the laser power by a factor of at least four compared with the current power. When the laser intensity is increased, the problem of exhausting the heat generated inside the crystal by absorbing the laser occurs; thus, improvements to lower temperatures are necessary.

Two solutions are used to increase the thickness of a triplet-DNP spin filter. One is to stack several thin crystals to create a 15 mm thickness. This is the simplest method and is feasible even with the current laser intensity, but it requires a detailed structural design to adjust the laser incidence direction and rotation angle of the

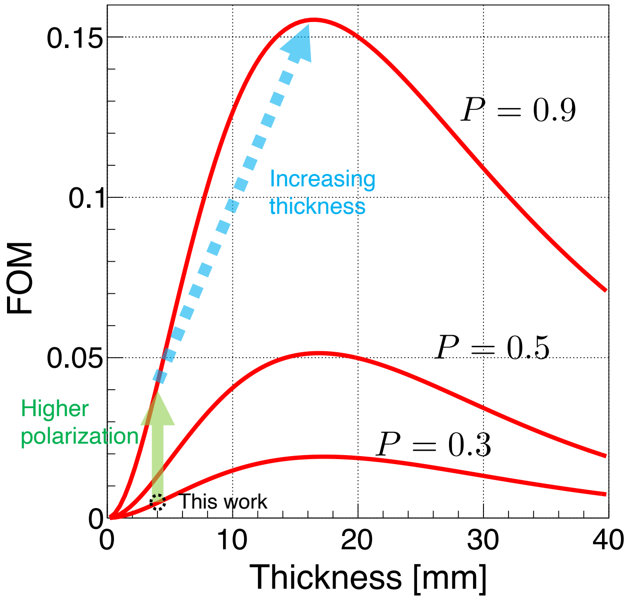

Figure 6.1: FOM of the triplet-DNP spin filter as a function of the crystal thickness for several proton polarizations. The solid lines show the FOM curves for each proton polarization P, from top to bottom: $P = 0.9$, $P = 0.5$, and $P = 0.3$.

crystal in the system shown in Fig. 5.5. The other is to use a 15 mm thick of single crystal. Here, it is essential to increase the laser power, as described above, for the laser to reach the interior of the crystal; hence, lower temperatures are also necessary.

Considering these factors, the most realistic improvement would be to use cooled helium gas to lower the temperature to 25 K and then layer thin filters to achieve an optimal thickness of 15 mm. Because 80% proton polarization was achieved in Ref. [98] at 25 K, the measurement time for T violation is estimated in the next section assuming a 50% proton polarization, which is reasonably achievable.

6.2 Estimation of the sensitivity for the T violation search

6.2.1 Estimation of the upper limit of W_T/W

The sensitivity of the T violation search with ^{115}In can be estimated using Eq. 1.3. The upper limit of the ratio of the T-violating matrix element to the P-violating matrix element in the nucleon–nucleon interaction of the compound W_T/W can be estimated using the upper limit of the current EDM search. The ratio of the T-odd P-odd cross-section to the P-odd cross-section in the compound nuclear reaction, $\Delta\sigma_\mathrm{T}/\Delta\sigma_\mathrm{P}$, is calculated using the meson-exchange model of the effective field theory (EFT) by Y. H. Song *et al.* [118]. Assuming that the ratio W_T/W is equal to $\Delta\sigma_\mathrm{T}/\Delta\sigma_\mathrm{P}$, the ratio is

$$\frac{W_\mathrm{T}}{W} = \frac{\Delta\sigma_\mathrm{T}}{\Delta\sigma_\mathrm{P}} \simeq (-0.47)\left(\frac{\bar{g}_\pi^{(0)}}{h_\pi^1} + (0.26)\frac{\bar{g}_\pi^{(1)}}{h_\pi^1}\right),$$

where $\bar{g}_\pi^{(0)}$ and $\bar{g}_\pi^{(1)}$ are the isoscalar and isovector time-reversal invariant meson–nucleon coupling constants, respectively, and h_π^1 is a P-violating meson exchange coupling constant. Here, superscript denotes the isospin change for the process. The upper limits of $\bar{g}_\pi^{(0)}$ and $\bar{g}_\pi^{(1)}$ were estimated from the nEDM [26] and ^{199}Hg-EDM search [119] as

$$\bar{g}_\pi^{(0)} < 1.6 \times 10^{-10} \text{ and } \bar{g}_\pi^{(1)} < 1.7 \times 10^{-13}.$$

The value of h_π^1 was obtained by measuring the P violation of the $\mathrm{n} + \mathrm{p} \to \mathrm{d} + \gamma$ reactions [120] as

$$h_\pi^1 = [2.6 \pm 1.2(\text{stat.}) \pm 0.2(\text{sys.})] \times 10^{-7}.$$

Using these values, the upper limit of the ratio W_T/W was estimated as

$$\left|\frac{W_\mathrm{T}}{W}\right| < 2.9 \times 10^{-4}. \tag{6.1}$$

6.2.2 Measurement method of the T violation using compound nucleus

As discussed in Sec. 1.3, a nonzero value of D implies the existence of a T violation. The D terms can be searched by measuring the analyzing power $\boldsymbol{A}$ and polarization $\boldsymbol{P}$, which are defined as

$$\boldsymbol{A} \equiv \frac{\mathrm{Tr}\left(\mathfrak{S}^\dagger \boldsymbol{\sigma} \mathfrak{S}\right)}{\mathrm{Tr}\left(\mathfrak{S}^\dagger \mathfrak{S}\right)} \text{ and } \boldsymbol{P} \equiv \frac{\mathrm{Tr}\left(\boldsymbol{\sigma} \mathfrak{S}^\dagger \mathfrak{S}\right)}{\mathrm{Tr}\left(\mathfrak{S}^\dagger \mathfrak{S}\right)},$$

where σ is the Pauli matrix, and the component with the same axis as the neutron spin direction is selected. Here, $\mathfrak{S}$ is the generalized neutron forward scattering amplitude for a target of finite thickness, as described in Appendix D. The ratio of the D' and C' in the scattering amplitude $\mathfrak{S}$, D'/C', implies Eq. 1.3. When the spin polarization of the target is parallel to the y-axis, as shown in Fig. 1.6, the following expressions for A and P are obtained for each direction of neutron spin polarization:

$$\begin{aligned}
A_x &= 4\left(\mathrm{Re}\, A^* D + \mathrm{Im}\, B^* C\right)/|A|^2 \text{ and } P_x = 4\left(\mathrm{Re}\, A^* D - \mathrm{Im}\, B^* C\right)/|A|^2,\\
A_y &= 4\left(\mathrm{Re}\, A^* B + \mathrm{Im}\, C^* D\right)/|A|^2 \text{ and } P_y = 4\left(\mathrm{Re}\, A^* B - \mathrm{Im}\, C^* D\right)/|A|^2,\\
A_z &= 4\left(\mathrm{Re}\, A^* C + \mathrm{Im}\, D^* B\right)/|A|^2 \text{ and } P_z = 4\left(\mathrm{Re}\, A^* C - \mathrm{Im}\, D^* B\right)/|A|^2.
\end{aligned}$$

Figure 6.2 shows the experimental setups for measuring analyzing power A and polarization P. The sum of A in the x-axis (A_x) and P in the x-axis (P_x) is the most sensitive observable, and is given by

$$A_x + P_x = \frac{8\,\mathrm{Re}\, A^* D}{|A|^2}. \tag{6.2}$$

6.2.3 Calculation of optimum thicknesses of an indium target

The thickness of the ^{115}In target is denoted by $8\,\mathrm{Re}\, A^* D$ in Eq. 6.2. Considering the polarization of the neutron beam and that of the target, Eq. 6.2 is rewritten as

$$A_x + P_x \quad = \quad P_\mathrm{n} P_\mathrm{t} \frac{8\,\mathrm{Re}\, A^* D}{|A|^2}, \tag{6.3}$$

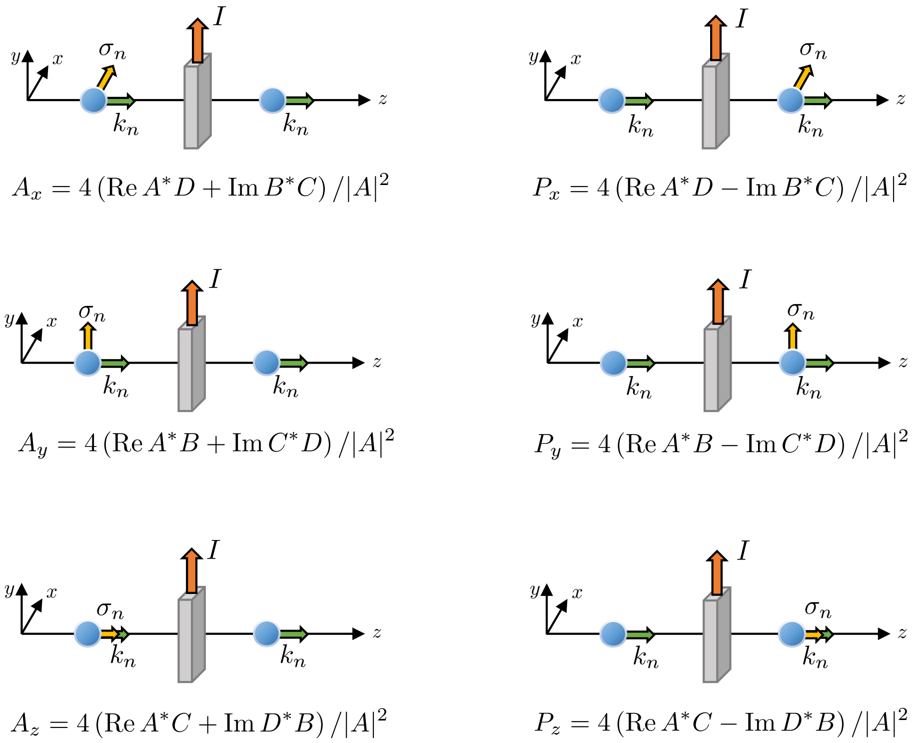

$A_x = 4\left(\mathrm{Re}\,A^*D + \mathrm{Im}\,B^*C\right)/|A|^2$ $P_x = 4\left(\mathrm{Re}\,A^*D - \mathrm{Im}\,B^*C\right)/|A|^2$

$A_y = 4\left(\mathrm{Re}\,A^*B + \mathrm{Im}\,C^*D\right)/|A|^2$ $P_y = 4\left(\mathrm{Re}\,A^*B - \mathrm{Im}\,C^*D\right)/|A|^2$

$A_z = 4\left(\mathrm{Re}\,A^*C + \mathrm{Im}\,D^*B\right)/|A|^2$ $P_z = 4\left(\mathrm{Re}\,A^*C - \mathrm{Im}\,D^*B\right)/|A|^2$

FIGURE 6.2: Combinations of observable variables.

where P_n is the polarization of the neutron and P_t is the polarization of the indium target. $|A|^2$ is the neutron transmission of the target, and $|A|^2 = \exp(-\rho\sigma_\mathrm{t}d_\mathrm{t})$, where ρ, σ_t, and d_t are the number density, total cross-section, and thickness of the target, respectively. By substituting each term of the forward scattering amplitude described in Appendix D into the 8 Re A^*D term in Eq. 6.3, the optimum thickness of the ^{115}In target to maximize Eq. 6.3 can be obtained. Here, matrix element W is applied to the value obtained in Chap. 4. The pseudo-magnetic effect of the B' term in Eq. D.1 reduces the experimental sensitivity of T violation. This spin rotation is canceled by applying an external magnetic field, i.e., $\mathrm{Re}\,B' = 0$. The solid curves in Fig. 6.3 depicts 8 Re A^*D as a function of the thickness z for the ^{115}In target. The thickness at which 8 Re A^*D is maximized is the optimal thickness of the target. The optimum thickness of the ^{115}In target for $\phi = 23.0°$ (left in Fig. 6.3), and $\phi = 252.0°$ (right in Fig. 6.3) are 6.0 and 8.9 cm, respectively. The upper limits of 8 Re A^*D for these scenarios are 8.2×10^{-6} (for $\phi = 23.0°$) and 19.4×10^{-6} (for $\phi = 252.0°$), respectively. These values are used in the next section to estimate the measurement time.

6.2.4 Estimation of the measurement time of T violation using the proton spin filter and indium target

The measurement time for the T violation required to reach the upper limit of W_T/W in Eq. 6.1 is discussed from a statistical perspective. The methods of measuring the polarization P_x and analyzing the power A_x are shown in Fig. 6.4, where N is the incident neutron flux; n_p and σ_p are the number density and total cross-section of the triplet-DNP spin filter, respectively; n_t and σ_t are the number density and total cross-section of the indium target, respectively; d_p and d_t are their thicknesses, respectively. The number of the transmitted neutrons for plus (minus) polarized polarizers and plus (minus) polarized analyzers are defined as N_{P_+} (N_{P_-}) and N_{A_+} (N_{A_-}), respectively.

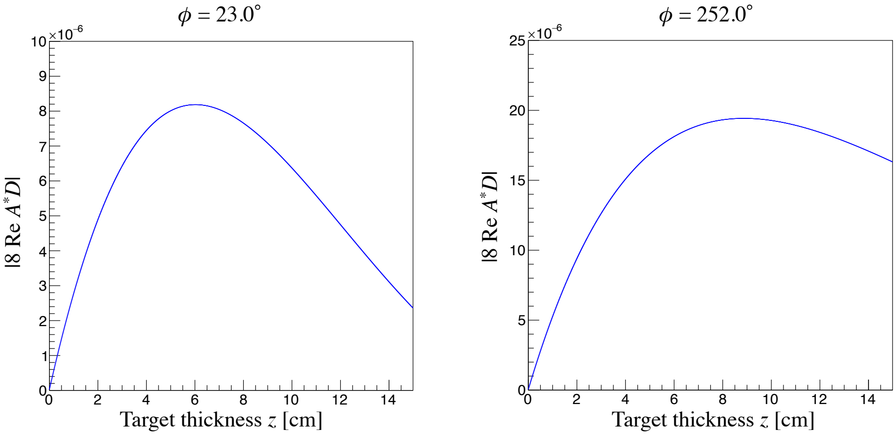

FIGURE 6.3: Target thickness dependence of the upper limit of $A_x + P_x$ for $\phi = 23.0°$ (left) and $\phi = 252.0°$ (right).

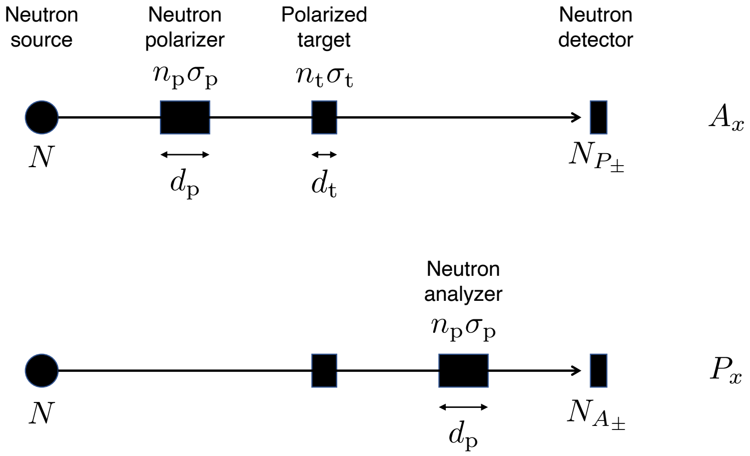

FIGURE 6.4: Experimental setup to measure A_x and P_x.

The analyzing power A_x and polarization P_x are expressed as

$$\begin{aligned} A_x &= \frac{N_{\mathrm{A}_+} - N_{\mathrm{A}_-}}{N_{\mathrm{A}_+} + N_{\mathrm{A}_-}}, \\ P_x &= \frac{N_{\mathrm{P}_+} - N_{\mathrm{P}_-}}{N_{\mathrm{P}_+} + N_{\mathrm{P}_-}} \frac{T_{\mathrm{pol}}}{\sqrt{T_{\mathrm{pol}}^2 - T_{\mathrm{unpol}}^2}}, \end{aligned}$$

where T_{unpol} and T_{pol} are the transmissions for the unpolarized and polarized polarizers, respectively, which are defined in Sec. 5.3. The detailed derivation process of P_x is described in Appendix D. The statistical errors of A_x and P_x are expressed as

$$\begin{aligned} \Delta A_x &= \frac{2\sqrt{N_{A_+} N_{A_-}}}{\left(N_{A_+} + N_{A_-}\right)^{3/2}} = \frac{1}{\sqrt{2NT_{\mathrm{pol}}}}, \\ \Delta P_x &= \frac{2\sqrt{N_{P_+} N_{P_-}}}{\left(N_{P_+} + N_{P_-}\right)^{3/2}} \frac{T_{\mathrm{pol}}}{\sqrt{T_{\mathrm{pol}}^2 - T_{\mathrm{unpol}}^2}} = \frac{1}{\sqrt{2NT_{\mathrm{pol}}}} \frac{T_{\mathrm{pol}}}{\sqrt{T_{\mathrm{pol}}^2 - T_{\mathrm{unpol}}^2}}. \end{aligned}$$

Here, the second equals are assuming

$$N_{A-} \approx N_{A+} \approx N_{P-} \approx N_{P+} \approx NT_{\mathrm{pol}} \exp(-\rho\sigma_{\mathrm{t}} d_{\mathrm{t}}). \tag{6.4}$$

The relationship to determine the value of $8\,\mathrm{Re}\,A^*D$ by measuring A_x and P_x with a 95% confidence level is

$$1.96\sqrt{\Delta {A_x}^2 + \Delta {P_x}^2} = P_n P_{\mathrm{t}} \frac{8\,\mathrm{Re}\,A^*D}{|A|^2}. \tag{6.5}$$

Substituting Eq. 6.4 into Eq. 6.5, the following equation is obtained:

$$\frac{1}{\sqrt{N}} = P_{\mathrm{n}} P_{\mathrm{t}} \frac{8\,\mathrm{Re}\,A^*D}{|A|^2} \sqrt{\frac{T_{\mathrm{pol}}^2 - T_{\mathrm{unpol}}^2}{2T_{\mathrm{pol}}^2 - T_{\mathrm{unpol}}^2}} \frac{\sqrt{2T_{\mathrm{unpol}}}}{1.96}. \tag{6.6}$$

To estimate the measurement time of the T violation when using the indium target, the following assumptions are made:

- The optimum thickness of the proton spin filter is 15 mm.
- A proton polarization of the proton spin filter is achieved at 50%.
- A thickness and a cross-section of the indium target are the optimum thickness calculated in the previous section and 4 × 4 cm^2, respectively.
- An indium polarization of the indium target is achieved at 30% [46].
- A beamline equipped with a Poison moderator is used, and the indium target is assumed to be placed at 15 m from the moderator surface.

Assuming the above, P_{n} is 50%, T_{pol} is 18%, T_{unpol} is 21%, $|A|^2$ is 17% (for $\phi = 23.0°$) or 7% (for $\phi = 252.0°$). The neutron flux N with a neutron energy of 6.85 eV was also assumed to be 2.8×10^6 n/sec, which was converted from the simulated values of the neutron beam intensity at J-PARC MLF BL07 (poisoned moderator) with a proton beam power of 1 MW [61]. The solid line curves shown in Fig. 6.5 represent Eq. 6.6 with $8\,\mathrm{Re}\,A^*D$ on the vertical axis and the number of days of measurement on the horizontal axis. The dashed lines represent the current upper limit obtained

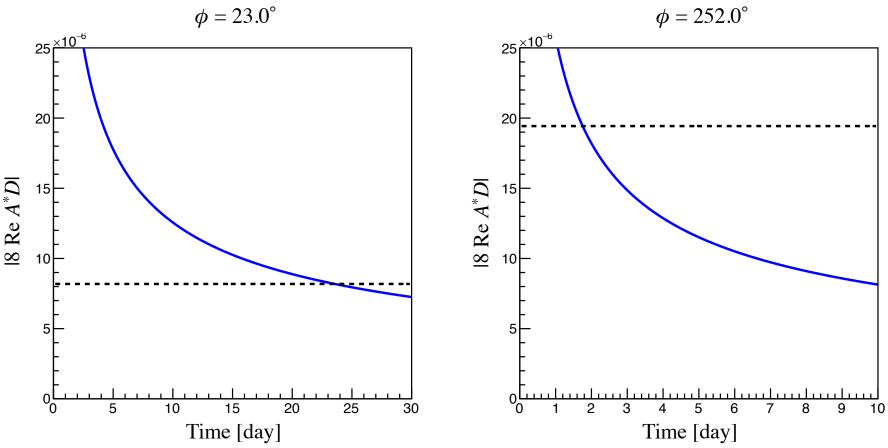

FIGURE 6.5: Estimation of measurement time to reach the current upper limit by EDM experiment. Cases for $\phi = 23.0°$ (left) and $\phi = 252.0°$ (right). The solid lines show the curve of $8\,\mathrm{Re}\,A^*D$ as a function of time, which is calculated using Eq. refeq:MeasurementTime. The dashed lines show the current upper limit obtained from the EDM search experiment converted to $8\,\mathrm{Re}\,A^*D$.

from the EDM search experiments, which corresponds to the value on the vertical axis at the optimum thickness in Fig. 6.3. The measurement time required to reach the current upper limit was estimated as 24 days for $\phi = 23.0°$ (left in Fig. 6.5), and 2 days for $\phi = 252.0°$ (right in Fig. 6.5), respectively. As mentioned at the end of Chap. 4, the value of ϕ can be uniquely determined by measuring the other coefficient terms described in Chap. 2 using a polarized neutron beam.

Chapter 7

Conclusion

An enhancement mechanism for T violation has been theoretically proposed for compound nuclear states, which can be realized to search for T violation with high sensitivity. However, the values of the parameters ϕ and $\kappa(J)$, which are necessary to estimate the sensitivity of T violation, have not yet been determined for most nuclei with p-wave resonances in the energy region of epithermal neutrons.

To determine the values of ϕ and $\kappa(J)$ for ^{115}In, which is one of the candidate target nuclei in experiments searching for T violation, this study measured the angular distribution of γ-rays emitted from the p-wave resonance of $^{115}\mathrm{In}+\mathrm{n}$ using germanium detectors at the ANNRI beamline at J-PARC. This analysis focused on the combined peak of the 5955 keV and 5971 keV peaks, which have a high emission probability from the p-wave resonance of $\mathrm{In}(\mathrm{n},\gamma)$. The single escape peak of the 6471 keV γ-ray from the $\mathrm{In}(\mathrm{n},\gamma)$ reaction was the main background, which could not be removed by the measurement data alone. A detector simulator using Geant4 was constructed to obtain an accurate detector response function. Using the simulation, the single escape peak background was successfully eliminated, and the angular distribution of the γ rays was accurately determined. From the results of the angular distribution measurement, the values of $|\kappa(J)| = 1.10^{+0.29+0.07}_{-0.26-0.09}$ for $\phi = 23.0^{+17.8+4.7\circ}_{-21.0-6.9}$ and $\kappa(J) > 1.66$ for $\phi = 252.0^{+21.0+6.9\circ}_{-17.8-4.5}$ were obtained. The value of $|\kappa(J)|$ deviates by 2.0σ from $|\kappa(J)| = 0$. The above results indicate that ^{115}In is a strong candidate for a T violation search. In addition, an epithermal neutron polarization device based on proton polarization using triplet DNP was developed. The polarization device, which consists of a naphthalene single crystal doped with 0.003 mol% deuterated pentacene, has a size of $\phi 15 \times 4$ mm^3, and operates at 0.35 T and 90 K. The polarization of epithermal neutrons by the triplet-DNP spin filter was demonstrated for the first time in this study by evaluating the performance of the spin filter in a compact neutron source. The average values of the proton and neutron polarizations were 0.250 ± 0.050 and 0.076 ± 0.015, respectively, and dramatic improvements in these values were expected through lowering the temperature and increasing the thickness of the filter.

The measurement time required to reach the current upper limit of the nEDM search was estimated to be 24 days with a 6.0 cm-thick indium target for $\phi = 23.0^\circ$ and 2 days with an 8.9 cm-thick indium target for $\phi = 252.0^\circ$ using a 15 mm-thick triplet-DNP spin filter with 50% proton polarization and an indium target with 30% polarization. This is the first step in extending the research area of compound nuclei to a very wide energy region of epithermal neutrons and are expected to significantly contribute to future research in particle physics.

Appendix A

Longitudinal asymmetry

In the process of neutron-induced compound nucleus production and decay, the resonant state can be represented by a zero-order perturbation term, and the PNC effect by a first-order perturbation term. Simplified Feynman diagrams of these processes are shown in Fig. A.1: (a) and (b) represent zero- and first-order perturbation processes, respectively. In each diagram, the left side shows a nucleus with mass number A absorbing a neutron (entrance channel), and the right side shows the final state of the reaction, which is a nucleus with mass number A and a neutron (exit channel). The line connecting the initial and exit channel vertices signifies the compound nucleus. $(A{+}1)_{\mathrm{s}}$ and $(A{+}1)_{\mathrm{p}}$ denote the s- and p-wave resonance states of the compound nucleus, respectively. The circles shown in Fig. A.1(b) shows transitions from the s- to p-wave resonance states (top figure) or vice versa (bottom figure). W in the circles is a weak matrix element. The coupling constants are indicated beside each vertex, and the propagation function is indicated immediately below the line that represents the compound nuclear state. Based on the Feynman rule, the probability amplitude f in the diagrams in Fig. A.1(b) can be expressed as

$$f_{\pm} = \mp \frac{g}{k} \frac{\sqrt{\Gamma_{\mathrm{s}}^{\mathrm{n}}} W \sqrt{\Gamma_{\mathrm{p},j=1/2}^{\mathrm{n}}}}{\left[E - E_{\mathrm{s}} + i\frac{\Gamma_{\mathrm{s}}}{2}\right]\left[E - E_{\mathrm{p}} + i\frac{\Gamma_{\mathrm{p}}}{2}\right]},$$

where k is the neutron momentum, E is the incident neutron energy, E_{s} (E_{p}) is the resonance energy of the s-wave (p-wave) resonance, Γ_{s} (Γ_{p}) is the resonance width of the s-wave (p-wave) resonance, and g is the statistical factor. The subscripts $+$ and $-$ refer to the helicity of the incident neutron. The probability amplitude f is the same in both the upper and lower figures. The helicity dependence of the capture cross-section on the incident neutron, $\Delta\sigma_{\mathrm{cap}}$, is expressed as

$$\begin{aligned} \Delta\sigma_{\mathrm{cap}} &= \sigma_{\mathrm{cap}}^{+} - \sigma_{\mathrm{cap}}^{-} = \frac{4\pi}{p} \,\mathrm{Im}\,(f_{+} - f_{-}) \\ &= -\frac{4\pi}{k^2} \frac{g\sqrt{\Gamma_{\mathrm{s}}^{\mathrm{n}}} W \sqrt{\Gamma_{\mathrm{p},j=1/2}^{\mathrm{n}}}}{\left[(E - E_{\mathrm{s}})^2 + \frac{\Gamma_{\mathrm{s}}^2}{4}\right]\left[(E - E_{\mathrm{p}})^2 + \frac{\Gamma_{\mathrm{p}}^2}{4}\right]} \left[(E - E_{\mathrm{s}})\,\Gamma_{\mathrm{p}} + (E - E_{\mathrm{p}})\,\Gamma_{\mathrm{s}}\right]. \end{aligned}$$

Now, by approximating $E \sim E_{\mathrm{p}}$, this can be simplified as

$$\Delta\sigma_{\mathrm{cap}} \simeq -4 \frac{W}{E_{\mathrm{p}} - E_{\mathrm{s}}} \sqrt{\frac{\Gamma_{\mathrm{s}}^{\mathrm{n}}}{\Gamma_{\mathrm{p}}^{\mathrm{n}}}} \sqrt{\frac{\Gamma_{\mathrm{p},j=1/2}^{\mathrm{n}}}{\Gamma_{\mathrm{p}}^{\mathrm{n}}}} \sigma_{\mathrm{p,cap}},$$

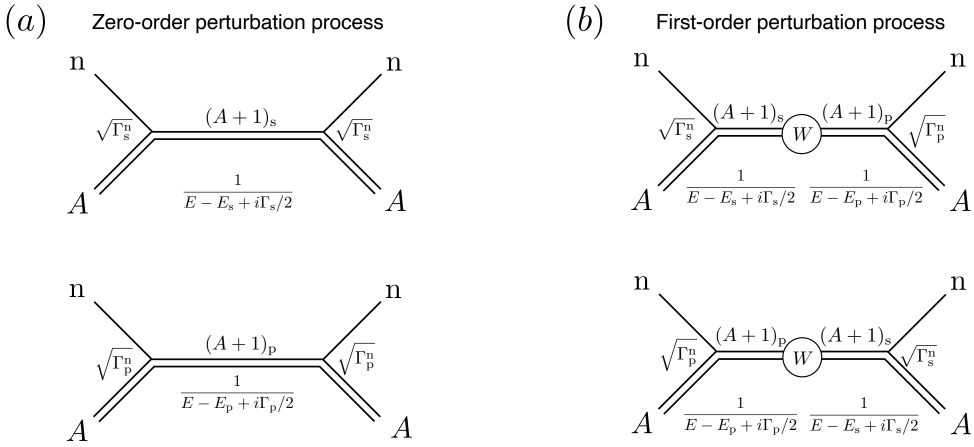

FIGURE A.1: Simplified Feynman diagrams of processes of neutron-induced compound nucleus. (a) and (b) show the zero- and first-order perturbation processes, respectively.

where $\sigma_{\mathrm{p,cap}}$ is the capture cross-section of the p-wave resonance. Thus,

$$\frac{\Delta\sigma_{\mathrm{cap}}}{2\sigma_{\mathrm{p,cap}}} \simeq -\frac{2W}{E_{\mathrm{p}}-E_{\mathrm{s}}}\sqrt{\frac{\Gamma_{\mathrm{s}}^{\mathrm{n}}}{\Gamma_{\mathrm{p}}^{\mathrm{n}}}}\sqrt{\frac{\Gamma_{\mathrm{p},j=1/2}^{\mathrm{n}}}{\Gamma_{\mathrm{p}}^{\mathrm{n}}}} = -\frac{2xW}{E_{\mathrm{p}}-E_{\mathrm{s}}}\sqrt{\frac{\Gamma_{\mathrm{s}}^{\mathrm{n}}}{\Gamma_{\mathrm{p}}^{\mathrm{n}}}} = A_{\mathrm{L}}.$$

Appendix B

Coefficient terms of differential cross-section in (n,γ) reaction

The expressions for coefficients a_0 to a_{17} in Eq. 2.1 are given by the products of the amplitudes V_1 to V_4 as

$$
\begin{aligned}
a_0 &= \sum_{J_\mathrm{s}} |V_1(E_\mathrm{n}, J_\mathrm{s})|^2 + \sum_{J_\mathrm{p},j} |V_2(E_\mathrm{n}, J_\mathrm{p})|^2, \\
a_1 &= 2\,\mathrm{Re} \sum_{J_\mathrm{s},J_\mathrm{p},j} V_1(E_\mathrm{n}, J_\mathrm{s}) V_2^*(E_\mathrm{n}, J_\mathrm{p}) P(J_\mathrm{s} J_\mathrm{p} \frac{1}{2} j 1 I F) z_j, \\
a_2 &= -2\,\mathrm{Im} \sum_{J_\mathrm{s},J_\mathrm{p},j} V_1(E_\mathrm{n}, J_\mathrm{s}) V_2^*(E_\mathrm{n}, J_\mathrm{p}) \beta_j P(J_\mathrm{s} J_\mathrm{p} \frac{1}{2} j 1 I F) z_j, \\
a_3 &= 3\sqrt{10}\,\mathrm{Re} \sum_{J_\mathrm{p},j,J'_\mathrm{p},j'} V_2(E_\mathrm{n}, J_\mathrm{p}) V_2^*(E_\mathrm{n}, J'_\mathrm{p}) P(J_\mathrm{p} J'_\mathrm{p} j j' 2 I F) z_j z_{j'} \begin{Bmatrix} 2 & 1 & 1 \\ 0 & \frac{1}{2} & \frac{1}{2} \\ 2 & j & j' \end{Bmatrix}, \\
a_4 &= -6\sqrt{5}\,\mathrm{Im} \sum_{J_\mathrm{p},j,J'_\mathrm{p},j'} V_2(E_\mathrm{n}, J_\mathrm{p}) V_2^*(E_\mathrm{n}, J'_\mathrm{p}) P(J_\mathrm{p} J'_\mathrm{p} j j' 2 I F) z_j z_{j'} \begin{Bmatrix} 2 & 1 & 1 \\ 1 & \frac{1}{2} & \frac{1}{2} \\ 2 & j & j' \end{Bmatrix}, \\
a_5 &= -\mathrm{Re} \sum_{J_\mathrm{s},J'_\mathrm{s}} V_1(E_\mathrm{n}, J_\mathrm{s}) V_1^*(E_\mathrm{n}, J'_\mathrm{s}) P(J_\mathrm{s} J'_\mathrm{s} \frac{1}{2} \frac{1}{2} 1 I F) \\
&\quad -6\,\mathrm{Re} \sum_{J_\mathrm{p},j,J'_\mathrm{p},j'} V_2(E_\mathrm{n}, J_\mathrm{p}) V_2^*(E_\mathrm{n}, J'_\mathrm{p}) P(J_\mathrm{p} J'_\mathrm{p} j j' 1 I F) z_j z_{j'} \begin{Bmatrix} 0 & 1 & 1 \\ 1 & \frac{1}{2} & \frac{1}{2} \\ 1 & j & j' \end{Bmatrix}, \\
a_6 &= -2\,\mathrm{Re} \sum_{J_\mathrm{s},J_\mathrm{p}} V_1(E_\mathrm{n}, J_\mathrm{s}) V_2^*(E_\mathrm{n}, J_\mathrm{p}, \frac{1}{2}) \delta_{J_\mathrm{s} J_\mathrm{p}}, \\
a_7 &= \sqrt{3}\,\mathrm{Re} \sum_{J_\mathrm{s},J_\mathrm{p}} V_1(E_\mathrm{n}, J_\mathrm{s}) V_2^*(E_\mathrm{n}, J_\mathrm{p}, \frac{3}{2}) P(J_\mathrm{s} J_\mathrm{p} \frac{1}{2} \frac{3}{2} 2 I F), \\
a_8 &= -18\,\mathrm{Re} \sum_{J_\mathrm{p},j,J'_\mathrm{p},j'} V_2(E_\mathrm{n}, J_\mathrm{p}) V_2^*(E_\mathrm{n}, J'_\mathrm{p}) P(J_\mathrm{p} J'_\mathrm{p} j j' 1 I F) z_j z_{j'} \begin{Bmatrix} 2 & 1 & 1 \\ 1 & \frac{1}{2} & \frac{1}{2} \\ 2 & j & j' \end{Bmatrix}, \\
a_9 &= -2\,\mathrm{Re} \sum_{J_\mathrm{s},J'_\mathrm{s}} V_1(E_\mathrm{n}, J_\mathrm{s}) V_3^*(E_\mathrm{n}, J'_\mathrm{s}) P(J_\mathrm{s} J'_\mathrm{s} \frac{1}{2} \frac{1}{2} 1 I F) \\
&\quad -12\,\mathrm{Re} \sum_{J_\mathrm{p},j,J'_\mathrm{p},j'} V_2(E_\mathrm{n}, J_\mathrm{p}) V_4^*(E_\mathrm{n}, J'_\mathrm{p}) P(J_\mathrm{p} J'_\mathrm{p} j j' 1 I F) z_j z_{j'} \begin{Bmatrix} 0 & 1 & 1 \\ 1 & \frac{1}{2} & \frac{1}{2} \\ 1 & j & j' \end{Bmatrix},
\end{aligned}
$$

$$
\begin{aligned}
a_{10} &= -2\,\mathrm{Re}\sum_{J_\mathrm{s}}[V_2(E_\mathrm{n},J_\mathrm{p},\frac{1}{2})V_3^*(E_\mathrm{n},J_\mathrm{s})+V_1(E_\mathrm{n},J_\mathrm{s})V_4^*(E_\mathrm{n},J_\mathrm{p},\frac{1}{2})]\delta_{J_\mathrm{s}J_\mathrm{p}},\\
a_{11} &= \sqrt{3}\,\mathrm{Re}\sum_{J_\mathrm{s},J_\mathrm{p}}[V_2(E_\mathrm{n},J_\mathrm{p},\frac{3}{2})V_3^*(E_\mathrm{n},J_\mathrm{s})+V_1(E_\mathrm{n},J_\mathrm{s})V_4^*(E_\mathrm{n},J_\mathrm{p},\frac{3}{2})]P(J_\mathrm{s}J_\mathrm{p}\frac{1}{2}\frac{3}{2}2IF),\\
a_{12} &= -36\,\mathrm{Im}\sum_{J_\mathrm{p},J'_\mathrm{p},j,j'}V_2(E_\mathrm{n},J_\mathrm{p})V_4^*(E_\mathrm{n},J'_\mathrm{p})P(J_\mathrm{p}J'_\mathrm{p}jj'1IF)z_jz_{j'}\begin{Bmatrix}2&1&1\\1&\frac{1}{2}&\frac{1}{2}\\1&j&j'\end{Bmatrix},\\
a_{13} &= 2\,\mathrm{Re}\sum_{J_\mathrm{s}}V_1(E_\mathrm{n},J_\mathrm{s})V_3^*(E_\mathrm{n},J_\mathrm{s})+2\,\mathrm{Re}\sum_{J_\mathrm{p}}V_2(E_\mathrm{n},J_\mathrm{p})V_4^*(E_\mathrm{n},J_\mathrm{p})z_jz_j,\\
a_{14} &= 2\,\mathrm{Re}\sum_{J_\mathrm{s},J_\mathrm{p},j}[V_2(E_\mathrm{n},J_\mathrm{p})V_3^*(E_\mathrm{n},J_\mathrm{s})z_j+V_1(E_\mathrm{n},J_\mathrm{s})V_4^*(E_\mathrm{n},J_\mathrm{p})z_j]P(J_\mathrm{s}J_\mathrm{p}\frac{1}{2}j1IF),\\
a_{15} &= 2\,\mathrm{Im}\sum_{J_\mathrm{s},J_\mathrm{p},j}V_2(E_\mathrm{n},J_\mathrm{p})V_3^*(E_\mathrm{n},J_\mathrm{s})z_j-V_1(E_\mathrm{n},J_\mathrm{s})V_4^*(E_\mathrm{n},J_\mathrm{p})z_j]\beta_jP(J_\mathrm{s}J_\mathrm{p}\frac{1}{2}j1IF),\\
a_{16} &= 6\sqrt{10}\,\mathrm{Re}\sum_{J_\mathrm{p},j,J'_\mathrm{p},j'}V_2(E_\mathrm{n},J_\mathrm{p})V_4^*(E_\mathrm{n},J'_\mathrm{p})P(J_\mathrm{p}J'_\mathrm{p}jj'2IF)z_jz_{j'}\begin{Bmatrix}2&1&1\\0&\frac{1}{2}&\frac{1}{2}\\1&j&j'\end{Bmatrix},\\
a_{17} &= -12\sqrt{5}\,\mathrm{Im}\sum_{J_\mathrm{p},j,J'_\mathrm{p},j'}V_2(E_\mathrm{n},J_\mathrm{p})V_4^*(E_\mathrm{n},J'_\mathrm{p})P(J_\mathrm{p}J'_\mathrm{p}jj'2IF)z_jz_{j'}\begin{Bmatrix}2&1&1\\1&\frac{1}{2}&\frac{1}{2}\\1&j&j'\end{Bmatrix}.
\end{aligned}
\tag{B.1}
$$

The longitudinal asymmetry A_L is derived from the a_{10} term in Eq. B.1, which corresponds to the helicity dependence of the neutron capture cross-section. The ratio of the a_{10} term to the $a_{0,\mathrm{p}}$ term is given by

$$
\begin{aligned}
\frac{a_{10}}{a_{0,\mathrm{p}}} &= \frac{-2x\,\mathrm{Re}\left(V_2\left(E_\mathrm{n},J_\mathrm{p}\right)V_3^*\left(E_\mathrm{n},J_\mathrm{s}=J_\mathrm{p}\right)+V_1\left(E_\mathrm{n},J_\mathrm{s}\right)V_4^*\left(E_\mathrm{n},J_\mathrm{p}=J_\mathrm{s}\right)\right)}{\left|V_2\left(E_\mathrm{n},J_\mathrm{p}\right)\right|^2}\\
&= \frac{-2xW}{\left(E_\mathrm{n}-E_\mathrm{s}\right)^2+\left(\Gamma_\mathrm{s}/2\right)^2}\sqrt{\frac{\Gamma_\mathrm{s}^\mathrm{n}}{\Gamma_\mathrm{p}^\mathrm{n}}}\left\{\left(E_\mathrm{n}-E_s\right)+\frac{\Gamma_{\mathrm{s},f}^\gamma}{\Gamma_{\mathrm{p},f}^\gamma}\right\}.
\end{aligned}
\tag{B.2}
$$

For $E_\mathrm{n}=E_\mathrm{p}$ and $E_\mathrm{p}-E_\mathrm{s}\gg\Gamma_\mathrm{s}$, Eq. B.2 can be expressed as

$$
\frac{a_{10}}{a_{0,\mathrm{p}}}\simeq-\frac{2xW}{E_\mathrm{p}-E_\mathrm{s}}\sqrt{\frac{\Gamma_\mathrm{s}^\mathrm{n}}{\Gamma_\mathrm{p}^\mathrm{n}}}=A_\mathrm{L}.
$$

Appendix C

Calibration of γ-ray and neutron energies

Calibration between the ADC pulse heights and γ-ray energies was performed using the 511 keV peak owing to positron annihilation and the 5893 keV peak of $^{115}\mathrm{In}(\mathrm{n},\gamma)$. A Gaussian function was fitted to each peak to obtain the center of the peak. Figure C.1 shows an example of fitting with the Gaussian function applied to each of the two peaks. The parameters C_0, $E_{\mathrm{PH,peak}}$, σ, and C_1 are the height of the Gaussian function, center of the peak, standard deviation, and constant term, respectively. Because of the asymmetry of the peaks resulting from the energy resolution of the germanium detector, the Gaussian function was fitted in an asymmetric region. Using a linear function connecting $E_{\mathrm{PH,peak}}$ obtained from fitting with the γ-ray energies of the literature value (511 keV and 5893 keV), the pulse height of the ADC was converted to γ-ray energy. The validity of the calibration was confirmed using the 7646 keV γ-ray peak of $^{56}\mathrm{Fe}(\mathrm{n},\gamma)$, which agreed with an accuracy of less than 1 keV.

A calibration from the TOFs to neutron energies was performed using the neutron kinetic energy equation:

$$\begin{aligned} E_{\mathrm{n}} &= \frac{1}{2} m_{\mathrm{n}} \left(\frac{L}{t}\right)^2 \\ &= \left(\frac{72.3 \times L}{t}\right)^2 . \end{aligned} \tag{C.1}$$

where L is 21.5 m, which is the distance from the moderator to the target position; m_{n} is the neutron mass; t is the TOF of the neutron between the moderator surface and the target. However, because of the neutron slowing-down process in the moderator described in Sec. 3.2, the neutron energy may differ for events with the same t. Therefore, the value obtained by substituting the TOF information from V1724 into this formula is not exactly equal to the neutron energy. The exact conversion to neutron energy can be obtained by the convolution of Eq. 3.1; however, in this study, it was convoluted into theoretical calculations instead of experimental data.

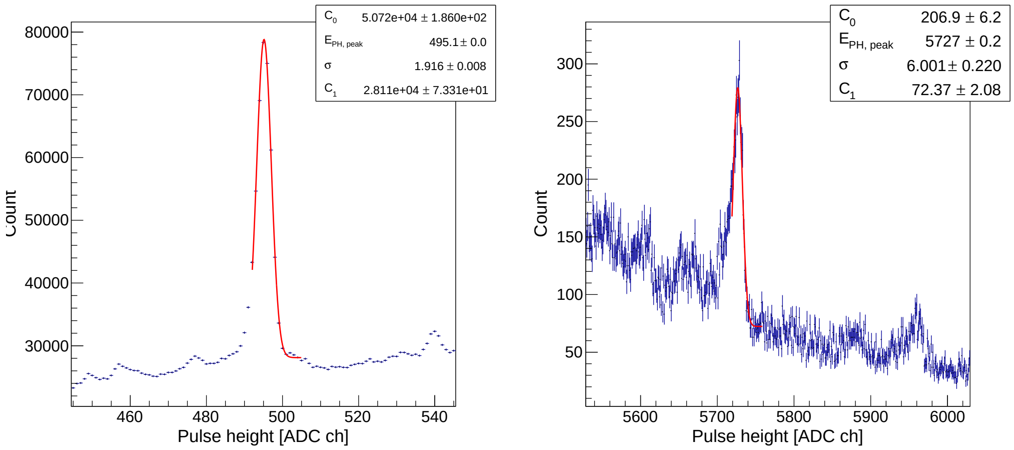

Figure C.1: Fitting with Gaussian function to 511 keV (left) and 5893 keV (right) peaks.

Appendix D

Neutron forward scattering amplitude

Describing the behavior of neutron spins in a polarized target, the initial and final spinors, denoted by U_i and U_f, can be related via the density matrix $\mathfrak{S}$, as follows:

$$\begin{aligned} U_f &= \mathfrak{S} U_i, \\ \mathfrak{S} &= e^{i(n-1)kz}, \\ n &= 1 + \frac{2\pi\rho}{k^2} f, \end{aligned}$$

where z is the thickness of the target, ρ is the number density of the material, and k is the neutron wavelength [121]. Here, $\mathfrak{S}$ is described as

$$\mathfrak{S} = A + B\left(\boldsymbol{\sigma}_{\mathbf{n}} \cdot \boldsymbol{I}\right) + C\left(\boldsymbol{\sigma}_{\mathbf{n}} \cdot \hat{\boldsymbol{k}}_{\mathbf{n}}\right) + D\left(\boldsymbol{\sigma}_{\mathbf{n}} \cdot \left(\boldsymbol{I} \times \hat{\boldsymbol{k}}_{\mathbf{n}}\right)\right), \tag{D.1}$$

$$\begin{aligned} A &= e^{iZA'} \cos b, \\ B &= ie^{iZA'} \frac{\sin b}{b} ZB', \\ C &= ie^{iZA'} \frac{\sin b}{b} ZC', \\ D &= ie^{iZA'} \frac{\sin b}{b} ZD', \\ Z &= \frac{2\pi\rho z}{k}, \\ b &= Z\sqrt{B'^2 + C'^2 + D'^2}. \end{aligned}$$

For a nucleus with $I = 9/2$ and $J = 5$, the neutron energy-dependent coefficient of each term in Eq. D.1 is expressed as

$$\begin{aligned} A'_{\mathrm{In}} &= -\frac{1}{16\sqrt{5}k}\left(9\frac{\Gamma^{\mathrm{n}}_{\mathrm{s}_0}}{E - E_{\mathrm{s}_0} + i\Gamma_{\mathrm{s}_0}/2} + 11\frac{\Gamma^{\mathrm{n}}_{\mathrm{s}_1}}{E - E_{\mathrm{s}_1} + i\Gamma_{\mathrm{s}_1}/2} + 11\frac{\Gamma^{\mathrm{n}}_{\mathrm{s}_2}}{E - E_{\mathrm{s}_2} + i\Gamma_{\mathrm{s}_2}/2}\right. \\ &\quad \left. +11\frac{\Gamma^{\mathrm{n}}_{\mathrm{p}}}{E - E_{\mathrm{p}} + i\Gamma_{\mathrm{p}}/2}\right) + \frac{1}{8\sqrt{5}k}\left(9a_- + 11a_+ + 11a_+\right), \\ B'_{\mathrm{In}} &= \frac{1}{400\sqrt{165}k}\left(825\frac{\Gamma^{\mathrm{n}}_{\mathrm{s}_0}}{E - E_{\mathrm{s}_0} + i\Gamma_{\mathrm{s}_0}/2} - 825\frac{\Gamma^{\mathrm{n}}_{\mathrm{s}_1}}{E - E_{\mathrm{s}_1} + i\Gamma_{\mathrm{s}_1}/2}\right. \\ &\quad \left. -825\frac{\Gamma^{\mathrm{n}}_{\mathrm{s}_2}}{E - E_{\mathrm{s}_2} + i\Gamma_{\mathrm{s}_2}/2}\frac{\Gamma^{\mathrm{n}}_{\mathrm{p}}}{E - E_{\mathrm{p}} + i\Gamma_{\mathrm{p}}/2}\left(-132\sqrt{6}x_S y_S + 1111x_S^2 - 396y_S^2\right)\right) \\ &\quad +\frac{825}{200\sqrt{165}}\left(a_- + a_+ + a_+\right), \end{aligned}$$

$$
\begin{aligned}
C'_{\mathrm{In}} &= \frac{11}{40k}\left(\frac{\sqrt{\Gamma^{\mathrm{n}}_{\mathrm{s}_1}}W\sqrt{\Gamma^{\mathrm{n}}_{\mathrm{p}}}}{(E-E_{\mathrm{p}}+i\Gamma_{\mathrm{p}}/2)(E-E_{\mathrm{s}_1}+i\Gamma_{\mathrm{s}_1}/2)}\right.\\
&\quad\left.+\frac{\sqrt{\Gamma^{\mathrm{n}}_{\mathrm{s}_2}}W\sqrt{\Gamma^{\mathrm{n}}_{\mathrm{p}}}}{(E-E_{\mathrm{p}}+i\Gamma_{\mathrm{p}}/2)(E-E_{\mathrm{s}_2}+i\Gamma_{\mathrm{s}_2}/2)}\right)\left(\sqrt{3}x_S-\frac{1}{\sqrt{2}}y_S\right),\\
D'_{\mathrm{In}} &= \frac{\sqrt{11}}{8k}x_S\left(\frac{\sqrt{\Gamma^{\mathrm{n}}_{\mathrm{s}_1}}W_{\mathrm{T}}\sqrt{\Gamma^{\mathrm{n}}_{\mathrm{p}}}}{(E-E_{\mathrm{p}}+i\Gamma_{\mathrm{p}}/2)(E-E_{\mathrm{s}_1}+i\Gamma_{\mathrm{s}_1}/2)}\right.\\
&\quad\left.+\frac{\sqrt{\Gamma^{\mathrm{n}}_{\mathrm{s}_2}}W_{\mathrm{T}}\sqrt{\Gamma^{\mathrm{n}}_{\mathrm{p}}}}{(E-E_{\mathrm{p}}+i\Gamma_{\mathrm{p}}/2)(E-E_{\mathrm{s}_2}+i\Gamma_{\mathrm{s}_2}/2)}\right),
\end{aligned}
\tag{D.2}
$$

where E is the neutron energy, E_{s} and E_{p} are the resonance energies, $\Gamma^{\mathrm{n}}_{\mathrm{s}}$ and $\Gamma^{\mathrm{n}}_{\mathrm{p}}$ are the neutron widths of the s- and p-wave resonances, respectively, Γ_{s} and Γ_{p} are the resonance widths of the s- and p-wave resonances, respectively, W is the matrix element of the P-violating interaction, and W_{T} is the matrix element of the P-violating interaction. Now, the subscripts 0, 1, and 2 of s are the 3.85 eV s-wave ($J=4$), 1.46 eV s-wave ($J=5$), and 9.07 eV s-wave ($J=5$), respectively. These terms were calculated based on Ref. [122], respectively. Here, x_S and y_S are given as

$$
\begin{pmatrix} x_S \\ y_S \end{pmatrix} = \begin{cases} \frac{1}{\sqrt{3(2I+1)}}\begin{pmatrix} -\sqrt{2I-1} & 2\sqrt{I+1} \\ 2\sqrt{I+1} & \sqrt{2I-1} \end{pmatrix}\begin{pmatrix} x \\ y \end{pmatrix} & (J=I-\frac{1}{2}) \\ \frac{1}{\sqrt{3(2I+1)}}\begin{pmatrix} -\sqrt{2I} & \sqrt{2I+3} \\ \sqrt{2I+3} & 2\sqrt{2I} \end{pmatrix}\begin{pmatrix} x \\ y \end{pmatrix} & (J=I+\frac{1}{2})\,. \end{cases}
\tag{D.3}
$$

Equation 1.3 is derived from the ratio of the D' and C', D'/C', which is calculated as

$$
\begin{aligned}
\frac{D'}{C'} &\propto \frac{x_S}{\sqrt{3}x_S-\frac{1}{\sqrt{2}}y_S}\frac{W_T}{W}\\
&= \frac{-2\sqrt{I}x+\sqrt{2I+3}y}{\sqrt{3}\left(-2\sqrt{I}x+\sqrt{2I+3}y\right)-\frac{1}{\sqrt{2}}\left(\sqrt{2I+3}x+2\sqrt{I}y\right)}\frac{W_T}{W}\\
&= \frac{1-\frac{1}{2}\sqrt{\frac{2I+3}{I}}\frac{y}{x}}{\sqrt{3}\left(1-\frac{1}{2}\sqrt{\frac{2I+3}{I}}\frac{y}{x}\right)+\frac{1}{\sqrt{2}}\left(\frac{1}{2}\sqrt{\frac{2I+3}{I}}+\frac{y}{x}\right)}\frac{W_T}{W}.
\end{aligned}
$$

Substituting $I=9/2$ in the denominator, this equation can be transformed as

$$
\frac{D'}{C'} \propto \left(1-\frac{1}{2}\sqrt{\frac{2I+3}{I}}\frac{y}{x}\right)\frac{W_T}{W} = \kappa(J)\frac{W_T}{W}.
\tag{D.4}
$$

Appendix E

Neutron spin analyzer

A neutron spin analyzer is exactly the same as a neutron spin filter, but it is used to measure the polarization of neutrons incident on the analyzer. The polarization P_x used in the calculations in Sec. 6.2.4 is derived using the following procedure. Consider that N neutrons pass through the neutron spin analyzer and N' neutrons reach the neutron detector (Fig. E.1). Here, p_n is the neutron polarization of the incident neutrons, n is the number density of protons in the analyzer, σ_0 and σ_p are the spin-independent and spin-dependent components of the scattering cross-section, respectively, d is the thickness of the analyzer, and P is the proton polarization of the analyzer. The number of transmitted spin-plus (-minus) neutrons, N_+ (N_-), is defined as

$$N_\pm \quad = \quad N e^{-n\sigma_0 t} \left(\cosh P n \sigma_\mathrm{p} d \mp p_\mathrm{n} \sinh P n \sigma_\mathrm{p} d\right).$$

Moreover,

$$N' \quad = \quad N_+ + N_- = 2Ne^{-n\sigma_0 d} \cosh P n \sigma_\mathrm{p} d.$$

When $p_\mathrm{n} = 0$ and $P = 0$, the neutron transmission T_unpol is given by

$$T_\mathrm{unpol} = e^{-n\sigma_0 d}.$$

Subsequently N' can be rewritten as

$$N' \quad = \quad 2NT_\mathrm{unpol} \cosh P n \sigma_\mathrm{p} d.$$

However, when the analyzer is proton-polarized, the neutron transmission T_pol is given by

$$T_\mathrm{pol} = \frac{N'}{2N} \quad = \quad T_0 \cosh P n \sigma_\mathrm{p} d.$$

Using these equations, the asymmetry of N_+ and N_- can be expressed as

$$\frac{N_+ - N_-}{N_+ + N_-} = -p_\mathrm{n} \tanh P n \sigma_\mathrm{p} d.$$

As P_x in Sec. 6.2.4 is synonymous with measuring the polarization of neutrons incident on the analyzer,

$$P_x = |p_\mathrm{n}| = \frac{N_+ - N_-}{N_+ + N_-} \frac{T_\mathrm{pol}}{\sqrt{{T_\mathrm{pol}}^2 - {T_\mathrm{unpol}}^2}}.$$

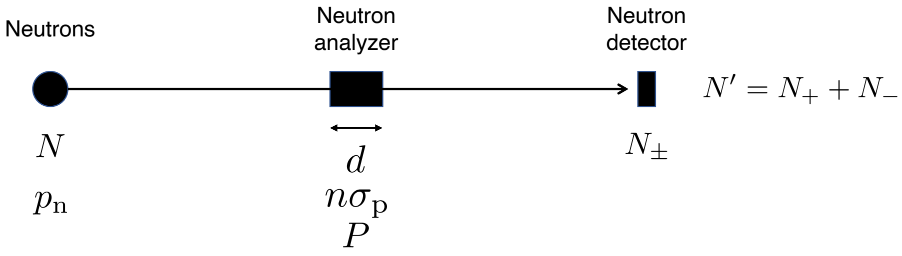

FIGURE E.1: Experimental setup to measure P_x.

Bibliography

[1] R. Brown, U. Camerini, P. H. Fowler, H. Muirhead, C. F. Powell, and D. M. Ritson, Nature **163**, 82 (1949).

[2] T. D. Lee and C. N. Yang, Phys. Rev. **104**, 254 (1956).

[3] C. S. Wu, E. Ambler, R. W. Hayward, D. D. Hoppes, and R. P. Hudson, Phys. Rev. **105**, 1413 (1957).

[4] L. Landau, Nucl. Phys. **3**, 127 (1957).

[5] J. H. Christenson, J. W. Cronin, V. L. Fitch, and R. Turlay, Phys. Rev. Lett. **13**, 138 (1964).

[6] M. Kobayashi and T. Maskawa, Prog. Theo. Phys. **49**, 652 (1973).

[7] Particle Data Group, Prog. Theo. Exp. Phys. **2020**, 083C01 (2020).

[8] K. Abe, R. Abe, I. Adachi, B. S. Ahn, H. Aihara, M. Akatsu, G. Alimonti, K. Asai, M. Asai, Y. Asano, *et al.*, Phys. Rev. Lett. **87**, 091802 (2001).

[9] B. Aubert, D. Boutigny, J. M. Gaillard, A. Hicheur, Y. Karyotakis, J. P. Lees, P. Robbe, V. Tisserand, A. Palano, G. P. Chen, *et al.*, Phys. Rev. Lett. **87**, 091801 (2001).

[10] A. D. Sakharov, Sov. Phy. Usp. **34**, 392 (1991).

[11] G. R. Farrar and M. E. Shaposhnikov, Phys. Rev. D **50**, 774 (1994).

[12] J. H. Smith, E. M. Purcell, and N. F. Ramsey, Phys. Rev. **108**, 120 (1957).

[13] P. D. Miller, W. B. Dress, J. K. Baird, and N. F. Ramsey, Phys. Rev. Lett. **19**, 381 (1967).

[14] W. B. Dress, J. K. Baird, P. D. Miller, and N. F. Ramsey, Phys. Rev. **170**, 1200 (1968).

[15] J. K. Baird, P. D. Miller, W. B. Dress, and N. F. Ramsey, Phys. Rev. **179**, 1285 (1969).

[16] W. B. Dress, P. D. Miller, and N. F. Ramsey, Phys. Rev. D **7**, 3147 (1973).

[17] W. B. Dress, P. D. Miller, J. M. Pendlebury, P. Perrin, and N. F. Ramsey, Phys. Rev. D **15**, 9 (1977).

[18] I. S. Altarev, Y. V. Borisov, A. B. Brandin, A. I. Egorov, V. F. Ezhov, S. N. Ivanov, V. M. Lobashov, V. A. Nazarenko, G. D. Porsev, V. L. Ryabov, *et al.*, Nucl. Phys. A **341**, 269 (1980).

[19] I. S. Altarev, Y. V. Borisov, N. V. Borovikova, A. B. Brandin, A. I. Egorov, V. F. Ezhov, S. N. Ivanov, V. M. Lobashev, V. A. Nazarenko, and V. L. Ryabov, Phys. Lett. B **102**, 13 (1981).

[20] J. M. Pendlebury, K. F. Smith, R. Golub, J. Byrne, T. J. L. McComb, T. J. Sumner, S. M. Burnett, A. R. Taylor, B. Heckel, N. F. Ramsey, *et al.*, Phys. Lett. B **136**, 327 (1984).

[21] K. F. Smith, N. Crampin, J. M. Pendlebury, D. J. Richardson, D. Shiers, K. Green, A. I. Kilvington, J. Moir, H. B. Prosper, D. Thompson, *et al.*, Phys. Lett. B **234**, 191 (1990).

[22] I. S. Altarev, Y. V. Borisov, N. V. Borovikova, S. N. Ivanov, E. A. Kolomensky, M. S. Lasakov, V. M. Lobashev, V. A. Nazarenko, A. N. Pirozhkov, A. P. Serebrov, *et al.*, Phys. Lett. B **276**, 242 (1992).

[23] P. G. Harris, C. A. Baker, K. Green, P. Iaydjiev, S. Ivanov, D. J. R. May, J. M. Pendlebury, D. Shiers, K. F. Smith, M. Van der Grinten, *et al.*, Phys. Rev. Lett. **82**, 904 (1999).

[24] C. A. Baker, D. D. Doyle, P. Geltenbort, K. Green, M. G. D. Van der Grinten, P. G. Harris, P. Iaydjiev, S. N. Ivanov, D. J. R. May, J. M. Pendlebury, *et al.*, Phys. Rev. Lett. **97**, 131801 (2006).

[25] A. P. Serebrov, E. A. Kolomenskiy, A. N. Pirozhkov, I. A. Krasnoschekova, A. V. Vassiljev, A. O. Polyushkin, M. S. Lasakov, A. N. Murashkin, V. A. Solovey, A. K. Fomin, *et al.*, Phys. Rev. C **92**, 055501 (2015).

[26] C. Abel, S. Afach, N. J. Ayres, C. A. Baker, G. Ban, G. Bison, K. Bodek, V. Bondar, M. Burghoff, E. Chanel, *et al.*, Phys. Rev. Lett. **124**, 081803 (2020).

[27] J. M. Pendlebury and E. A. Hinds, Nucl. Instrum. Meth. Phys. Res. Sect. A **440**, 471 (2000).

[28] M. Pospelov and A. Ritz, Ann. Phys. **318**, 119 (2005).

[29] D. E. Nagle, in Aip conference proceedings, Vol. 54, 1 (American Institute of Physics, 1979), pp. 760–764.

[30] R. Balzer, R. Henneck, C. Jacquemart, J. Lang, F. Nessi-Tedaldi, T. Roser, M. Simonius, W. Haeberli, S. Jaccard, W. Reichart, *et al.*, Phys. Rev. C **30**, 1409 (1984).

[31] P. von Rossen, U. von Rossen, and H. E. Conzett, in Aip conference proceedings, Vol. 69, 2 (American Institute of Physics, 1981), pp. 1442–1445.

[32] A. R. Berdoz, J. Birchall, J. B. Bland, J. D. Bowman, J. R. Campbell, G. H. Coombes, C. A. Davis, A. A. Green, P. W. Green, A. A. Hamian, *et al.*, Phys. Rev. C **68**, 034004 (2003).

[33] V. Yuan, H. Frauenfelder, R. W. Harper, J. D. Bowman, R. Carlini, D. W. MacArthur, R. E. Mischke, D. E. Nagle, R. L. Talaga, and A. B. McDonald, Phys. Rev. Lett. **57**, 1680 (1986).

[34] D. P. Grosnick, D. A. Hill, T. Kasprzyk, D. Lopiano, Y. Ohashi, J. Sheppard, T. Shima, H. Spinka, R. Stanek, D. G. Underwood, *et al.*, Phys. Rev. D **55**, 1159 (1997).

[35] G. E. Mitchell, J. D. Bowman, S. I. Penttilä, and E. I. Sharapov, Phys. Rep. **354**, 157 (2001).

[36] V. P. Gudkov, Phys. Rep. **212**, 77 (1992).

[37] B. A. Bernevig, *Topological insulators and topological superconductors* (Princeton university press, 2013).

[38] V. Gudkov and H. M. Shimizu, Phys. Rev. C **97**, 065502 (2018).

[39] T. Okudaira, S. Takada, K. Hirota, A. Kimura, M. Kitaguchi, J. Koga, K. Nagamoto, T. Nakao, A. Okada, K. Sakai, *et al.*, Phys. Rev. C **97**, 034622 (2018).

[40] J. Koga, "Measurement of angular distribution of gamma rays from neutron-induced compound states of 118 sn with a pulsed neutron beam", PhD thesis (Kyushu University, 2021).

[41] P. Hautle and M. Iinuma, Nucl. Instrum. Meth. Phys. Res. Sect. A **440**, 638 (2000).

[42] T. Yamamoto, "Experimental study of discrete symmetry in a compound nucleus using polarized neutrons", PhD thesis (Nagoya University, 2021).

[43] M. Bulatowicz, R. Griffith, M. Larsen, J. Mirijanian, C. B. Fu, E. Smith, W. M. Snow, H. Yan, and T. G. Walker, Phys. Rev. Lett. **111**, 102001 (2013).

[44] J. W. T. Dabbs, L. D. Roberts, and S. Bernstein, Phys. Rev. **98**, 1512 (1955).

[45] B. Gotschy, G. Denninger, H. Obloh, W. Wilkening, and J. Schneider, Solid State Commun. **71**, 629 (1989).

[46] S. Matsuki, *Dynamic nuclear self-polarization (dynasp) of in in semiconductor inp*, tech. rep. (2005).

[47] S. F. Mughabghab, *Neutron cross sections: neutron resonance parameters and thermal cross sections part b: z= 61-100*, Vol. 1 (Academic press, 2012).

[48] *National nuclear data center - brookhaven national laboratory*, `https://www.nndc.bnl.gov/`, 2021.

[49] M. A. Lone, E. D. Earle, and G. A. Bartholomew, Nucl. Phys. A **156**, 113 (1970).

[50] D. R. Rich, T. R. Gentile, T. B. Smith, A. K. Thompson, and G. L. Jones, Appl. Phys. Lett. **80**, 2210 (2002).

[51] T. E. Chupp, M. E. Wagshul, K. P. Coulter, A. B. McDonald, and W. Happer, Phys. Rev. C **36**, 2244 (1987).

[52] F. D. Colegrove, L. D. Schearer, and G. K. Walters, Phys. Rev. **132**, 2561 (1963).

[53] K. H. Andersen, D. Jullien, A. K. Petoukhov, P. Mouveau, F. Bordenave, F. Thomas, and E. Babcock, Physica B Condens. Matter **404**, 2652 (2009).

[54] A. Yoshimi, K. Asahi, K. Sakai, M. Tsuda, K. Yogo, H. Ogawa, T. Suzuki, and M. Nagakura, Phys. Lett. A **304**, 13 (2002).

[55] T. Ino, M. Nakamura, T. Oku, T. Shinohara, J. Suzuki, K. Ohoyama, and H. Hiraka, Physica B Condens. Matter **404**, 2667 (2009).

[56] V. I. Luschikov, Y. V. Taran, and F. L. Shapiro, *Polarized proton target as the neutron polarizer.* Tech. rep. (Joint Inst. for Nuclear Research, Dubna (USSR). Lab. of Neutron Physics, 1969).

[57] C. D. Jeffries, *Dynamic nuclear orientation*, 23 (Interscience Publishers, 1963).

[58] A. Abragam and M. Goldman, (1982).

[59] W. G. Williams *et al.*, *Polarized neutrons* (Clarendon Press Oxford, 1988).

[60] V. V. Flambaum and O. P. Sushkov, Nucl. Phys. A **435**, 352 (1985).

[61] `https://j-parc.jp/c/index.html`, 2021.

[62] `https://j-parc.jp/researcher/MatLife/ja/instrumentation/`, 2021.

[63] S. Takada, T. Okudaira, F. Goto, K. Hirota, A. Kimura, M. Kitaguchi, J. Koga, T. Nakao, K. Sakai, H. M. Shimizu, *et al.*, J. Instrum. **13**, P02018 (2018).

[64] S. Ikeda and J. M. Carpenter, Nucl. Instrum. Methods A **239**, 536 (1985).

[65] I. Cole and C. G. Windsor, Nucl. Instrum. Methods **171**, 107 (1980).

[66] M. C. Moxon, T. C. Ware, and C. J. Dean, Capture, Fission and Scattering Data Users' Guide for REFIT-2009-10 (UKNSFP243, 2010) (2010).

[67] H. J. Stone, M. G. Tucker, Y. Le Godec, F. M. Méducin, E. R. Cope, S. A. Hayward, G. P. J. Ferlat, W. G. Marshall, S. Manolopoulos, S. A. T. Redfern, *et al.*, Nucl. Instrum. Methods A **547**, 601 (2005).

[68] H. J. Stone, M. G. Tucker, F. M. Meducin, M. T. Dove, S. A. T. Redfern, Y. Le Godec, and W. G. Marshall, J. Appl. Phys. **98**, 064905 (2005).

[69] K. Kino, M. Furusaka, F. Hiraga, T. Kamiyama, Y. Kiyanagi, K. Furutaka, S. Goko, K. Y. Hara, H. Harada, M. Harada, *et al.*, Nucl. Instrum. Methods A **736**, 66 (2014).

[70] *User manual um5960 compass multiparametric daq software for physics applications.* 2019.

[71] K. Shibata, O. Iwamoto, T. Nakagawa, N. Iwamoto, A. Ichihara, S. Kunieda, S. Chiba, K. Furutaka, N. Otuka, T. Ohsawa, *et al.*, J. Nucl. Sci. Technol. **48**, 1 (2011).

[72] H. A. Bethe and G. Placzek, Phys. Rev. **51**, 450 (1937).

[73] W. E. Lamb Jr, Phys. Rev. **55**, 190 (1939).

[74] H. A. Bethe, Rev. Mod. Phys. **9**, 69 (1937).

[75] F. H. Fröhner, (2000).

[76] I. I. Gurevich, L. V. Tarasov, and R. I. Sharp, *Low-energy neutron physics* (North-Holland Publishing Company, 1968).

[77] H. Glättli and M. Goldman, *Methods of experimental physics*, 1987.

[78] H. Börner, J. Brown, C. J. Carlile, R. Cubitt, R. Currat, A. J. Dianoux, B. Farago, A. W. Hewat, J. Kulda, E. Lelièvre-Berna, *et al.*, OCP Science (2003).

[79] A. W. Overhauser, Phys. Rev. **92**, 411 (1953).

[80] T. R. Carver and C. P. Slichter, Phys. Rev. **92**, 212 (1953).

[81] C. D. Jeffries, Phys. Rev. **106**, 164 (1957).

[82] T. J. Schmugge and C. D. Jeffries, Phys. Rev. Lett. **9**, 268 (1962).

[83] D. A. Hill, J. B. Ketterson, R. C. Miller, A. Moretti, R. C. Niemann, L. R. Windmiller, A. Yokosawa, and C. F. Hwang, Phys. Rev. Lett. **23**, 460 (1969).

[84] T. O. Niinikoski and J. M. Rieubland, Phys. Lett. A **72**, 141 (1979).

[85] T. R. Eichhorn, B. Brandt, P. Hautle, A. Henstra, and W. T. Wenckebach, Mol. Phys. **112**, 1773 (2014).

[86] S. Takada, K. Tateishi, Y. Wakabayashi, Y. Ikeda, T. Yoshioka, Y. Otake, and T. Uesaka, Prog. Theo. Exp. Phys. **2020**, 123G01 (2020).

[87] A. J. Van Strien and J. Schmidt, Chem. Phys. Lett. **70**, 513 (1980).

[88] A. Henstra and W. T. Wenckebach, Mol. Phys. **112**, 1761 (2014).

[89] S. R. Hartmann and E. L. Hahn, Phys. Rev. **128**, 2042 (1962).

[90] A. Henstra, P. Dirksen, and W. T. Wenckebach, Phys. Lett. A **134**, 134 (1988).

[91] A. Henstra, T. S. Lin, J. Schmidt, and W. T. Wenckebach, Chem. Phys. Lett. **165**, 6 (1990).

[92] K. Tateishi, M. Negoro, S. Nishida, A. Kagawa, Y. Morita, and M. Kitagawa, Proc. Natl. Acad. Sci. **111**, 7527 (2014).

[93] K. Tateishi, M. Negoro, A. Kagawa, and M. Kitagawa, Angew. Chem. Int. Ed. **52**, 13307 (2013).

[94] M. Negoro, A. Kagawa, K. Tateishi, Y. Tanaka, T. Yuasa, K. Takahashi, and M. Kitagawa, J. Phys. Chem. A **122**, 4294 (2018).

[95] S. Fujiwara, M. Hosoyamada, K. Tateishi, T. Uesaka, K. Ideta, N. Kimizuka, and N. Yanai, J. Am. Chem. Soc. **140**, 15606 (2018).

[96] M. Haag, B. van den Brandt, T. R. Eichhorn, P. Hautle, and W. T. Wenckebach, Nucl. Instrum. Methods A **678**, 91 (2012).

[97] T. R. Eichhorn, M. Haag, B. van den Brandt, P. Hautle, W. T. Wenckebach, S. Jannin, J. J. Van der Klink, and A. Comment, J. Magn. Reson. **234**, 58 (2013).

[98] Y. Quan, B. van den Brandt, J. Kohlbrecher, W. T. Wenckebach, and P. Hautle, Nucl. Instrum. Methods A **921**, 22 (2019).

[99] N. Niketic, B. Brandt, W. T. Wenckebach, J. Kohlbrecher, and P. Hautle, J. Appl. Crystallogr. **48**, 1514 (2015).

[100] S. Ramo, J. R. Whinnery, and T. Van Duzer, *Fields and waves in communication electronics* (John Wiley & Sons, 1994).

[101] K. Takeda, Rev. Sci. Instrum. **78**, 033103 (2007).

[102] K. Takeda, J. Magn. Reson. **192**, 218 (2008).

[103] M. Takamura, Y. Ikeda, H. Sunaga, A. Taketani, Y. Otake, H. Suzuki, M. Kumagai, T. Hama, and Y. Oba, in J. phys. conf. ser. Vol. 734, 3 (IOP Publishing, 2016), p. 032047.

[104] Y. Ikeda, Y. Otake, and M. Mizuta, J. Adv. Concr. Technol. **15**, 603 (2017).

[105] A. Taketani, M. Yamada, Y. Ikeda, T. Hashiguchi, H. Sunaga, Y. Wakabayashi, S. Ashigai, M. Takamura, S. Mihara, S. Yanagimachi, *et al.*, ISIJ Int., ISIJINT (2016).

[106] Y. Wakabayashi, Y. Yoshimura, M. Mizuta, Y. Otake, and Y. Ikeda, J. Adv. Concr. Technol. **17**, 571 (2019).

[107] Y. Yoshimura, M. Mizuta, H. Sunaga, Y. Otake, and Y. Ishikawa, JAILCD, 233 (2019).

[108] Y. Otake, Y. Seki, Y. Wakabayashi, Y. Ikeda, T. Hashiguchi, Y. Yoshimura, H. Sunaga, A. Taketani, M. Mizuta, Y. Oshima, *et al.*, J. Disaster Res. **12**, 585 (2017).

[109] S. Satoh, Plasma Fusion Res. **13**, 2405056 (2018).

[110] K. Takeda, *Triplet state dynamic nuclear polarization: basics, concepts, methods* (VDM Publishing, 2009).

[111] M. Iinuma, Y. Takahashi, I. Shaké, M. Oda, A. Masaike, T. Yabuzaki, and H. M. Shimizu, Phys. Rev. Lett. **84**, 171 (2000).

[112] J. R. Granada, Z. Naturforsch. A **39**, 1160 (1984).

[113] G. L. Squires, *Introduction to the theory of thermal neutron scattering* (Courier Corporation, 1996).

[114] M. Mattes and E. Sartori, Nuclear Energy Agency, Paris (1984).

[115] S. Grieger, H. Friedrich, K. Guckelsberger, R. Scherm, and W. Press, J. Chem. Phys. **109**, 3161 (1998).

[116] N. Morishima and Y. Sakurai, Nucl. Instrum. Methods A **490**, 527 (2002).

[117] Z. Salhi, E. Babcock, K. Bingöl, K. Bussmann, H. Kammerling, V. Ossovyi, A. Heynen, H. Deng, V. Hutanu, S. Masalovich, *et al.*, in J. phys. conf. ser. Vol. 1316, 1 (IOP Publishing, 2019), p. 012009.

[118] Y. H. Song, R. Lazauskas, and V. Gudkov, Phys. Rev. C **83**, 065503 (2011).

[119] B. Graner, Y. Chen, E. G. Lindahl, B. R. Heckel, *et al.*, Phys. Rev. Lett. **116**, 161601 (2016).

[120] D. Blyth, J. Fry, N. Fomin, R. Alarcon, L. Alonzi, E. Askanazi, S. Baeßler, S. Balascuta, L. Barrón-Palos, A. Barzilov, *et al.*, Phys. Rev. Lett. **121**, 242002 (2018).

[121] L. Stodolsky, Phys. Lett. B **172**, 5 (1986).

[122] V. Gudkov and H. M. Shimizu, Phys. Rev. C **102**, 015503 (2020).